2017

Microwave resonant sensor for measurement of ionic concentration in aqueous solutions

Subhanwit Roy
Iowa State University

Microwave resonant sensor for measurement of ionic concentration in aqueous solutions

by

Subhanwit Roy

A thesis submitted to the graduate faculty

in partial fulfillment of the requirements for the degree of

MASTER OF SCIENCE

Major: Electrical and Computer Engineering
(Electromagnetics, Microwave and Nondestructive Evaluation)

Program of Study Committee:
Nicola Bowler, Co-major Professor
Nathan M. Neihart, Co-major Professor
Jaeyoun Kim

The student author, whose presentation of the scholarship herein was approved by the program of study committee, is solely responsible for the content of this thesis. The Graduate College will ensure this thesis is globally accessible and will not permit alterations after a degree is conferred.

Iowa State University

Ames, Iowa

2017

DEDICATION

To my parents.

TABLE OF CONTENTS

Page

NOMENCLATURE

DI	Deionized
FEA	Finite Element Analysis
HFSS	ANSYS High Frequency Structure Simulator
ISE	Ion Selective Electrode
PLL	Phase Locked Loop
PTFE	Polytetrafluoroethylene
RF	Radio Frequency
RLC	Resistor Inductor Capacitor
SMA	SubMiniature version A
TE	Transverse Electric
TM	Transverse Magnetic
UV	Ultraviolet
VNA	Vector Network Analyzer

ACKNOWLEDGMENTS

I would like to thank my major professors Dr. Nicola Bowler and Dr. Nathan M. Neihart, and my committee member, Dr. Jaeyoun Kim, for their guidance and support throughout the course of this research. I would also like to thank Dr. Amy L. Kaleita-Forbes for funding me and providing the resources to carry out this work.

In addition, I would like to offer my appreciation to Mr. Amin Gorji and the Electromagnetic Materials Design and Characterization (EMDC) Group for their guidance and assistance with this research. I want to also thank my parents, friends, and colleagues for their constant support, without which, this thesis would not have been possible.

ABSTRACT

Nitrate efflux from agricultural lands in the Midwestern United States mixes with surface streams and creates hypoxic conditions in the Gulf of Mexico, which lead to destruction of aquatic ecosystems. Besides, excess nitrate in drinking water poses a serious threat to human health, including blue baby syndrome, birth defects, and cancer. The current nitrate management techniques are inefficient and expensive, and a major reason for this is the lack of low-cost, effective ionic concentration monitoring systems. The dependence of nitrate concentration on local hydrology means that laboratory techniques yield incomplete data, whereas the available real-time monitoring techniques have drawbacks like exorbitant cost, ion selectivity issues, and others. This research aims to bridge the gap between reliable concentration monitoring and economic feasibility by developing a low-cost, effective, real time ion monitoring system which is field deployable and sensitive to changes in ionic concentration at agriculturally-relevant levels.

In this work, a resonant sensor is designed using an open-ended coaxial transmission line which can be evanescently perturbed by a liquid sample and shows a shift in its resonant frequency on change of ionic concentration of the sample. The dimensions of the coaxial resonator are optimized to ensure high sensitivity to changes in the ionic concentration of the sample at relevant concentrations, low manufacturing costs, and small physical dimensions to enable field deployment. The resonant sensor design is followed by the design and optimization of a suitable coupling structure which can take two-port transmission measurements to measure the characteristics of the resonator.

Finite Element Analysis (FEA) simulations are carried out using ANSYS HFSS, using as input data the complex permittivity of aqueous solution samples with varying concentrations of nitrate, sulfate, and chloride ions. Deionized water is taken as a reference sample, and a clear correlation between shift in resonant frequency and ionic concentration is observed for each of the three resonant modes studied, with the sensor being highly sensitive to concentration changes at agriculturally relevant concentrations. Appropriate fitting functions are implemented to represent the correlations between resonant frequency and ion concentration, and discussion on the feasibility of the designed sensor for field deployment is presented.

CHAPTER 1. GENERAL INTRODUCTION

1.1 Research Question

The research herein addresses the question of how to infer the ionic concentration of electrolyte liquids using a resonant method at a microwave frequency. The approach taken involves the design of a microwave resonator and a corresponding structure to couple the energy from the resonator to a measuring instrument. The method undertaken in this research is novel because, to our knowledge, no other group has used a resonant method to characterize ionic solutions. This work is important in the light of the need for a low cost, real time nitrate monitoring system to enable better nitrate management strategies in the Midwestern United States, where the excessive levels of nitrate in rivers from agricultural drainage has been drastically affecting both aquatic life as well as human health.

1.2 Motivation

In the predominantly agricultural Midwestern United States, wetness of soil limits productivity of the farmlands. In the state of Iowa, which has over 6 million units of croplands, and 375 distinct soil series, more than half of the different soil series face the challenge of removing the excess water in order to improve productivity [1].

One of the most effective procedures to remove the excess water from the soil is the use of subsurface tile drainage. In this technique, the excess moisture from the soil is eliminated by implementing a system of underground perforated drainage pipes. These pipes were traditionally

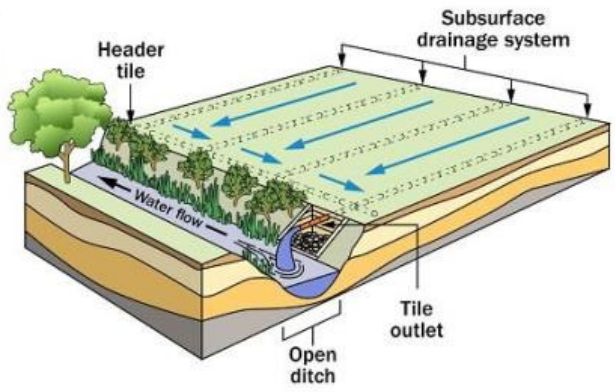

Figure 1.1 Illustration of a subsurface tile drainage system (taken from [3])

formed of tile, hence giving the drainage system its name. Nowadays, tile drainage systems are made of perforated plastic pipes which are typically positioned at a depth of 3 to 4.5 feet under the soil surface, depending on the subsoil permeability [2].

The subsurface tile drainage system, which has the objective of controlling a high water table to foster suitable conditions for crop production and field operations [4], ensures consistent yields and higher return on investment [5], as well as requiring less power for field operations, decreasing plant diseases, and even more being robust in drought [6], when compared with other conventional drainage techniques.

According to a USDA report [7], as of 1987, there are approximately 110 million acres of croplands in the United States which are artificially drained, and owing to the several advantages mentioned above, the adoption of tile drainage continuous to grow on previously undrained lands.

However, owing to the fact that tile drainage provides for a flow-path to the surface streams, excess nutrients from the croplands are washed directly to these streams [8]. This

creates an imbalance of the ions present in surface waterbodies, and in turn affects both aquatic as well as human life. Recent research at Iowa State University has found that the most common primary dissolved ions present in the agricultural tile drainage waters of Central Iowa, in descending order of parts per million concentration are HCO_3^-, Ca^{2+}, Mg^{2+}, NO_3^-, Cl^-, Na^+ and SO_4^{2-} [9].

Cations like Ca^{2+} and Mg^{2+} may increase the hardness of water, making it more difficult to use for domestic purposes, and hence incurring costs to soften it, whereas excess Na^+in drinking water may hamper the diets of patients of congestive heart failure and hypertension, among other ailments [121].

The excess anions in water have a more adverse effect on the environment as well as human health. Of all the anions in tile drainage water, NO^{3-} has the most significant impact.

Problems caused by excessive nitrate in tile drainage water

Nitrates (NO^{3-}) are an important source of nitrogen (N) for plants and are hence added in the form of fertilizers to facilitate agriculture. Nitrate is often reported as nitrate-nitrogen ($NO^{3-}—N$), which represents the total nitrogen that is present in the nitrate ion. By this definition, 10 mg/L of $NO^{3-}—N$ refers to approximately 44 mg/L of NO^{3-} in water.

As discussed earlier, excessive pollution of river water by nitrates from agricultural waste drastically affects the aquatic ecosystem. The contamination of nitrate accelerates eutrophication, which is the process of richening of nutrients in a water body due to runoff from land [11]. Eutrophication leads to excessive algae growth in river water. The algae use up the available oxygen in water, causing a condition called hypoxia. This results in the water being unable to support aquatic life.

It has been estimated that one million metric tons of nitrates are run off from croplands into the Mississippi River annually [12], and this leads to an area of hypoxia of over 20,000 km^2 in the northern Gulf of Mexico [13]. Of the total nitrate that is delivered by the Mississippi river into the Gulf of Mexico, the croplands of Iowa contribute about 25% of it, in spite of the state occupying less than 5% of the river's drainage basin [14]. Besides, excessive nitrate in drinking water can lead to a multitude of human health risks. One severe risk is Methemoglobinemia, which affects infants below the age of six months. Methemoglobinemia, commonly called Blue Baby Syndrome, decreases the blood's ability to transport oxygen and is potentially life-threatening.

By the Safe Drinking Water Act, there is a 10 mg/L (or 10 parts per million) standard set for the maximum contaminate level (MCL) of nitrate-nitrogen in drinking water [15]. A survey of rural wells in Iowa between 2006 and 2008 revealed that 12% of all the samples collected exceeded this standard [16]. Most of the Blue Baby Syndrome cases reported were found to have occurred in infants drinking water with concentrations of nitrate-nitrogen over 22 mg/L.

In addition to the above, nitrate in drinking water gets reduced inside the human body to form nitrite which gets further reduced to N-nitroso compounds. These compounds are potential carcinogens and teratogens, and increase the risk of bladder, colon, and rectum cancers [17-18], along with being a driving factor toward a lot of birth defects, including neural tube defects (NTDs), and congenital heart defects [19]. Also, high concentrations of nitrate have been seen to inhibit iodine uptake as well as instigate hypertrophic changes (enlargement) in the thyroid gland. The Iowa Environmental Council has summarized the results of peer-reviewed literature pertaining to health concerns due to elevated nitrate levels in the drinking waters of Iowa [20].

Problems caused by excess of other anions in tile drainage water

As stated before, the other anions which are found in excess in the surface streams of Central Iowa due to the contribution of agricultural effluxes are HCO_3^-, Cl^-, and SO_4^{2-}. Even though at the current levels they are found in tile drainage water they are not as pernicious as NO^{3-}, the potential hazards of these ions are discussed here for the sake of completeness.

The presence of HCO_3^- in water increases its pH. This can facilitate corrosion leading to failure of metallic structures, which in turn may pose serious health and economic problems. Also, excess bicarbonates can cause incrustation [21] of water-carrying pipes. This not only slows down the flow of water but also provides a suitable environment to harbor microorganisms which may be deleterious to human health, in turn precipitating a high demand for disinfectants.

Chlorides, which are usually present in the form of common salt in water, have not been identified to affect human health negatively. When coupled with Na^+ (a cation found in excess in the tile drainage waters of Iowa), Cl^- at a concentration over 250 mg/L can bring about "saltiness" in water, and requires expensive treatment to be made suitable for drinking. Additionally, Cl^- dissolved in water can corrode concrete by extraction of calcium. Another potential problem caused by Cl^- dissolved in water is in boilers, where it can generate highly corrosive hydrochloric acid upon heating [22].

In addition to causing similar problems like corrosion of piping and giving drinking water an unpleasant taste, the presence of excess sulfate ions in water poses a few more hazards. In young animals and human infants, drinking water contaminated with excess SO_4^{2-} can cause chronic diarrhea, being fatal in a few instances [23]. Sulfates are also responsible for aiding the methylation of mercury to form methylmercury, which is highly toxic, as well as promoting the biodegradation of organic soils [24].

To summarize this section, it can be seen that the widespread use of tile drainage systems in the Midwestern United States has led to elevated levels of several ions in surface water, which pose a plethora of hazards to both human health and the environment. Of these ions, nitrate has the most detrimental impact, and several studies mentioned above reveal that nitrate management in Iowa has been poor. Since the first step for efficient ion management is to be able to monitor ions effectively, discussion of the current ion monitoring systems is called for. This is the subject of the following section.

1.3 Current Ionic Concentration Monitoring Systems

Measuring the concentration of a solute in a solution is a fundamental problem of chemistry, with a lot of potential applications. The problem has attracted the attention of researchers over several decades. A multitude of methods, involving wet chemical colorimetry, mass spectroscopy, potentiometry, optical methods, remote sensing, and biosensors, have been developed for this purpose [25-27]. The need to operate with very low, agriculturally relevant concentrations renders many of these techniques unsuitable for this problem, however. Moreover, it has been seen [9] that the concentration of the various ions in the surface waters of Iowa is associated with the local hydrology and hence varies rapidly with time and space. For this reason, laboratory based methods which rely on spot and snapshot sampling do not paint an accurate picture of the contamination of water. Hence, for measuring ionic concentration in tile drainage water effectively, a detection system is required which is real time, has high sensitivity, and is field deployable.

Of all the methods found in literature, there are currently two approaches which are predominantly used to build effective, commercial, real time ion monitoring systems, namely: ion selective electrode technology, and ultraviolet absorption technology.

Ion Selective Electrode (ISE) Technology

Ion selective electrode (ISE) technology is an electrochemistry based approach which involves passing the aqueous solution sample across a specialized electrode membrane which is sensitive to only a particular kind of ion [28]. As the specific ion of interest diffuses across the membrane, an electrical potential is developed between the ion selective electrode and a reference electrode. The process can be assumed to follow the Nernst Equation [29]

$$E = E^0 + 2.3\frac{T}{n}\log(\gamma c) \tag{1.1}$$

where E stands for the measured voltage, E^0 is a reference constant, T is the temperature, n represents the charge on ion, γ stands for the ionic strength, and c represents ionic concentration. It can be observed that the voltage generated varies logarithmically with the concentration of the ion of interest [30].

Even though this approach has a few key advantages like being easy to use and relatively inexpensive compared to its counterparts, along with having a fast response time, it suffers from some serious drawbacks in practice because the ISE is seldom selective to only one ion [31]. This means that the presence of multiple ions causes interference in detecting the concentration of the target ion. It is a serious problem which limits the effectiveness of the approach for measuring the concentration of a particular ion in tile drainage water, which typically contains many different types of ions. There are also other challenges such as the need for low conductivity so that there is no interference with the generated voltage, and low solubility of the

membrane so that it does not get dissolved in the sample solution, which hurt the suitability of this approach for the problem of interest.

Ultraviolet (UV) Absorption Technology

Ultraviolet (UV) absorption technology makes use of the ability of a medium to absorb electromagnetic radiation in the ultraviolet spectrum. This is measured using a dimensionless quantity called absorbance [32], which is defined using the ratio of the intensity of the light transmitted by the sample to the intensity of the incident light at a particular wavelength of interest. Subsequently, Beer's Law, Equation (1.2), linearly relates the absorbance of a sample to its ionic concentration, given the knowledge of the thickness of the sample through which light travels, as follows [33].

$$c = \frac{A_\lambda}{\varepsilon_\lambda L} \tag{1.2}$$

Equation (1.2) uses absorbance of the sample A_λ, at a specific wavelength λ to compute ionic concentration c, given the values of the path length L, which is basically the thickness of the sample, and the molar absorptivity ε_λ, of the substance of interest at the operating wavelength. The absorbance A_λ can be calculated using the following equation:

$$A_\lambda = -\log\left(\frac{I_\lambda}{I_{\lambda_0}}\right) \tag{1.3}$$

In Equation (1.3), I_{λ_0} is the intensity of the light of wavelength λ incident on the sample, whereas I_λ is the intensity of light of the same wavelength after having passed through the sample,

Ultraviolet absorption technology has higher resolution than the ISE Method, and has a rapid response time too, but the interference of other ions and organic compounds with similar absorbance as the ion of interest acts to break down the linear relationship between ionic

concentration and absorbance, as predicted by Beer's Law. Furthermore, at high concentrations of solute, an increase in inter-ionic interactions also causes interference, rendering Beer's Law incapable of predicting the concentration accurately. Also, this technology requires highly monochromatic UV radiation, which is difficult to realize in practice, leading to exorbitant installation and maintenance cost of the sensor.

Thus, with the current technologies it is difficult to obtain a low cost, effective, real time ion monitoring system to operate in agriculturally relevant conditions. Hence, there is a need to develop a new technique to tackle the problem. A method based upon dielectric spectroscopy could be used to develop a real time ionic concentration sensing system, which would be potentially low cost, nondestructive, and of high accuracy.

1.4 Dielectric Spectroscopy

Dielectric spectroscopy involves measuring the complex permittivity of a sample over a frequency spectrum [34]. The real part of permittivity of a medium is a parameter that indicates the ability of the medium to become polarized by an external electric field, whereas the imaginary part quantifies losses incurred in the medium due to absorption of electrical energy upon the application of the external field.

The permittivity of a material essentially sprouts from the different kinds of polarizations exhibited by it. Depending on the material and the frequency of applied external field, a medium exhibits at least one of the three types of polarizations – electronic polarization (found in all dielectric materials), ionic polarization (found only in ionic materials), and orientation polarization (found only in materials possessing permanent dipoles) [35]. Under the influence of an alternating electric field, permanent dipoles try to reorient themselves as the direction of the

applied external electric field changes. For each polarization type, there exists a minimum time required for the dipole to align with the electric field, and this depends on the material under test. When for a particular polarization type the frequency of the applied electric field exceeds the inverse of this minimum reorientation time, called the relaxation frequency, the dipoles cannot keep up with the alternating electric field, and the polarization type does not contribute to the total polarization anymore. This effect manifests itself as a drop in the real part of permittivity, and is observed to be paired with a peak in the imaginary part. Such a process is called a relaxation process [36] and can provide insight into the composition of the sample.

Dielectric spectroscopy techniques entail applying an external time-varying electric field to the sample under test and measuring some quantity (impedance, reflection coefficient, transmission coefficient etc.) which can be used to find the complex permittivity of the sample. Studying the complex permittivity spectrum, subsequently, can provide information about the composition of the sample under test.

Dielectric Spectrum of Aqueous Solutions

The complex relative permittivity of a sample as a function of frequency *f is* defined as

$$\varepsilon_r(f) = \varepsilon_r'(f) - j\varepsilon_r''(f) \tag{1.4}$$

The real part of ε_r represents energy storage by the sample, whereas the imaginary part stands for the dissipation of energy by the sample. For an electrolyte solution, these two components of the complex relative permittivity can be attributed to three additive contributions, viz. intramolecular forces, intermolecular forces, and migration of charge carriers under an applied electric field (conductivity). The conductivity term contributes solely to the dissipation of energy [37], leading to a more informative version of Equation (1.4).

$$\varepsilon_r(f) = \varepsilon_r'(f) - j[\varepsilon_d''(f) + \frac{\sigma}{2\pi\varepsilon_0 f}] \tag{1.5}$$

where ε_r'' has been decomposed into a dipolar loss component ε_d'' and a dc conductivity term σ. Figure 1.2 demonstrates the dielectric spectrum of an electrolyte solution. The regions of the spectrum which correspond to $\frac{d\varepsilon'}{df} < 0$ signify different relaxation processes in the solution, which can be attributed to the following physiochemical mechanisms occurring as the frequency of applied electric field increases. It can be observed that a relaxation in ε_r' is associated with a corresponding peak of ε_r''. In fact, the two quantities, in principle, reveal the same information [38]. A detailed account of the different relaxation mechanisms can be found in [39].

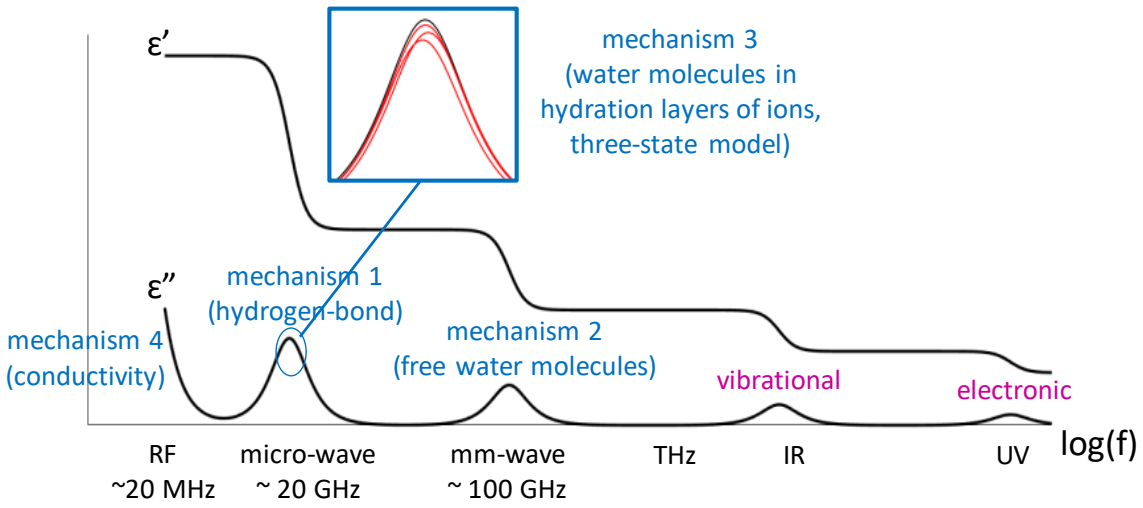

Figure 1.2 Dielectric dispersion of 1:1 electrolyte solution showing different relaxation mechanisms (taken from [39])

Since the shape of the dielectric spectrum allows us to have a peek into the sample's chemical structure and related physiochemical properties, parameters like the frequency of a

relaxation, relaxation time, permittivity values at very low or very high frequencies, etc. can be used to infer sample properties like ion type and ion concentration.

Dielectric spectroscopy has been demonstrated for all three common states of matter [40-42]. It is potentially a contactless method as it requires the sample to occupy only part of the region of the applied field and not necessarily be in direct contact with the probe used to apply the field although, most commonly, a flat sample is sandwiched between two parallel-plate electrodes. The time taken for the sample to react to the applied electric field is usually lesser than the time taken by the measuring instrumentation to read the corresponding data; hence, the speed of operation is determined by the rate at which the measuring instrumentation can read data rather than the speed at which the relaxation mechanisms occur [43].

Thus, with dielectric spectroscopy, it seems possible to carry out noncontact, nondestructive, and label-free real time measurements in a multi-solute solution, and thereafter infer the ion-types and the concentrations of the ions of interest [44]. Moreover, the microwave frequency region of the electromagnetic spectrum, where two of the relaxation mechanisms take place (mechanisms 1 and 3 in Fig. 1.2), offers low cost and high portability in terms of electronics, as opposed to higher frequencies. Hence, the subsequent research is targeted at building a microwave sensor which uses dielectric spectroscopy to infer ionic concertation of aqueous solutions.

1.5 Current Research Focus

Recent research in dielectric spectroscopy has related successfully the dielectric spectrum of electrolyte solutions with the ion types and concentrations for agriculturally relevant concentrations of NO_3^-, Cl^-, and SO_4^{2-}. Specifically, the research has been able to predict the ion type and the concentration of anion in an aqueous solution sample using three parameters

from the dielectric spectrum – real permittivity at dc, relaxation time, and dc conductivity. A detailed discussion on these parameters can be found in [45]. The method employed is dependent on the use of a highly sophisticated instrumentation, namely, a Vector Network Analyzer (VNA) which is expensive and not suitable for field deployment. Thus, the current research focuses on developing a suitable dielectric spectroscopy technique which can leverage the findings of the abovementioned research to come up with a low cost, highly sensitive, nondestructive, real time, field deployable sensing system for monitoring ionic concentration in tile drainage water.

CHAPTER 2. SAMPLE DATA

For the purpose of designing the ionic concentration monitoring sensor, as well as testing its performance, the complex permittivity data of different concentrations of aqueous solutions of sodium nitrate, sodium sulfate, and sodium chloride are used. This chapter summarizes how the dielectric spectra of the different aqueous solutions were measured. The details of these experiments can be found in [45].

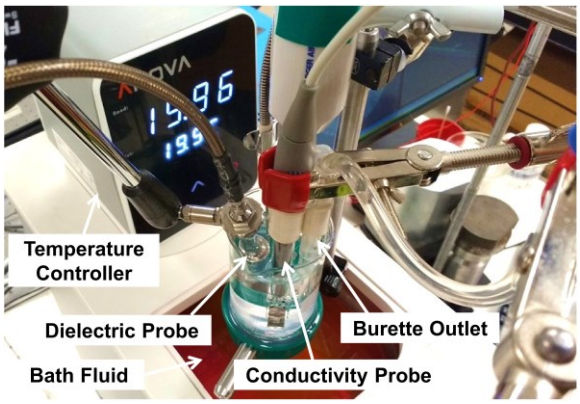

(a)

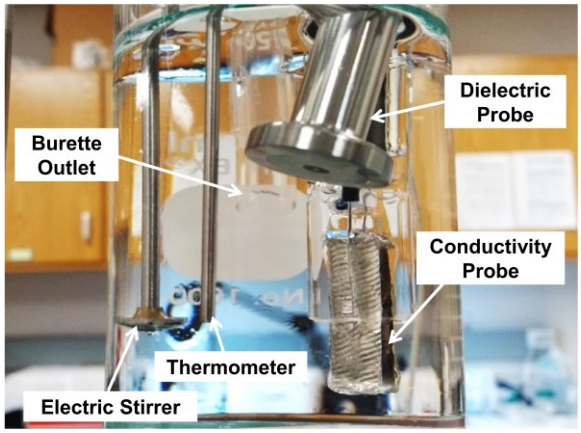

(b)

Figure 2.1 Experimental setup (a, b) for measurement of complex permittivity and conductivity of an electrolyte sample at a fixed controlled temperature. The VNA is not shown (taken from [45]).

A Speag open-ended coaxial DAK3.5 dielectric probe kit (recommended bandwidth of 200 MHz to 20 GHz) was used in conjunction with an Anritsu 37347C Vector Network Analyzer

(nominal bandwidth of 40 MHz to 20 GHz) to investigate the dielectric spectra of the different samples under test. The experimental setup is shown in Figure 2.1. The probe was fixed at an angle of 30° to optimize the sensitivity of the sensor, and a beaker, containing a sample solution was moved to interface with the probe. The DAK software enabled the calculation of the real and imaginary parts of the complex permittivity of the sample under test, ε_r' and ε_r'' respectively, from a measurement of S_{11} at the interface between the coaxial probe and the solution sample, which for a one-port network, is synonymous with the reflection coefficient.

The calibration for the one-port network was carried out using three standards: short-circuit (shorting block), open circuit (air), and a reference load (deionized water at 25 ºC). Once calibrated, for each sample, the VNA was set to logarithmically sweep 100 points for ten times in the frequency range of 200 MHz to 20 GHz. In addition, to measure conductivity a separate Seven2Go™ conductivity meter was used along with an InLab720 probe (operating range 0.1 to 500 µS/cm ± 0.5%), which was calibrated with a standard 84 µS/cm solution.

The temperature of the sample was maintained at 25 ºC ± 0.01 ºC by placing the sample beaker in a temperature-controlled Anova R10 Refrigerated and Heating Circulator (± 0.01 ºC). The effect of ambient temperature fluctuations was minimized with the use of Downtherm SR-1 Ethylene Glycol oil (18.1 Vol %) as a bath fluid, and an electric stirrer was incorporated to obviate the influence of turbulence to maintain a uniform temperature across the entire volume of the sample solution.

Electrolyte solution samples of three different salts: sodium nitrate, sodium sulfate, and sodium chloride, were prepared for the study. Fifteen concentrations of each type of solution, which are environmentally relevant, were tested from lower to higher concentrations by

gradually titrating the required stock electrolyte into a fixed volume of deionized water. The range of concentrations of the three electrolyte solutions used has been listed in Table 2.1.

Table 2.1 Concentration of different electrolyte solutions tested

Electrolyte Solution	Range of Concentrations Tested (mmol/L)
Sodium Nitrate	0 to 28.56
Sodium Sulfate	0 to 12.48
Sodium Chloride	0 to 11.28

The complex permittivity of an aqueous solution sample ε_r can be expressed in terms of its real and imaginary components using Equation (1.5).

The experimental data is fitted by a single-term Debye relaxation model, and the three different contributions to $\varepsilon_r(f)$, i.e. polarization $\varepsilon_r'(f)$, dipolar loss $\varepsilon_d''(f)$, and conductivity contribution $\frac{\sigma}{2\pi\varepsilon_0 f}$ have been plotted in Figure 2.2 for all three types of ionic solutions with similar concentration, $c \approx 7$ mmol/L.

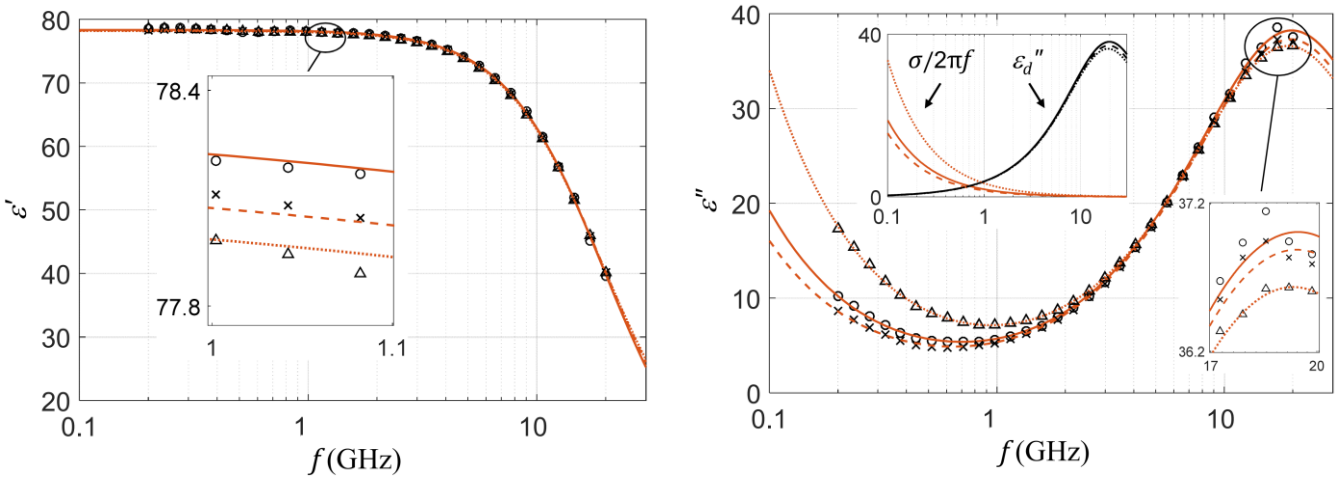

(a) (b)

Figure 2.2 (a) Dielectric dispersion $\varepsilon'(f)$, and (b) loss $\varepsilon''(f)$ spectra at T = 25 °C of aqueous solutions of $NaNO_3$ (cross-dashed line) with $c = 7.139$ mmol/L, Na_2SO_4 (triangle-dotted line) with $c = 7.797$ mmol/L, and $NaCl$ (circle-solid line) with $c = 7.052$ mmol/L. The markers denote the measured permittivity data, whereas the fitted curves using single Debye model are represented by lines. The contributions to $\varepsilon''(f)$ by the conductivity term ($\frac{\sigma}{2\pi f\varepsilon_0}$) and the dipolar relaxation process $\varepsilon_d''(f)$ are also separately shown in (b) (taken from [46])

CHAPTER 3. APPROACH

The current chapter aims at finding a suitable dielectric metrological technique, which can be leveraged to build a low cost, highly sensitive, nondestructive, real time, field deployable sensor for monitoring ionic concentration in electrolyte solutions. The chapter begins with an introduction to microwave frequency dielectric spectroscopy, and goes on to survey the various dielectric metrological techniques found in literature. Based on the survey, a decision is made about the dielectric measurement method to be used to design the ionic concentration monitoring sensor for the current research.

3.1 Microwave Frequency Dielectric Spectroscopy

The problem herein deals with a polar solvent system, i.e. a solvent with molecules which have permanent dipole moments. The fact that for such a system many dipolar relaxations occur in the microwave spectrum (300 MHz and above, i.e. centimeter scale wavelengths) helps narrow down the focus of the problem to only the microwave region. For an aqueous solution, its complex permittivity at microwave frequencies is dominated by electric dipole interactions. This allows one to disregard ionic and electronic effects [44], and thus avoid problematic electrode polarization effects which can be seen for lower frequency techniques [91].

When comparing polar molecules with their nonpolar counterparts, it is observed that polar molecules have higher values of their real part of relative permittivity, ε_r'. This typically lies in the range of 10-100 and arises from the presence of permanent dipoles in polar molecules. This phenomenon relates to the absorption of more energy to reorient dipoles under the influence of an alternating electric field, typically oscillating at a microwave frequency, leading to higher losses in polar molecules, which manifests as a relatively higher imaginary part of permittivity,

ε_r". The molecular dielectric relaxations also imply a pronounced frequency dependence of the complex permittivity for polar molecules in the microwave frequency range, as has been mentioned before.

There has been significant research done over the last few decades involving the study of dielectric properties of polar liquids in microwave frequencies. There has been continued interest in the molecular structure of polar dielectric liquids, and studying the dielectric relaxations of these molecules through microwave spectroscopy provide clues about the same [48]. Also, the use of polar liquids as dielectric reference materials [49] and to make tissue-equivalent materials [50] have attracted considerable attention toward dielectric spectroscopy of these liquids from researchers.

The following two sections deal with reviewing the various techniques found in literature for dielectric measurements of liquids in the microwave frequency range, with more focus on polar liquids. As mentioned earlier, the survey that follows has been conducted with the aim of narrowing down on an appropriate measurement technique for the purpose of the current research, i.e. the need to build a low cost, highly sensitive, nondestructive, real time, field deployable sensor.

The survey has been organized in three sections. Sections 3.2 and 3.3 respectively discuss the two broad families of microwave dielectric measurement techniques found in literature, namely broadband spectroscopy, and resonant techniques. Section 3.4 talks briefly about some other microwave dielectric techniques.

Comparisons between various kinds of techniques are presented in Section 3.5, and based on them a decision is made regarding the type of dielectric spectroscopy method to be used as the foundation for designing the ion concentration monitoring sensor.

3.2 Broadband Dielectric Spectroscopy Methods

Broadband dielectric spectroscopy is one of the most commonly used and studied families of microwave dielectric measurement techniques. These methods involve applying some power carried by a time-varying electric field to a sample whose dielectric properties are to be determined, and measuring either the power reflected by the sample, or the power that is transmitted across the sample to a measuring port. The reflectance and the transmittance depend on the material's dielectric properties, and thus can be used to infer the complex permittivity of the sample at the given frequency. Such techniques generally employ sweeping the frequency of the applied electric field over a broad spectrum, hence the name broadband, and obtain complex permittivity as a function of frequency. Based on what kind of measurement is taken, broadband dielectric spectroscopy methods can be further classified into reflectometric methods, transmission methods, and those that employ both together. Since these methods deal with power reflected and/or transmitted by a sample, S-parameters [51] are often the measured quantity upon which the analysis of the sample is based.

Reflectometric Methods

Reflectometric methods involve applying an alternating electric field to a sample and measuring the S_{11} scattering parameter or the complex reflection coefficient Γ. It is worth mentioning that reflection based methods can be modeled as a one port network, and for such a network S_{11} and Γ are identical. This complex reflection coefficient of the sample, in turn, can be related back to the complex permittivity of the sample under test. Such methods typically make use of a calibrated Vector Network Analyzer (VNA) to carry out the measurements, although many of the reflectometric spectroscopy methods were in place long before VNAs became

widely available, when slotted lines and waveguide null bridges were common techniques used to measure the reflection coefficient [52-53].

One of the earliest contributions in this field was made by Roberts and von Hippel [54], in which a short-circuited section of a coaxial line containing the liquid sample was used. This method and related techniques implementing shorted sections of either coaxial line or waveguide have been often used for dielectric metrology [55-57]. Considerable work has also been done to study the effects of losses and uncertainties of measurement in such techniques [58-60]. At microwave frequencies, however, realizing a short circuit is nontrivial, and might result in the magnitude of reflection coefficient being less than unity. This calls for compensation, and one approach adopted is to ensure that the sample liquid is in sufficient quantity to absorb all the RF power, effectively making the sample infinitely long, thus doing away with the impact of a non-ideal short [53]. A fairly recent implementation of a waveguide based method for dielectric characterization of liquids in the frequency range of 60-90 GHz, which spans parts of the V (40-75 GHz) and W (75-110 GHz) bands of the frequency spectrum, has been demonstrated in [61].

The most commonly used broadband dielectric technique is the coaxial reflectance sensor or, simply, the coaxial probe, which was analyzed in [62]. The largest distinction from the previously discussed Roberts and Von Hippel method is the use of an open-ended coaxial line. This does away with the need for a section of the coaxial cable to be filled with the sample, and thus provides a way to carry out non-invasive measurements. The working principle of such a sensor involves measuring the reflection coefficient after a propagating wave reflects off the open aperture of the coaxial transmission line. From transmission line theory [63], it can be concluded that the complex reflection coefficient Γ depends on the complex aperture admittance Y_L as follows:

$$\Gamma = \frac{Y_0 - Y_L}{Y_0 + Y_L} \tag{3.1}$$

In the above equation Y_0 represents the characteristic admittance of the coaxial transmission line ('coax'). The complex aperture admittance Y_L can be shown to be dependent on the complex permittivity of the sample which occupies the evanescent field in the region adjacent to the open-end of the coax, where the waves can no longer propagate. In order to achieve this. the modes inside and outside the coaxial line need to be matched [44]. Details on different aperture admittance models used in dielectric spectroscopy and their effects on sensitivity are discussed in [64].

It is a customary practice to have a dielectric insert, or a bead, at the end of the coaxial line to prevent fluid ingress while providing a path for the evanescent field to couple into the fluid. Such dielectric inserts are usually made of polymers with low permittivity, high thermal stability, and high chemical resistance. The sudden transition from air to bead inside the coaxial cable, however, causes impedance mismatch. To tackle this problem, the bead region can be made of a different diameter, and an undercut can help get rid of discontinuity fringing capacitances [65]. Furthermore, it is desirable that the coaxial sensor incorporates a large circular

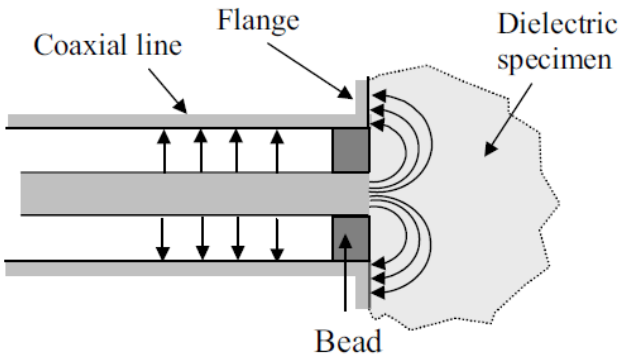

Figure 3.1 Illustration of an open ended coaxial sensor for dielectric spectroscopy (taken from [68])

flange. This allows one to neglect the fringing electric field lines at the aperture, and thus approximate electric field at the boundary to be zero. This approximation, in turn, simplifies numerical analysis. A flange diameter which is a few times larger than that of the outer conductor diameter of the coaxial transmission line, along with a large sample size is usually sufficient to approximate that the field at the edge of the flange is practically zero, and all the entire field is confined near the aperture, but not always [66]. An analysis of coaxial sensors using full-wave theory and accounting for a finite flange diameter has been reported in [67]. In [68], the authors review the various computational algorithms which have been used to model the open-ended coaxial cable reflectometry sensor. Figure 3.1 illustrates a typical broadband coaxial probe sensor.

Calibration is another aspect which has attracted the attention of a lot of researchers working with coaxial probe sensors. The entire experimental setup consisting of the coaxial probe, the transmission line connecting the probe to the VNA, and the VNA itself requires rigorous calibration prior to use. Calibration is done to compensate for the effect of mismatches anywhere in the setup. The most common calibration practice is to use three measurements – an open circuit, where the sensor radiates to air, a short circuit, where the coaxial line's aperture is shorted by a conductor, and a load, where the sensor is loaded with a reference liquid with known dielectric properties [69], although other calibration methods are also found in literature [70-71]. Water serves as a good reference liquid but errors might stem from air bubbles forming on the sensor surface or flange. This calls for manual removal of the air bubbles. Also, it is good metrological practice to validate the calibration using a second reference liquid, and ethanol is commonly used for this purpose. This is because errors during calibration lead to high uncertainties in the measured data and an independent test of the calibration quality using a

second reference liquid mitigates against a poor calibration. Monte Carlo Modeling provides an effective way to estimate the uncertainties of measurements on dielectrics for which reference materials with similar dielectric properties are not available [65].

References [72-74] talk about different industrial applications of the coaxial reflectance sensor such as density monitoring of crude oil in the petroleum industry, and dielectric spectroscopy of breast tissue to aid in breast cancer detection. Variations of the coaxial probe which have calculable geometries have been explored by researchers. In [75], an open ended coaxial probe has been discussed where the sample is backed by a sheet of conductor, which allows for the approximation of the sample to have infinite area. A coaxial technique with a discontinuous inner conductor has been taken up for research in [76], whereas [77] explores another coaxial sensor where a cylindrical cavity is attached to its aperture to store the sample under test. There has also been some research done with open-ended waveguide sensors [78-79]. Such sensors have been observed to be better suited for low permittivity material measurements than coaxial sensors [68].

Transmission Methods

Transmission methods employ a two-port sample cell, that is loaded with the sample in some way, and use the ratio of the power transmitted by the cell to the power applied to it to infer dielectric properties of the sample [80-82]. In the case of a coaxial sample cell and a liquid sample, for example, inlet and outlet pipes facilitate the introduction of the liquid into the cell, and dielectric inserts known as beads are used to prevent it from flowing into the transmission line hosting the cell. Figure 3.2 illustrates a transmission method employing a coaxial line to infer sample permittivity from measured S-parameters.

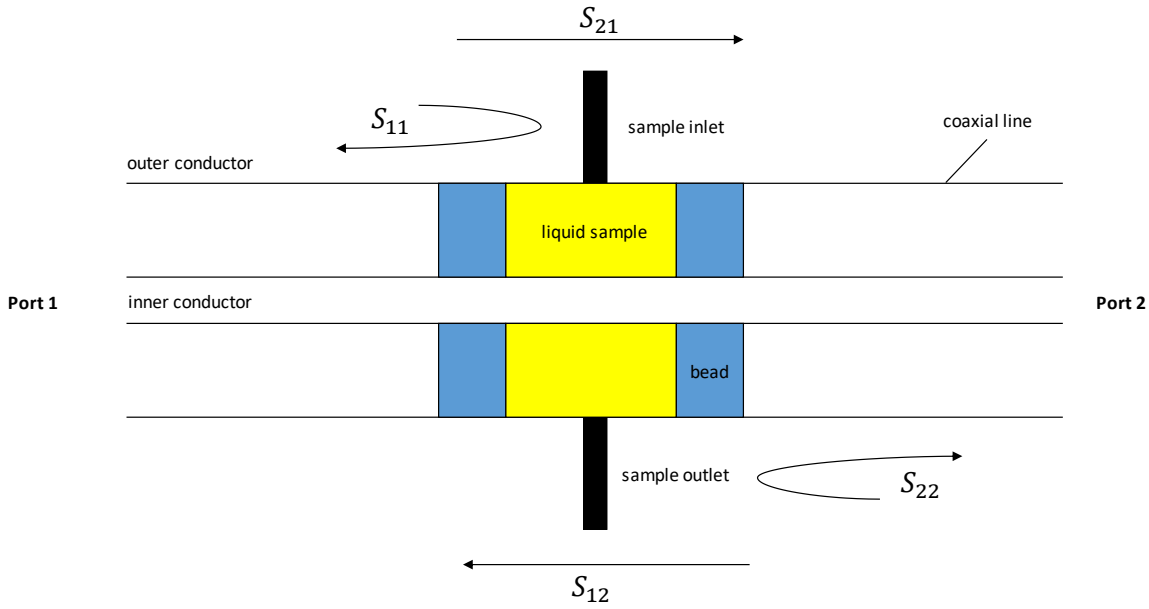

Figure 3.2 Illustration of a coaxial transmission sensor for dielectric measurement of liquids

For a nonmagnetic material, any one of the four S-parameters can be used individually to calculate the complex permittivity of the specimen but approaches that use more S-parameters can yield smaller uncertainties [68]. Comparisons of uncertainties of various transmission line based liquid measurement techniques, viz. Roberts and von Hippel cells, coaxial transmission cells, discontinuous inner conductor cells, open-ended coaxial probes, along with a low-frequency capacitance cell, are reported in [83]. It is observed that at operating frequencies in the order of GHz, transmission cells provide the smallest uncertainties in measurement of ε_r', when the transmission coefficient of the cell is used.

There have also been various waveguide-based transmission methods for the measurement of complex permittivity discussed in the literature [84-85]. Coplanar waveguides allow the fabrication of miniature transmission sensors [86-87]. Such sensors can be

manufactured to be less than 1 cm in length, allowing a smaller volume of sample to be used. They have, however, been found to suffer from high radiation and conduction losses. A method utilizing a stripline transmission cell which contains two planar conductors sandwiching a circular central conductor has been reported in [88]. Another stripline-based transmission technique has been demonstrated in [89] and has succeeded in distinguishing between picomolar concentration of nucleic acids in macromolecules. This method relies on changes in transmitted power to make the distinction in concentration. The authors state that such a measurement is subject to dispersions and nonlinearities of the stripline, making it impossible to exactly interpret the polarization of the molecular system. Thus it is unable to provide the complex permittivity of the sample.

In general, transmission methods are more accurate and have lower uncertainties compared to their reflection counterparts. Interfacing the sample with the sensor is much more convenient for reflectometric sensors, however, thus making the open-ended coaxial probe the most widely used sensor for microwave dielectric spectroscopy. Further discussions on different kinds of broadband dielectric spectroscopy sensors, and their advantages and limitations, can be found in the reviews [45] and [68]. The use of broadband dielectric spectroscopy to study the interaction between molecules of dielectric materials, and their molecular structure, have been presented in detail in [90].

3.3 Resonant Dielectric Measurement Methods

As the name suggests, resonant dielectric measurement methods employ resonators or resonant cavities to infer the complex permittivity of samples from the measurement of resonant frequency and Q-factor. This may be done with the use of perturbation theory which was

introduced by Waldren in [91]. Given a resonator designed to resonate at a particular frequency and a sample with much smaller volume than the resonator, introduced to it, perturbation theory can be employed to infer the real part of the permittivity of the sample from the observed shift in resonant frequency, whereas the imaginary part of the permittivity can be inferred from the change in Q-factor of the resonator [92].

One of the most common types of resonator found in the literature of dielectric measurement is the cylindrical cavity resonator, which is generally used as a TM_{010}, TE_{011}, or a reentrant cavity [44]. The lowest resonant mode of a cylindrical cavity is the TM_{010} mode. In this mode, the electric field lines points in a direction parallel to the axis of the cylinder, as shown in Figure 3.3, and decreases in the radial direction. Hence, this mode can be perturbed by

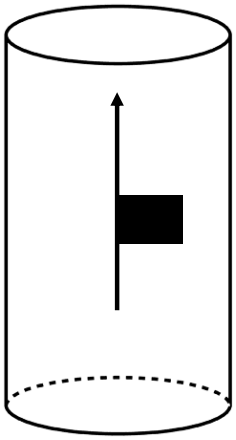

Figure 3.3 Direction of the electric field vector in TM_{010} mode of a cylindrical metal cavity resonator

a cylindrical sample inserted along the axis.

The TM_{010} cylindrical metal cavity has been demonstrated for dielectric measurements in [93-94]. This method is not suitable for lossy samples because, unless the volume of the sample is very small, it dampens the resonance heavily. This is due to the fact that the sample is placed

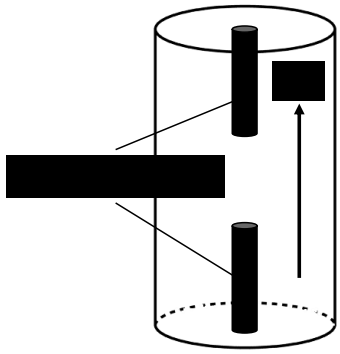

Figure 3.4 Illustration of a reentrant cylindrical cavity resonator

in the maximum electric field region of the cavity [68]. This can be avoided using a cylindrical cavity in the TE_{011} mode in which the sample is placed in the minimum field region. One such implementation is reported in [95]. Employing this mode is particularly convenient for making measurements on disc-shaped samples, but these are not always possible to make or obtain. Also, the fact that the TE_{011} mode is degenerate with TM_{111} mode calls for the need of additional filtering [44]. Reentrant cavities, as demonstrated in Figure 3.4, are similar to TM_{010} cavities, but have an additional protruding inner conductor. This leads to the region around the protruding inner conductor having an inductive behavior, and the gap in between having a capacitive behavior, enabling the analysis of the resonator with a simple equivalent LCR circuit [96]. The presence fringing capacitances at the end of the protruding inner conductor, however, may cause large uncertainties. In [97], the authors use numerical modeling to remove the effect of the fringing electric fields. Rectangular cavities have also been used by researchers for dielectric metrology [98].

Dielectric resonators have also been explored as a resonant technique for permittivity measurement. These resonators, which are generally formed of materials with high permittivity

and low loss, are most commonly operated in the $TE_{01\delta}$ mode [99], followed by the whispering gallery mode [100], and as split-post resonators [97]. The lowest cutoff frequency mode is $TE_{01\delta}$, which incorporates a dielectric cylinder which has a height much smaller than the half wavelength at its resonant frequency. There is propagation of waves along the axis of the dielectric resonator, but the field decays rapidly at the edges due to the high permittivity of the material. The fact that the field is not confined strictly inside the resonator allows for non-invasive coupling of such a sensor, as opposed to a sensor implementing a metal cavity. The whispering gallery mode operates on the total internal reflection of a wave inside the dielectric resonator. It generally occurs at frequencies much higher than the low gigahertz region where dielectric relaxations of many liquids are typically observed [44], making it unsuitable for metrology of those liquids. In [100], the authors demonstrate whispering gallery mode resonances at 26 GHz and 170 GHz. A split-post resonator is formed of two dielectric resonators with one of their flat edges parallel, hosted inside a metal cavity. Its ease of construction leads to its high popularity in dielectric measurement applications [44]. Figure 3.5 is taken from [101] and it illustrates the structure of a split-post resonator, where a sample under test is sandwiched between two dielectric resonators, enclosed in a metal cavity. Dielectric resonators, in general, tend to have higher sensitivity than cavity resonators. Also, unlike cavity resonators, invasive coupling in not a necessity. The requirement of disc-shaped samples, however, poses challenges in perturbing it with liquid samples which require the use of sophisticated microchannel designs.

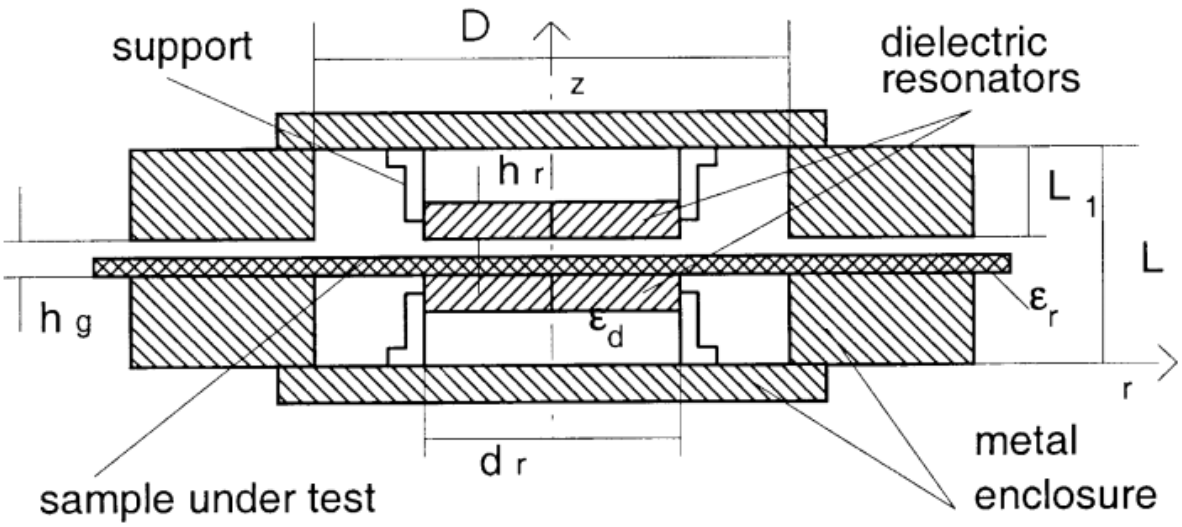

Figure 3.5 Split Post Resonator with two dielectric disk resonators of diameter d_r, height h_r, and permittivity ε_d sandwiching a sample of permittivity ε_r (taken from [101])

A rather simple resonator design that has been used by researchers to characterize dielectric liquids is the coaxial resonator, operating in its dominant TEM mode. A half-wavelength shorted section or a quarter wavelength open ended section of a coaxial transmission line behaves in a manner similar to a series resonator (series combination of a lumped resistor, capacitor, and inductor), whereas a half-wavelength open ended section or a quarter wavelength shorted section of a coaxial transmission line behave similarly to a shunt resonator (parallel combination of a lumped resistor, capacitor, and inductor). A technique employing a shorted TEM coaxial resonator which uses a capillary tube to introduce the sample into the resonator has been developed in [102]. The technique is extended to make broadband measurements by changing the length of the inner conductor. An open-ended $\frac{\lambda}{4}$ coaxial resonator has been used in [103] to measure the content of liquid water in snow, using permittivity calculations. An open ended half-wavelength coaxial resonator has been developed in conjunction with a novel coupling structure, to implement weak capacitive coupling, to take transmission measurements

of the resonance while not loading the resonator [104-105]. The resonator is perturbed using a capillary in [104], whereas an evanescent perturbation was realized in [105]. A liquid filled coaxial stub which acts as a quarter-wavelength resonator has been used to measure the permittivities of water, ethanol, and glycerol [106].

Other resonator topologies, such as split-ring resonator [107], hairpin resonator [108], and YIG resonator [65] have also been reported in literature. A microstrip patch antenna sensor is used in [109] to predict the concentration of glucose in blood samples.

3.4 Other Microwave Dielectric Measurement Methods

There has been some work done in microwave dielectric metrology to characterize liquid samples using admittance cells, a technique which is more prevalent at frequencies lower than 10 MHz [110-111]. This method is useful in measuring the dc permittivity of liquids [112], but suffers from the critical drawback of exhibiting the interfering electrode polarization effect [113].

Time-domain methods, which deal with transient responses of specimens to determine their dielectric properties, have also been explored by researchers. Such methods can be broadly classified into two types – one in which the sample is assumed to be a lumped impedance, and the other in which it is assumed to be a distributed impedance [114]. The latter kinds of technique are referred to as Time Domain Reflectometry (TDR) methods. Knowledge of the dielectric properties of a sample in the time domain can be transformed to find its dielectric dispersion over a frequency spectrum using the Fourier Transform of the signal used to stimulate the sample. Further discussion of time domain methods can be found in [115-116].

3.5 Choice of Dielectric Measurement Method for Current Problem

As mentioned before, the choice for the dielectric measurement method on which the sensor herein would be designed depends on a number of factors, viz. low cost, high sensitivity, high portability, capability of making real time measurements, and being nondestructive and field deployable. This would also require the sensor to interface well with the sample.

The electrophoretic effect of admittance cells, and the uncertainties posed by time-domain methods due to imperfect pulses, along with high costs, render those classes of methods unsuitable for a high sensitivity sensor. Of all the different kinds of sensors available in the literature, broadband methods seem to be the most popular choice for making dielectric measurements of liquids. The relatively high cost of VNAs, the requirement of a VNA by most broadband dielectric spectroscopy methods, and their strong dependence on careful VNA calibration, however, make them a less favorable contender for the problem herein [97]. Also, broadband methods have lower sensitivity than resonant methods because of lower signal-to-noise ratio [43]. This does not mean that resonant sensors are always a better choice compared to their broadband counterparts, when it comes to selecting a technique for measuring dielectric properties of a sample. One major drawback of the resonant methods is that they can make dielectric measurements only at their fundamental resonant frequency and its integer multiples which correspond to higher modes of resonance. Since the goal of the current research is to devise a system which can relate a change in concentration of ions in water to a change in resonant frequency, and the fact that the permittivity of a typical sample solution does not change much with frequency until a relaxation occurs, designing a resonant method to operate at an

optimum frequency should suffice. The optimum frequency would come from a tradeoff between the resonator size and the resonator sensitivity.

The need for having a field deployable sensor eliminates cavity based resonators which require the sample to be inserted into the cavity. The most suitable topology for a low cost, highly sensitive, real time, nondestructive, field deployable sensor appears to be a simple open-ended coaxial transmission line resonator, which can be perturbed evanescently by the sample at the open end. A similar design is used by the authors in [61], and the work has been closely followed to come up with the approach for the current problem.

CHAPTER 4. DESIGN OF EVANESCENTLY PERTURBED RESONANT SENSOR

This chapter explores the design procedure adopted to build an evanescently perturbed resonant sensor for measuring ionic concentration of aqueous solutions. The design has been aimed to make the sensor highly sensitive to changes in ionic concentration, while keeping its size physically small (around 10 cm). Sections 4.1 and 4.2 discuss transmission line resonator theory and resonator perturbation theory respectively, which provide insights into the operating principle of the sensor. Section 4.3 presents an argument for choosing the dimensions of the resonator for the current work.

To measure a change in ionic concentration, it is also important to address how the frequency information from the resonator can be reliably measured. This calls for the need of a suitable coupling technique in between the resonant sensor and an instrument which can measure the resonant frequency. For this purpose, different coupling strategies are discussed in Section 4.4, and the one deemed most appropriate is chosen for the design. Simulations based on Finite Element Analysis are further used to choose the optimized dimensions of the coupling structure.

4.1 Transmission Line Resonator Theory

A section of a transmission line is said to resonate, when its boundary conditions allow for an incident wave to be reflected repeatedly from the ends to form a standing wave by constructive interference. This condition manifests itself as the input impedance or the input admittance to the section of the transmission line being purely real. Considering a lossless section of transmission line of length L and characteristic impedance Z_0, which is terminated by an arbitrary load impedance Z_L, as shown in Figure 4.1, its input impedance Z_{IN} is given by:

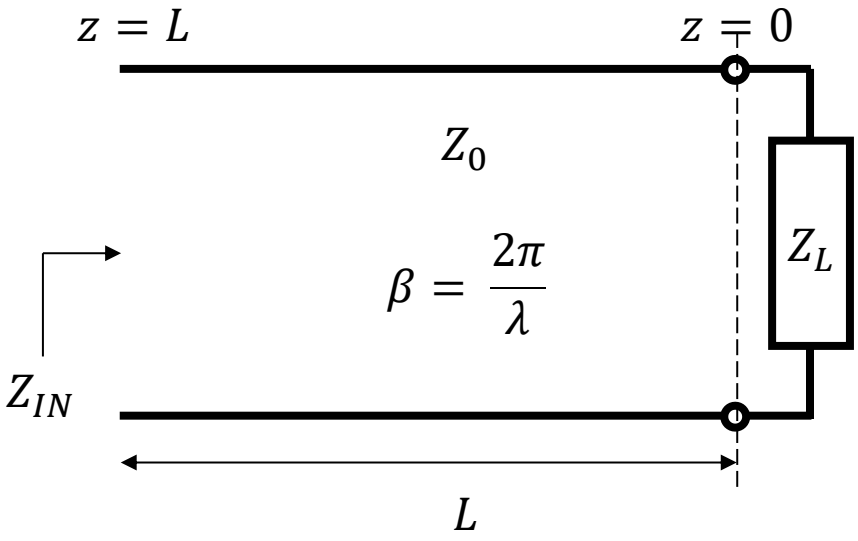

Figure 4.1 Transmission line terminated with an arbitrary load

$$Z_{IN} = Z_0 \frac{1+\Gamma^{-2j\beta L}}{1-\Gamma^{-2j\beta L}} \tag{4.1}$$

In Equation (4.1) β is the wavenumber of the wave propagating in the transmission line. Writing Equation (3.1) in terms of impedances, $\Gamma = \frac{Z_L - Z_0}{Z_L + Z_0}$, and plugging it into Equation (4.1),

$$Z_{IN} = Z_0 \frac{Z_L + jZ_0 \tan(\beta L)}{Z_0 + jZ_L \tan(\beta L)} \tag{4.2}$$

When the above section of transmission line is open circuited, $Z_L \rightarrow \infty$, making $\Gamma = 1$. This condition simplifies Equation (4.2) to give

$$Z_{IN,open-circuited} = -jZ_0 \cot(\beta L) \tag{4.3}$$

$$Y_{IN,open-circuited} = -jY_0 \tan(\beta L) \tag{4.4}$$

This leads to two possible resonance conditions, one for real input impedance, and another for real input admittance. Since the transmission line used in this analysis is lossless, the resonance conditions translate to zero input impedance and zero input admittance, respectively.

Focusing on the latter case, it is observed from Equation (4.4) that the resonance condition is satisfied when $\tan(\beta L) = 0$, or $\beta L = n\pi$, where n is a positive integer. Using $\beta = \frac{2\pi}{\lambda}$, it is found that for resonance,

$$L = \frac{n\lambda}{2} \tag{4.5}$$

This condition corresponds to the open circuit being at a distance from the input where the incident electric field has the maximum amplitude whereas the incident magnetic field is zero. In terms of voltage and current, this translates to maximum voltage and zero current at the open end, allowing for the formation of standing waves in the section of the transmission line.

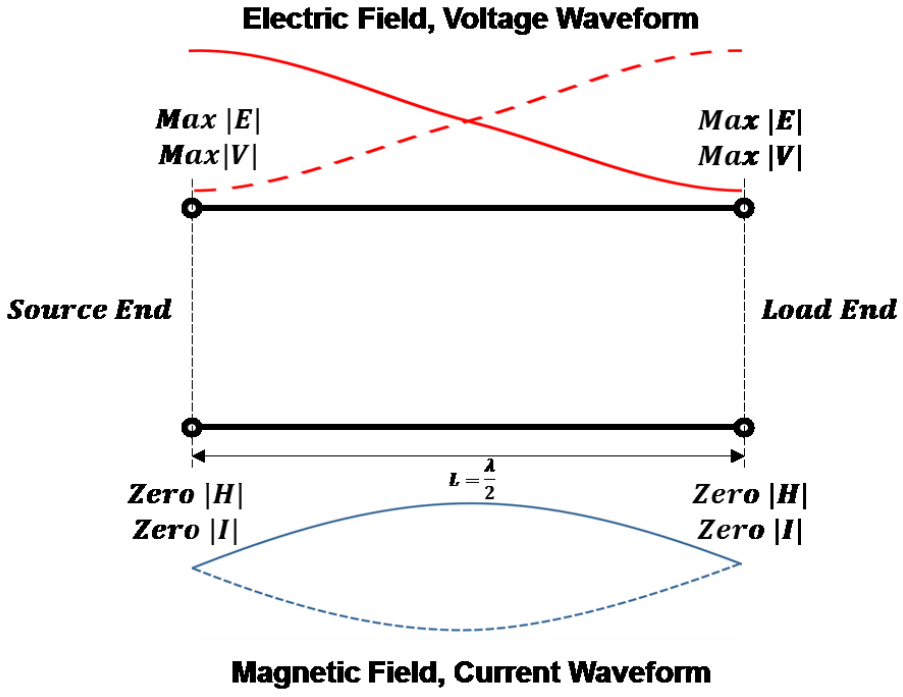

Figure 4.2 Half wavelength open circuited transmission line

The half-wavelength open circuited resonance condition is analogous to the resonance observed in a half-wavelength open ended air column. Longitudinal pressure waves are reflected from the open end to form standing waves when the length of the air column is an integer multiple of the half wavelength of sound. In terms of the behavior of its input admittance (or impedance), a half wavelength open circuited transmission line resonator behaves similar to a shunt RLC (resistor-inductor-capacitor) network.

A resonance condition can also be found when the termination is a short circuit for a half wavelength section of a transmission line. In this case, the magnetic field is maximum at the load end, whereas the electric field is zero. The input impedance of such a transmission line section is purely real (zero if lossless), and this behavior is similar to that of a series RLC network.

The conditions for resonance can also be satisfied using a quarter-wavelength transmission line. An open circuited quarter wavelength transmission line behaves like a series RLC resonator, whereas a short circuited quarter wavelength transmission line behaves like a shunt RLC resonator. Table 4.1 lists the different conditions for resonance in short circuited and open circuited sections of a lossless transmission line. A detailed discussion on the theory of microwave resonators can be found in [63].

Table 4.1: Resonance conditions for short circuited and open circuited lossless transmission lines

Termination	Length	Input Impedance at Resonance	Input Admittance at Resonance	Circuit Equivalent
Short Circuit	λ/2	$Z_{IN} = 0$	$Y_{IN} = \infty$	Series RLC
Open Circuit	λ/2	$Z_{IN} = \infty$	$Y_{IN} = 0$	Shunt RLC
Short Circuit	λ/4	$Z_{IN} = \infty$	$Y_{IN} = 0$	Shunt RLC
Open Circuit	λ/4	$Z_{IN} = 0$	$Y_{IN} = \infty$	Series RLC

It is worth mentioning that these resonances are Transverse Electromagnetic (TEM), as there is no electric or magnetic field component in the wave propagation direction. There can be Transverse Electric (TE) and Transverse Magnetic (TM) modes of resonance in transmission lines, like in waveguides, but these modes have a large cutoff frequency. In order to operate a transmission line resonator in TEM mode, the frequency of operation should be maintained low enough for the other modes to not interfere.

Open Ended Coaxial Transmission Line Resonator

A coaxial transmission line, or a coaxial cable, or simply a coax, is a type of a transmission line with a cylindrical inner conductor surrounded by a tubular dielectric layer, which in turn, is surrounded by a tubular outer conductor. Given the radius of the inner conductor a, the radius of the inner surface of the outer conductor b, and dielectric constant $\varepsilon_m{}'$ of the dielectric layer (assumed to be nonmagnetic), the characteristic impedance Z_0 can be computed using the following relationship:

$$Z_0 = \frac{\eta_0}{2\pi\sqrt{\varepsilon_m{}'}} \ln\left(\frac{b}{q}\right) \tag{4.6}$$

In Equation (4.6), η_0 stands for the intrinsic impedance of vacuum (approximately 377 Ω). The electric and magnetic field patterns inside a coaxial transmission line operating in TEM mode is illustrated in Figure 4.3.

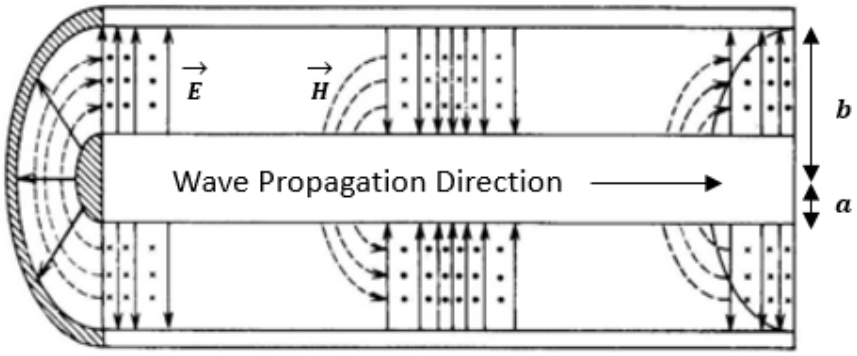

Figure 4.3. Electric and magnetic field patterns inside a coaxial cable in TEM mode (redrawn from [117])

Coaxial transmission lines find a plethora of applications in the RF communication industry, such as feedlines from antennae to transmitter and receiver circuits, television networks, and RF connectors. The electromagnetic field which carries the signal is completely confined in between the two conductors. This provides protection from external interference. Coaxial cable systems are broadband, have large channel capacity, and low error rates [118]. The fact that the open end of a coaxial cable can be easily interfaced with a liquid sample under test to evanescently perturb a coaxial resonator renders the geometry suitable for the current purpose. The resonant frequency of an open ended section of a coaxial line of length L operating in TEM mode, acting as a half-wavelength resonator , can be found as follows:

$$f = \frac{v}{\lambda} = \frac{c}{\sqrt{\varepsilon_m'}\lambda} \tag{4.7}$$

For a half wavelength resonator, using $\lambda = \frac{2L}{n}$ from Equation (2.5).

$$f = \frac{nc}{2L\sqrt{\varepsilon_m'}} \tag{4.8}$$

In Equation (4.7), c denotes the phase velocity of the electromagnetic wave in free space (approximately 3×10^8 m/s), and v stands for the phase velocity inside the dielectric of the coaxial line.

From equation (4.9), it can be observed that there are multiple TEM modes of resonance of the coaxial resonator, each denoted by a different positive integer value of n. The lowest resonant frequency (for $n = 1$) is known as the fundamental mode resonant frequency of the coaxial resonator, and all the other resonant frequencies, called harmonics, are integer multiples of the fundamental mode resonant frequency. To distinguish the different TEM modes of resonance of the resonator, the subscript n is introduced, and Equation (4.8) is rewritten as

$$f_{n-1} = \frac{nc}{2L\sqrt{\varepsilon_m'}} \tag{4.9}$$

Using this notation, the fundamental mode resonant frequency is given by

$$f_0 = \frac{c}{2L\sqrt{\varepsilon_m'}} \tag{4.10}$$

In the discussions henceforth, the notations f_r has been used to represent a generic frequency of resonance.

Under the influence of a sample interfaced at the open end of the coaxial resonator, the resonant frequencies of the resonator are expected to shift according to the dielectric properties of the sample. Since the dielectric properties of an aqueous solution depend on the ion type and ion concentration, the shift in resonant frequencies can be utilized to infer the ion concentration, given the ion type. The following section talks about resonator perturbation theory, which explores the effect of perturbation by a small volume of a sample with known dielectric properties on the resonator characteristics of the resonator.

4.2 Resonator Perturbation Theory

Perturbation theory describes the effect of introducing a piece of an external material to a resonator, or changing the shape of a resonator on its resonant characteristics, and was first introduced by Bethe and Schwinger in 1943 [119]. In 1960, Waldron gave a detailed perturbation formula to find the shift in resonant frequency of a resonant cavity by the introduction of a ferrite or dielectric sample, with necessary approximations [91]. Although initially developed for analysis of perturbations in cavity resonators in terms of shape, permittivity, or permeability, open ended coaxial resonant sensors based on resonator perturbation theory has been demonstrated in literature [92,102].

For a perturbation by a sample which changes the complex permittivity of the region which the resonator field occupies by $\Delta\varepsilon$ from the unperturbed case (ε_{orig}), the resonant frequency can be found to change according to the following equation:

$$\frac{\omega_c - \omega_{c,orig}}{\omega_c} = \frac{\int \Delta\varepsilon \vec{E}.\overline{E_{orig}}\, dv}{\int_V (\varepsilon_{orig} \vec{E}.\overline{E_{orig}} + \mu \vec{H}.\overline{H_{orig}})\, dv} \tag{4.11}$$

In Equation (4.11), the subscript '$orig$' has been used to denote the unperturbed quantities, μ denotes the permeability of the region, while $\vec{H}$ represents magnetic field, and ω_c is a complex quantity whose real part represents the angular resonant frequency ω_r (where $\omega_r = 2\pi f_r$), and the imaginary part denotes negative of the half 3dB angular frequency ω_{3db} [44].

$$\omega_c = \omega_r - j\frac{1}{3}\omega_{3dB} \tag{4.12}$$

It is assumed that the sample does not change the permeability of the region occupied by the resonator fields. If a further assumption is made that the perturbation in complex permittivity

is small, i.e. the perturbation does not disturb the field distribution inside the resonator, Equation (4.11) can be simplified to get the relationships in the following form:

$$\frac{\omega_c - \omega_{c,orig}}{\omega_c} \propto \Delta\varepsilon \tag{4.13}$$

Separating out the real and imaginary parts of Equation (4.13) predicts a linear relationship between the change in resonant frequency normalized to the unperturbed resonant frequency and the change in sample polarizability, whereas change in the bandwidth of the resonance normalized to the bandwidth of the unperturbed resonance is linearly related to the change in dipolar loss.

It is important to note, however, that Equation (4.11) considers that the sample perturbation changes the permittivity of the entire resonator by $\Delta\varepsilon$, and calculating the change is complicated for the open ended coaxial resonator discussed in this work. Also, since for the aqueous solution samples being used in this work, the imaginary part of permittivity changes significantly with concentration, the approximation that the field patterns inside the resonator remain constant is no longer expected to be valid, thus leading to a nonlinear behavior. Nevertheless, the fact that the complex permittivity at any given frequency of the ionic solutions under test varies with concentration implies that that the complex permittivity of the region occupied by the resonator field changes with concentration. Hence, even though an exact prediction of the relationship cannot be made at this stage, it is reasonable to expect to observe a change in resonant frequency with the change in ionic concentration.

4.3 Choice of Resonator Dimensions

The two preceding sections have explored the theory of transmission line resonators and how a change in the sample interfaced with an open ended coaxial resonant sensor can have an impact on its resonant characteristic. This chapter shifts the focus from the theory to finding optimal resonator dimensions for the current purpose. For finding the design dimensions, the following aspects are considered:

1. Length of the resonant sensor: It is undesirable to be make the resonator too long, as it would make it unsuitable for field deployment. This calls for constraining the maximum size of the resonator. Tile drainage pipe diameters vary from 2" to 18" [120]. Since 5" (approximately 12.7 cm) is one of the standard sizes for the diameter of a tile drainage pipe, a maximum of 12 cm is chosen as the maximum length of the resonant sensor.
2. Sensitivity of the resonant sensor to changes in ionic concentration: It is desired that the resonator is designed with dimensions for which it is the easiest to observe a change in resonant frequency of the sensor to a change in ionic concentration. It is worth mentioning that since the only dimension of a coaxial resonator which affects its resonant frequency is its length (axial dimension), this aspect calls for looking at resonator lengths for which sensitivity to change in concentration is maximized.
3. Loss: The most important sources of loss in the system are the lossy sample, conductivity of resonator dielectric, and imperfect conductivity of the conductors, along with geometric defects. The longer the section of the coaxial line used, the more is the impact of these imperfections. Hence, given a lossy coaxial transmission line, a shorter length is preferable for getting lower loss.

4. Cost: Since the focus of this research is to design a low cost sensor, it is preferable to use a low cost coaxial transmission line which is suitable for the current work. This cuts down the manufacturing cost of the entire sensor arrangement significantly, and also provides easy interfacing with the measurement instrument (VNA).
5. Robustness: It is also desired for a field deployable sensor to withstand changing environmental conditions.

Criteria 3 and 4 suggest the choice of an RG401 coaxial cable for the purpose of resonator design. It is a standard 50 Ω coaxial copper transmission line, with a polytetrafluoroethylene (PTFE) spacer. The advantage of using a PTFE dielectric is that its permittivity does not vary strongly with frequency, and is also thermally stable at environmentally relevant temperatures. According to the datasheet [55], an RG401 has an inner conductor diameter of 1.63 mm, dielectric spacer diameter of 5.31 mm, and outer shield diameter of 6.35 mm. These radial dimensions set the characteristic impedance of the coaxial line to 50 Ω, which facilitates easy interfacing with other microwave devices, which have a standard input impedance of 50 Ω. Also, an RG401 coaxial cable can be operated in the temperature range of -55 to 125 ºC, which encompasses all environmentally relevant temperatures across the year in Midwestern United States.

From Equation (4.9), it can be seen that the resonant frequency of a coaxial transmission line resonator is inversely proportional to its length. This sets a bound on the minimum frequency for which a resonator can be designed, keeping its size relatively small. For a 12 cm long section of an open-ended coaxial transmission line, the fundamental resonant frequency can be calculated by Equation (4.10), using $\varepsilon_m{}' = 2.1$ (dielectric constant of PTFE spacer). The fundamental resonant frequency comes out to be 862.58 MHz. This implies that for the resonant sensor to

have a length less than 12 cm, its resonant frequency in free space (without any sample) should be greater than 862.58 MHz.

Since the resonant frequency of the coaxial sensor depends on its length, it is worthwhile to investigate how the sensitivity of the complex permittivity of an aqueous solution sample to changes in ionic concentration varies with frequency. To facilitate that, using experimental data, the real and imaginary parts of the complex permittivity of an Na_2SO_4 solution in water has been plotted against changes concentration at eight different frequencies in Figure 4.4.

From the plots one can observe that for the lower frequencies of operation, the real part of permittivity is linearly decreasing with concentration, and the imaginary part of permittivity is linearly increasing with concentration. The response starts getting less linear as the frequency increases. To quantify the above, a linear function is fitted to each of the plots. The fitting parameters and norm of residuals are tabulated in Table 4.2. The norm of residuals is a dimensionless quantity representing the square root of the sum of squared residuals for a fitted curve; a lower value represents a better fit. This is followed by a discussion on the sensitivity of complex permittivity to changes in concentration at different frequencies. The sensitivity of a change in sample's real and imaginary permittivity to a change in ionic concentration at a given frequency can be defined as $|\frac{\partial \varepsilon_r'}{\partial c}|$ and $|\frac{\partial \varepsilon_r''}{\partial c}|$ respectively.

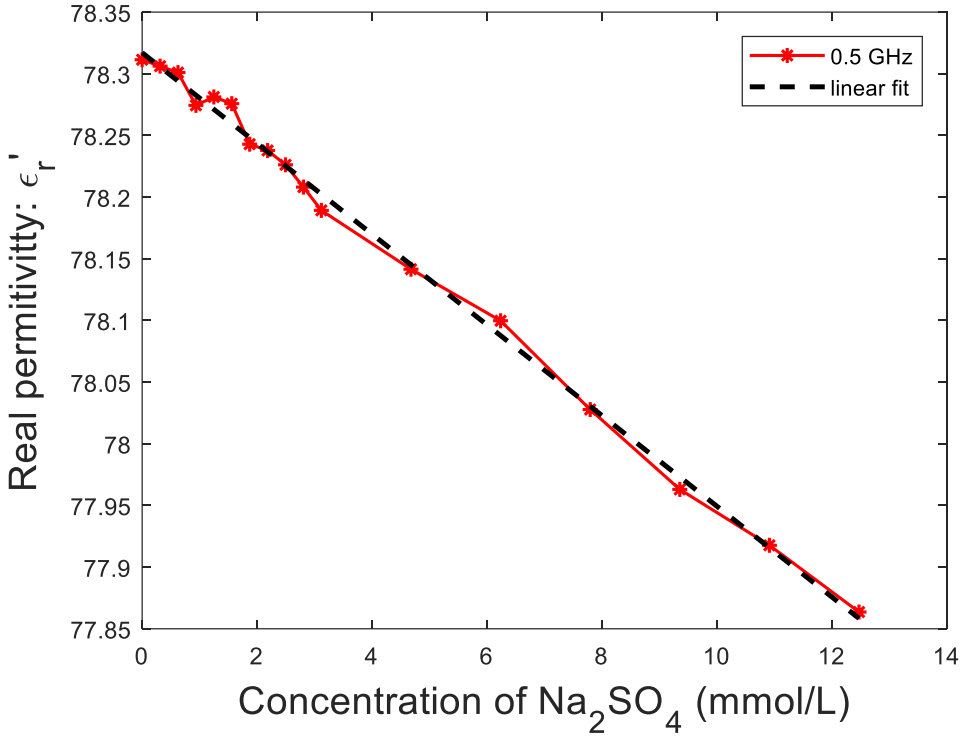

Fig 4.4 (a) Real permittivity $\varepsilon_r{}'$ vs concentration of Na_2SO_4 at 0.5 GHz

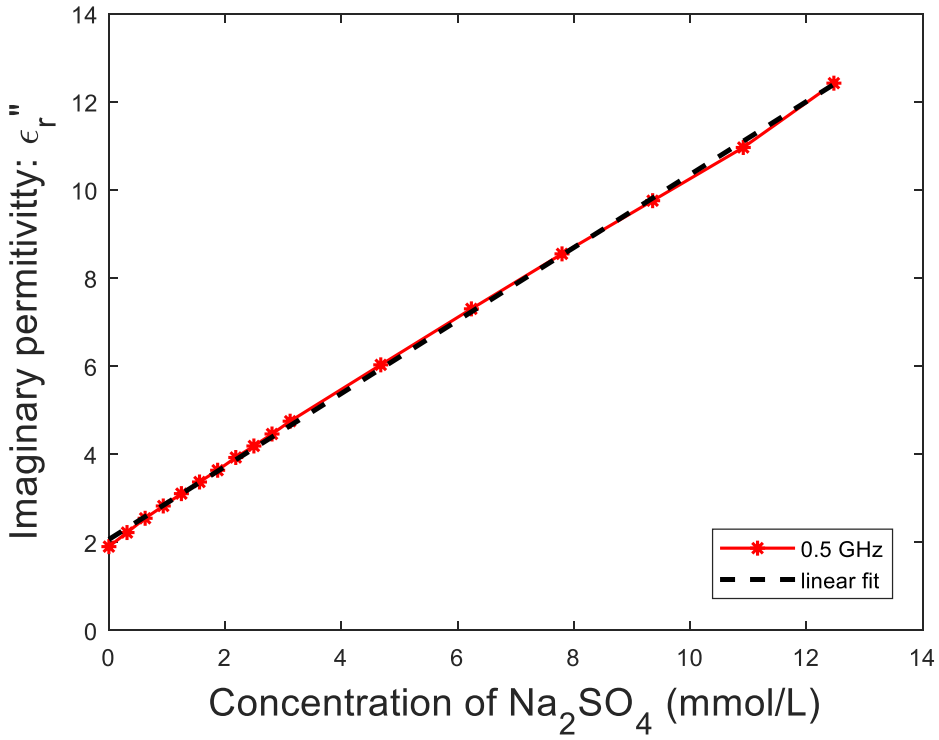

Fig 4.4 (b) Imaginary permittivity $\varepsilon_r{}''$ vs concentration of Na_2SO_4 at 0.5 GHz

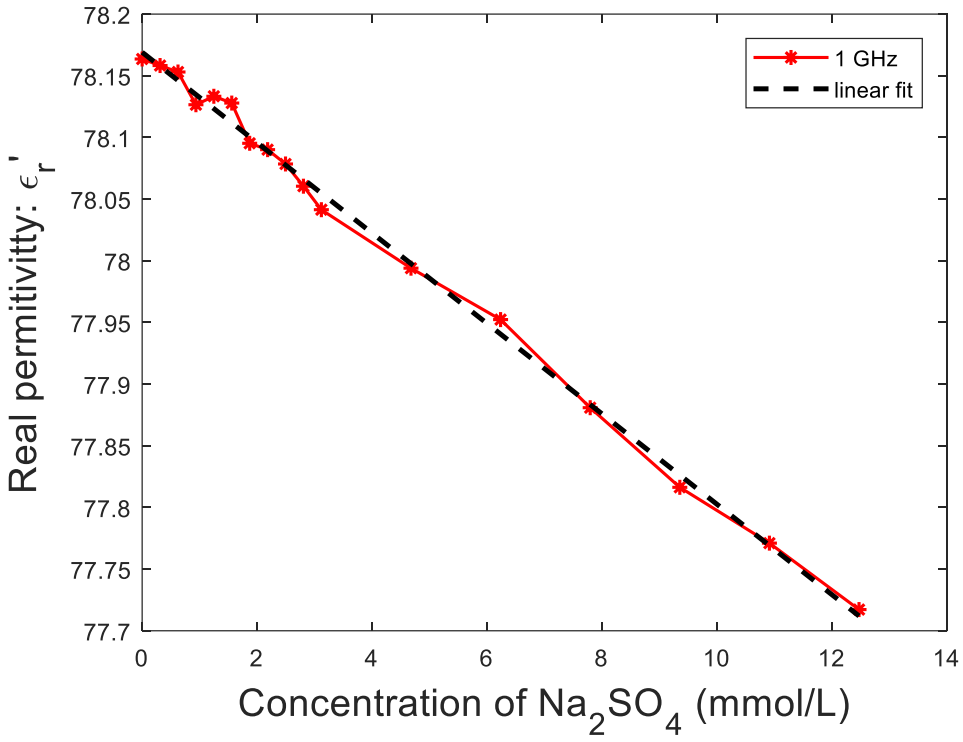

Fig 4.4 (c) Real permittivity $\varepsilon_r{}'$ vs concentration of Na_2SO_4 at 1.0 GHz

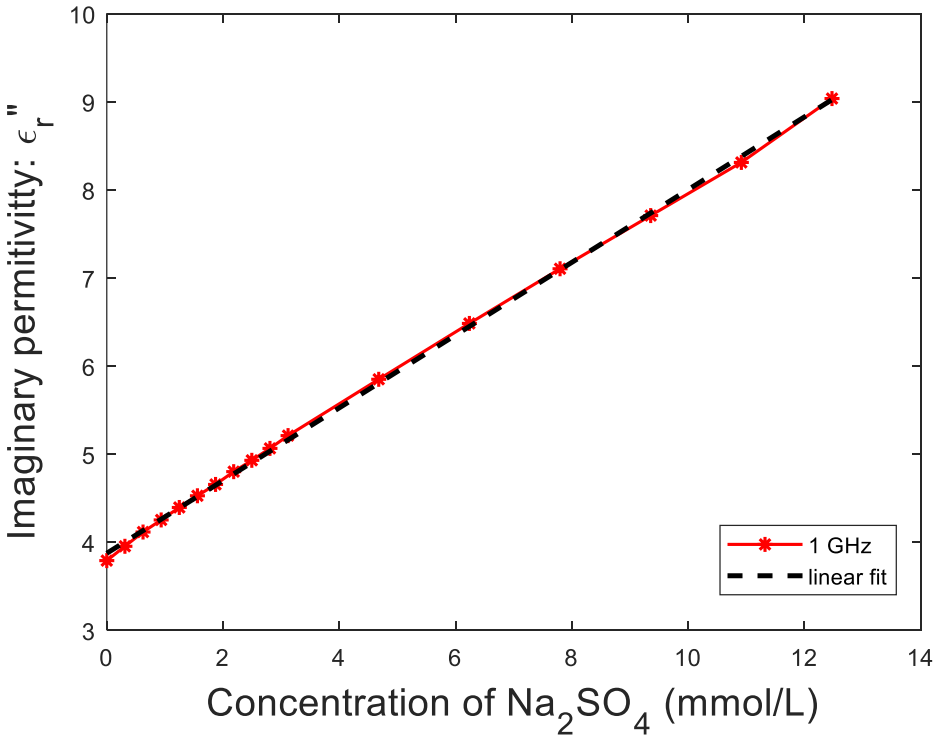

Fig 4.4 (d) Imaginary permittivity $\varepsilon_r{}''$ vs concentration of Na_2SO_4 at 1.0 GHz

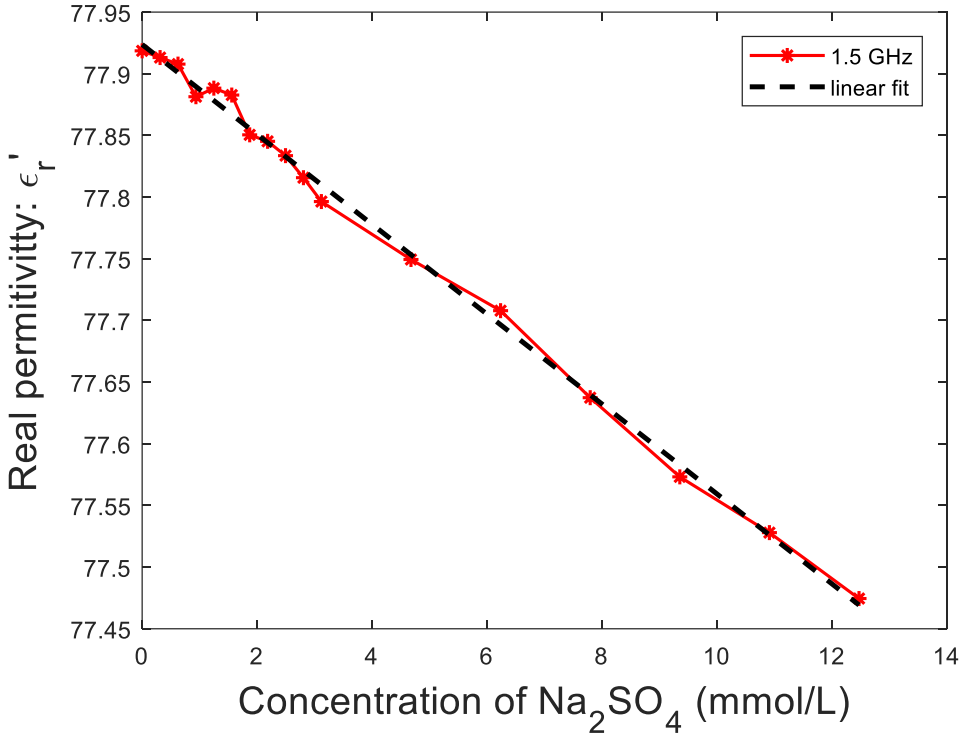

Fig 4.4 (e) Real permittivity $\varepsilon_r{}'$ vs concentration of Na_2SO_4 at 1.5 GHz

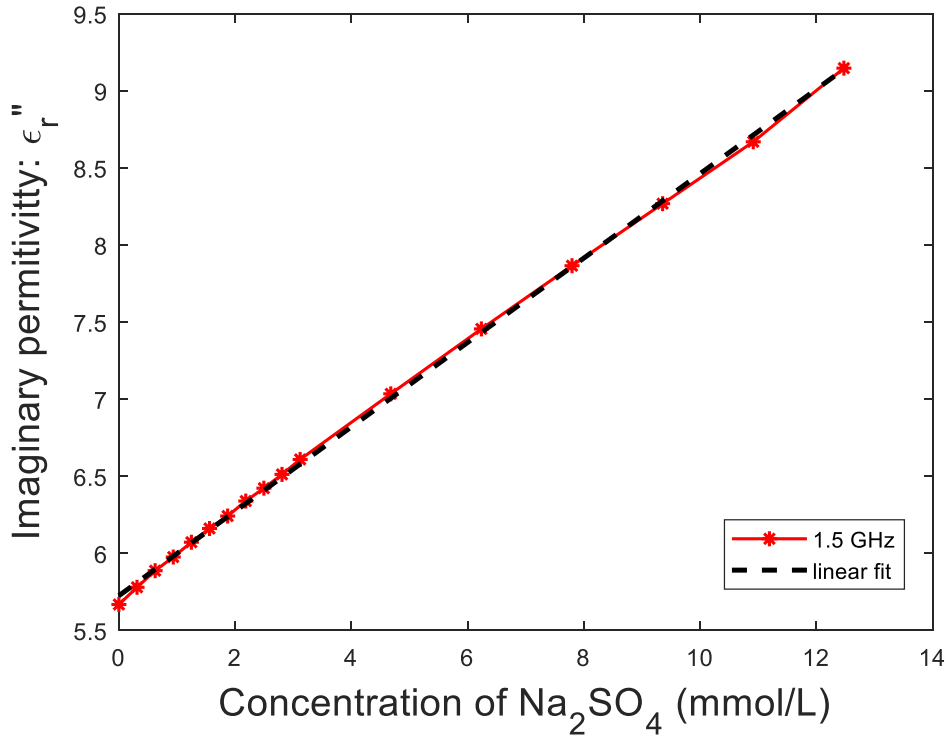

Fig 4.4 (f) Imaginary permittivity $\varepsilon_r{}''$ vs concentration of Na_2SO_4 at 1.5 GHz

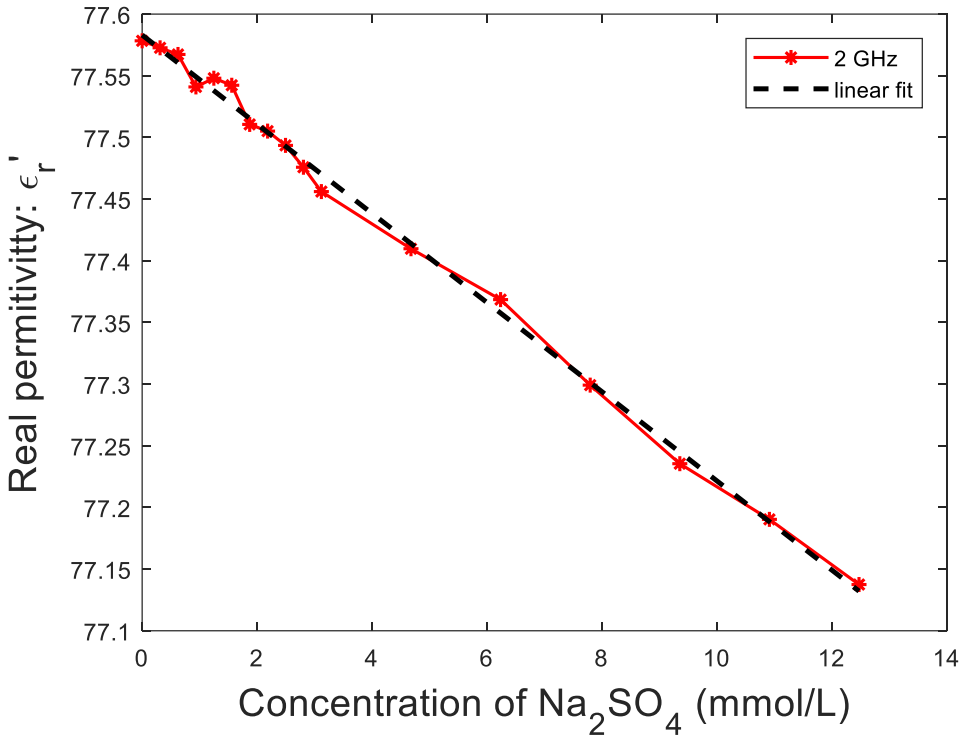

Fig 4.4 (g) Real permittivity $\varepsilon_r{}'$ vs concentration of Na_2SO_4 at 2.0 GHz

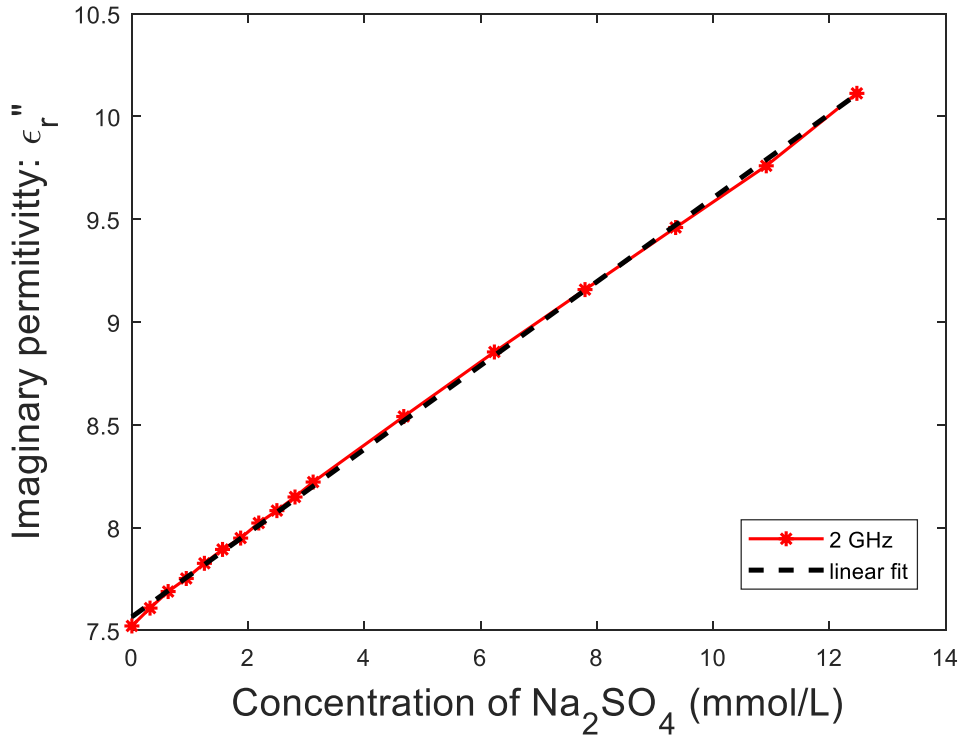

Fig 4.4 (h) Imaginary permittivity $\varepsilon_r{}''$ vs concentration of Na_2SO_4 at 2.0 GHz

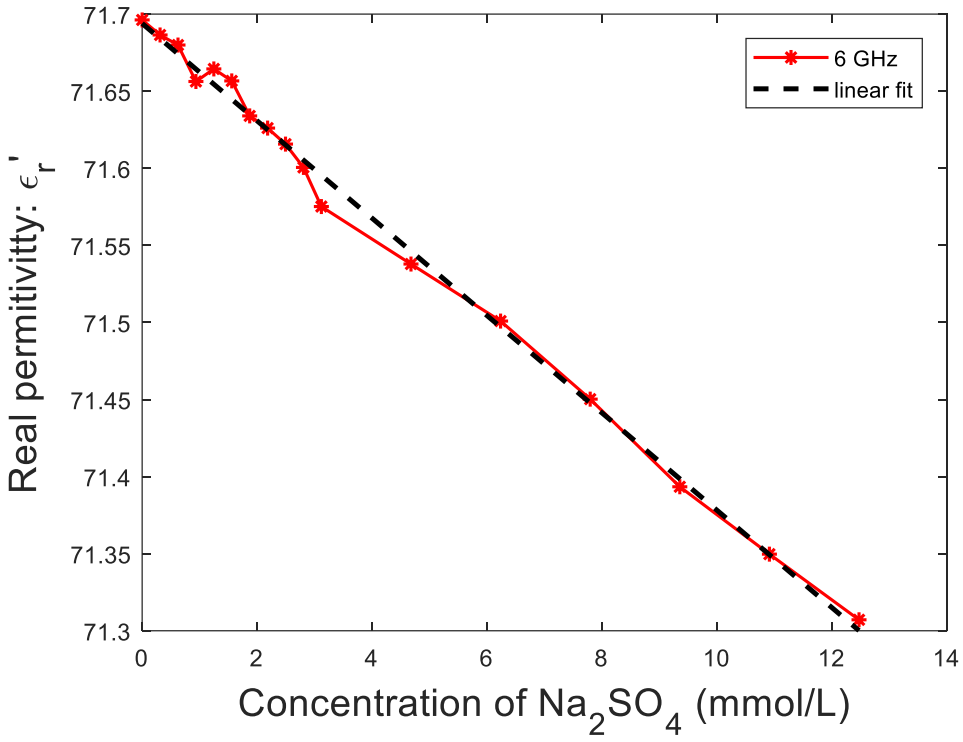

Fig 4.4 (i) Real permittivity $\varepsilon_r{}'$ vs concentration of Na_2SO_4 at 6.0 GHz

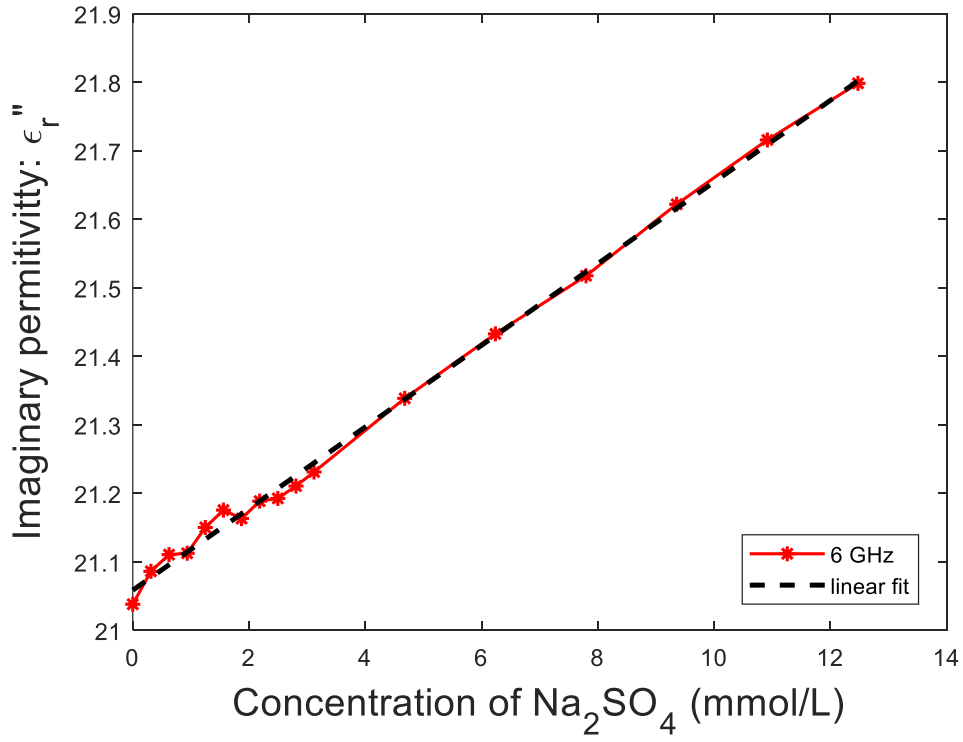

Fig 4.4 (j) Imaginary permittivity $\varepsilon_r{}''$ vs concentration of Na_2SO_4 at 6.0 GHz

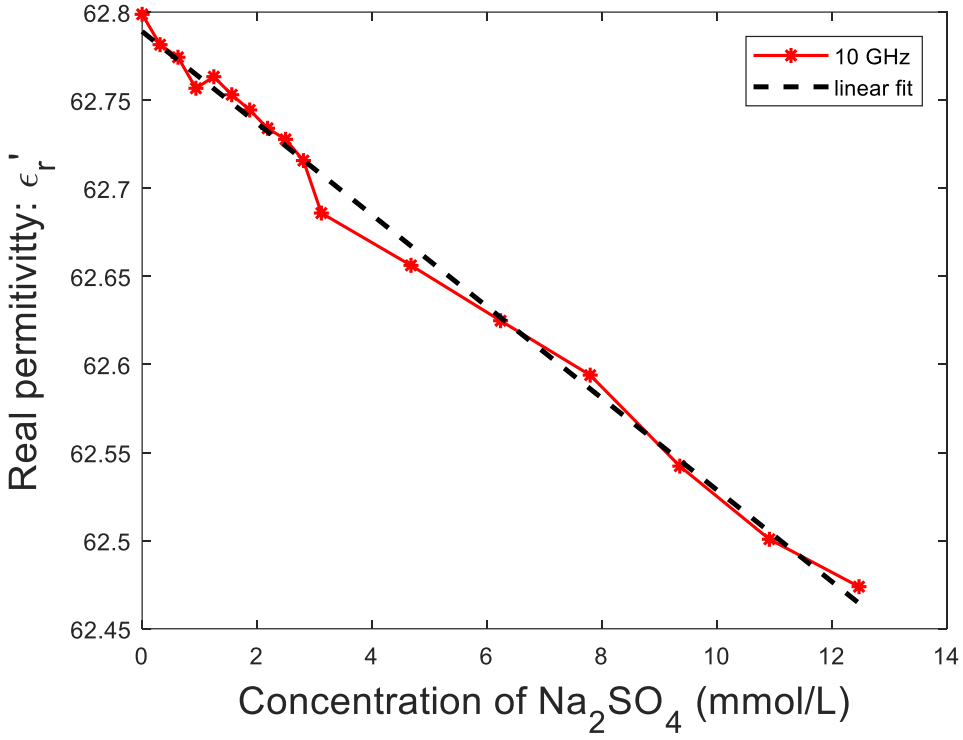

Fig 4.4 (k) Real permittivity $\varepsilon_r{}'$ vs concentration of Na_2SO_4 at 10.0 GHz

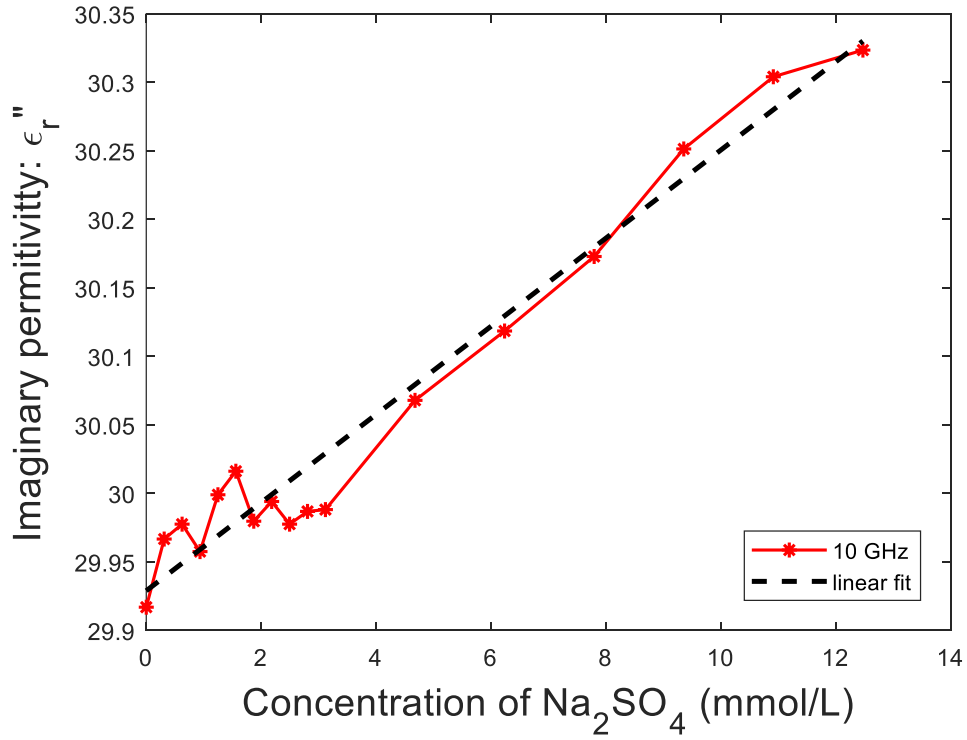

Fig 4.4 (l) Imaginary permittivity $\varepsilon_r{}''$ vs concentration of Na_2SO_4 at 10.0 GHz

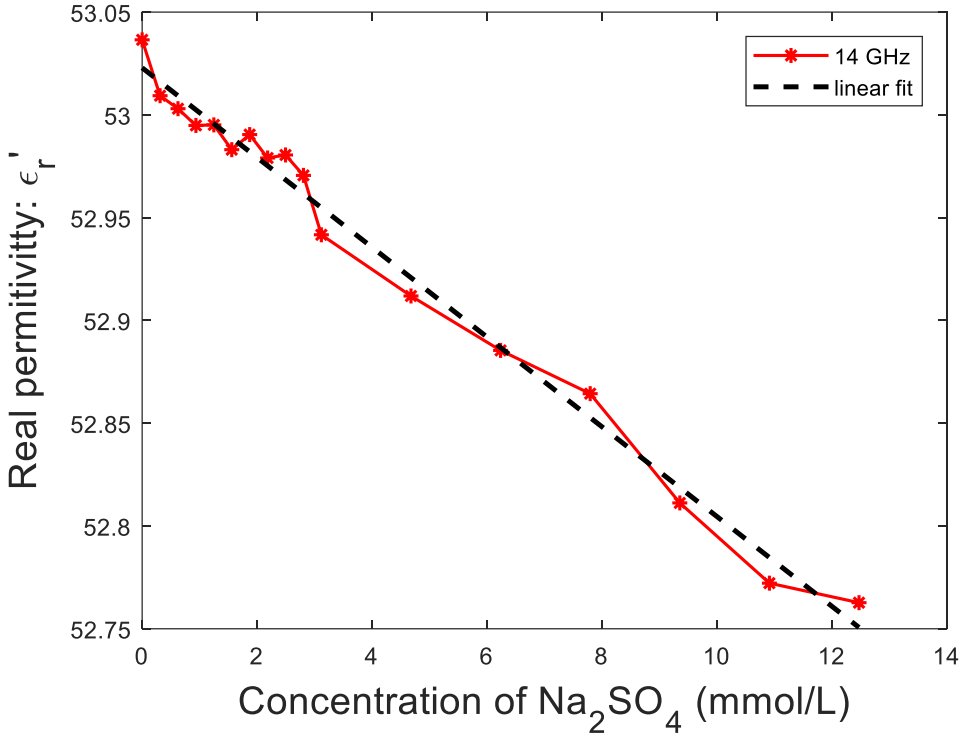

Fig 4.4 (m) Real permittivity $\varepsilon_r{}'$ vs concentration of Na_2SO_4 at 14.0 GHz

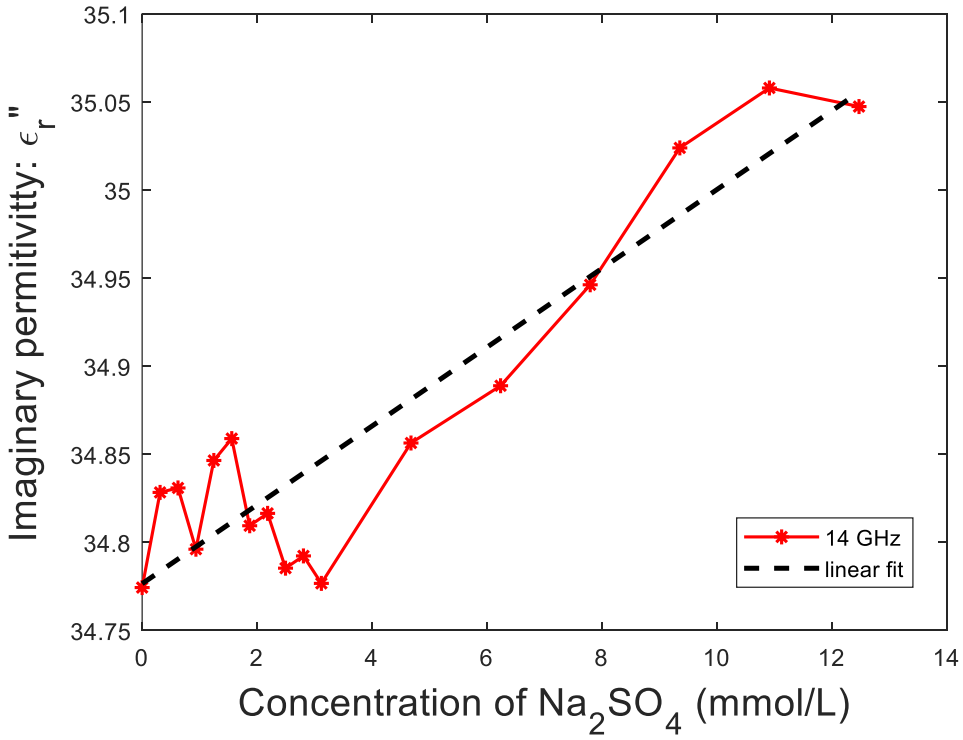

Fig 4.4 (n) Imaginary permittivity $\varepsilon_r{}''$ vs concentration of Na_2SO_4 14 GHz

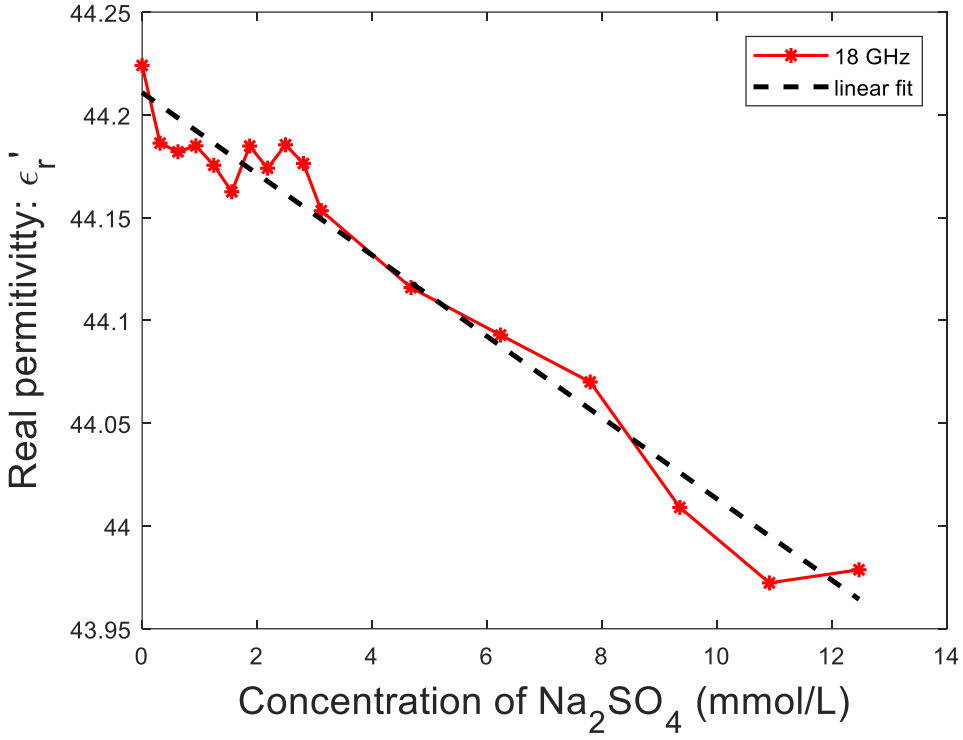

Fig 4.4 (o) Real permittivity $\varepsilon_r{}'$ vs concentration of Na_2SO_4 at 18.0 GHz

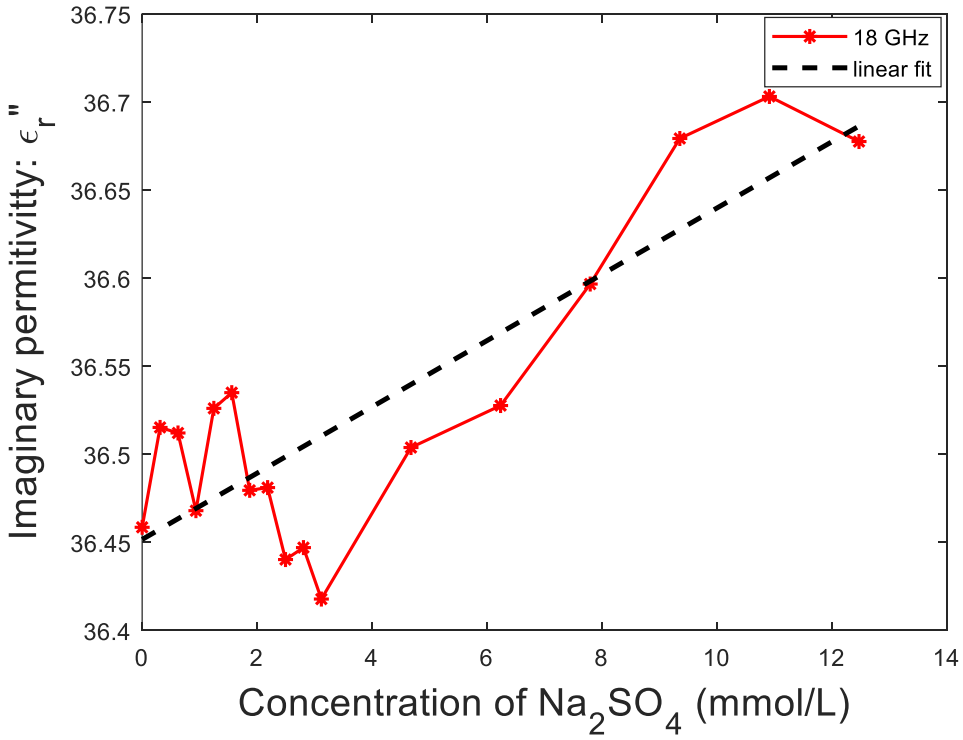

Fig 4.4 (p) Imaginary permittivity $\varepsilon_r{}''$ vs concentration of Na_2SO_4 at 18.0GHz

Table 4.2: Parameters and Norm of Residuals for Linearly Fitting Real and Imaginary Parts of Complex Permittivity with Concentration of Na_2SO_4 Solution in Water

Frequency (GHz)	Real Permittivity: ε_r'			Imaginary Permittivity: ε_r''		
	Linear fitting: $\varepsilon_r' = a'c + b'$			Linear fitting: $\varepsilon_r'' = a''c + b''$		
	Coefficient a' (L/mmol)	Coefficient b'	Norm of residuals	Coefficient a'' (L/mmol)	Coefficient b''	Norm of residuals
0.5	-0.03677	78.38	0.0322	0.8282	2.065	0.3124
1.0	-0.03664	78.17	0.0321	0.2737	5.725	0.0993
1.5	-0.03643	77.92	0.0319	0.4128	3.875	0.1533
2.0	-0.03614	77.58	0.0317	0.2038	7.566	0.0720
6.0	-0.03157	71.69	0.0309	0.0596	21.06	0.0490
10.0	-0.02602	62.79	0.0323	0.0322	29.93	0.0961
14.0	-0.02183	53.02	0.0377	0.0224	34.78	0.1462
18.0	-0.01976	44.21	0.0606	0.0188	36.45	0.1859

Assuming a linear function as in Table 4.2, the sensitivity of a change in real and imaginary parts in ionic permittivity to a change in ionic concentration, at a particular frequency, is given by the absolute values of the slope parameters a' and a''.

From these two quantities, it can be inferred that at lower frequencies, the aqueous solution shows higher sensitivity of change in complex permittivity on change in ionic concentration. It can be observed that the norm of residuals increases as one shifts to higher frequencies. The behavior for lower concentrations is no longer monotonic. This might result from higher uncertainties in the measured data for lower concentration samples at high frequencies.

Using the above information, it can be concluded that a lower frequency would yield a better sensor design. However, as mentioned before, going down in frequency is limited by the physical size requirements of the resonant sensor. Hence, an optimal resonator length of 10.35 cm is chosen for this work, which corresponds to an open-circuit fundamental resonant frequency of 1 GHz.

4.4 Design of Coupling Structure

An ideal resonator is a device which allows the formation of pure standing waves at its resonant frequency, thus prohibiting any energy to leak out of the system. In order to measure the resonance characteristics of a resonant sensor, however, it is necessary to couple some energy out of the system, into a measuring device. This can be done either noninvasively at the other end of the coaxial resonator which is not interfaced with the sample, or invasively at any point on the resonator. It is important to not couple out too much energy from the resonator. This will cause the resonator to be loaded severely, drastically affecting its resonant characteristics.

To come up with the right coupling technique for the resonant sensor, the approach developed in [44] is followed. This section summarizes the design procedure adopted for the coupling structure, whereas the following section uses parametric FEA simulations to optimize the coupling structure for the current research.

Resonator fields can be coupled to another device either capacitively or inductively. The former is done using electric field interactions, while the latter is based on the magnetic field. To couple a resonator with another device, the field distribution of the coupling structure at the resonator interface has to be oriented along the resonator field distribution. This follows that an SMA receptacle with a straight, protruding inner conductor can be used for capacitive coupling, whereas a looped inner conductor of an SMA receptacle works well for inductive coupling. Such SMA connectors are depicted in Figure 4.5.

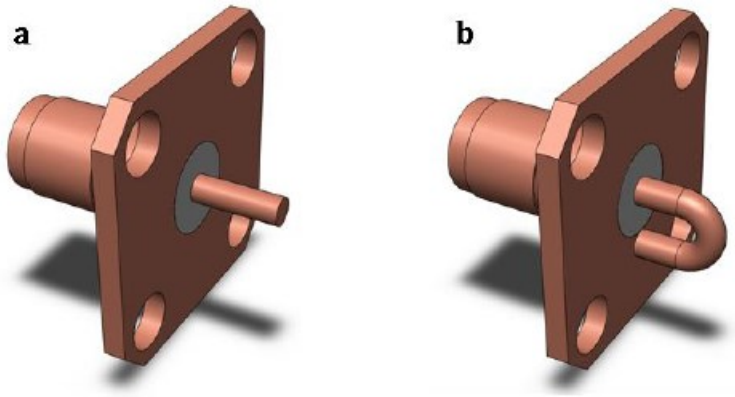

Figure 4.5. SMA receptacles for capacitive coupling (a) and inductive coupling (b) respectively (taken from [44])

It has been established in [44] that inductive coupling is not well suited for coupling into an open-ended coaxial resonator, as the loop of the connector to be used for coupling has to fit between the inner and outer conductors of the coaxial transmission line for the coupling field to be oriented according to the resonator magnetic field. Also, inductive coupling loops tend to resonate themselves, thus affecting the resonant characteristics of the resonator. These reasons make capacitive coupling a better alternative for interrogating a half-wavelength coaxial transmission line resonator.

A capacitive coupling structure can be designed to either measure the reflection coefficient looking into the resonator, or to take transmission measurements between two ports. The former is easier to implement as it requires only a single port. There are multiple ways of taking such measurements, and the simplest is to place a feedline alongside the resonator, with the gap between the resonator and the feedline determining the strength of coupling. An increase in coupling strength can be achieved by decreasing the gap size. This enables more power to be coupled from the resonator, making the act of taking measurements easier, but loads the resonator considerably to change its resonance characteristics, most importantly decreasing its

dynamic range, which can be defined as the difference between the peak power coupled from the resonator to the noise floor. Hence, weak coupling is desirable for taking resonance measurements. For a reflection based method, however, it is not possible to reliably measure a weakly coupled resonance as a large insertion loss leads to a value of reflection coefficient near 0 dB [11]. It is, in fact, considered to be bad measurement practice to try and measure a resonance that is weakly coupled, using reflection methods [97]. This calls for the need of a transmission method, which complicates the coupling structure by necessitating the use of two ports, but allows a reliable, low-uncertainty way of measuring resonance characteristics of an open-ended coaxial line resonator. The conventional approaches of getting transmission measurements involve perturbing the sample invasively into the resonator. Such structures have high uncertainties because of fabrication tolerances. Invasive coupling approaches require high volumes of sample, and also suffer from reproducibility issues if the part for filling the sample has to be disassembled for any reason. This motivated the authors of [44,92,105] to develop a noninvasive coupling approach to take transmission measurements.

The coupling structure designed by the authors of [44,92,105] enables single ended transmission coupling, leaving the other end of the resonator free for perturbation by a liquid sample. The coupling structure is designed to confine electromagnetic fields within it to avoid external interference. Two SMA receptacles are symmetrically housed on either side within a hole whose diameter is set to match the input impedance of both the ports to the 50 Ω standard. A ground plane is placed in between the two SMA receptacles to avoid crosstalk, which would potentially decrease the dynamic range. Figures 4.6 illustrates different aspects of the noninvasive coupling structure for transmission measurements, whereas Figure 4.7 demonstrates the dimensions of the coupling structure which dominate coupling strength. These figures have

been taken from [44] and the reader is recommended to refer to the article for a more rigorous discussion on the coupling structure.

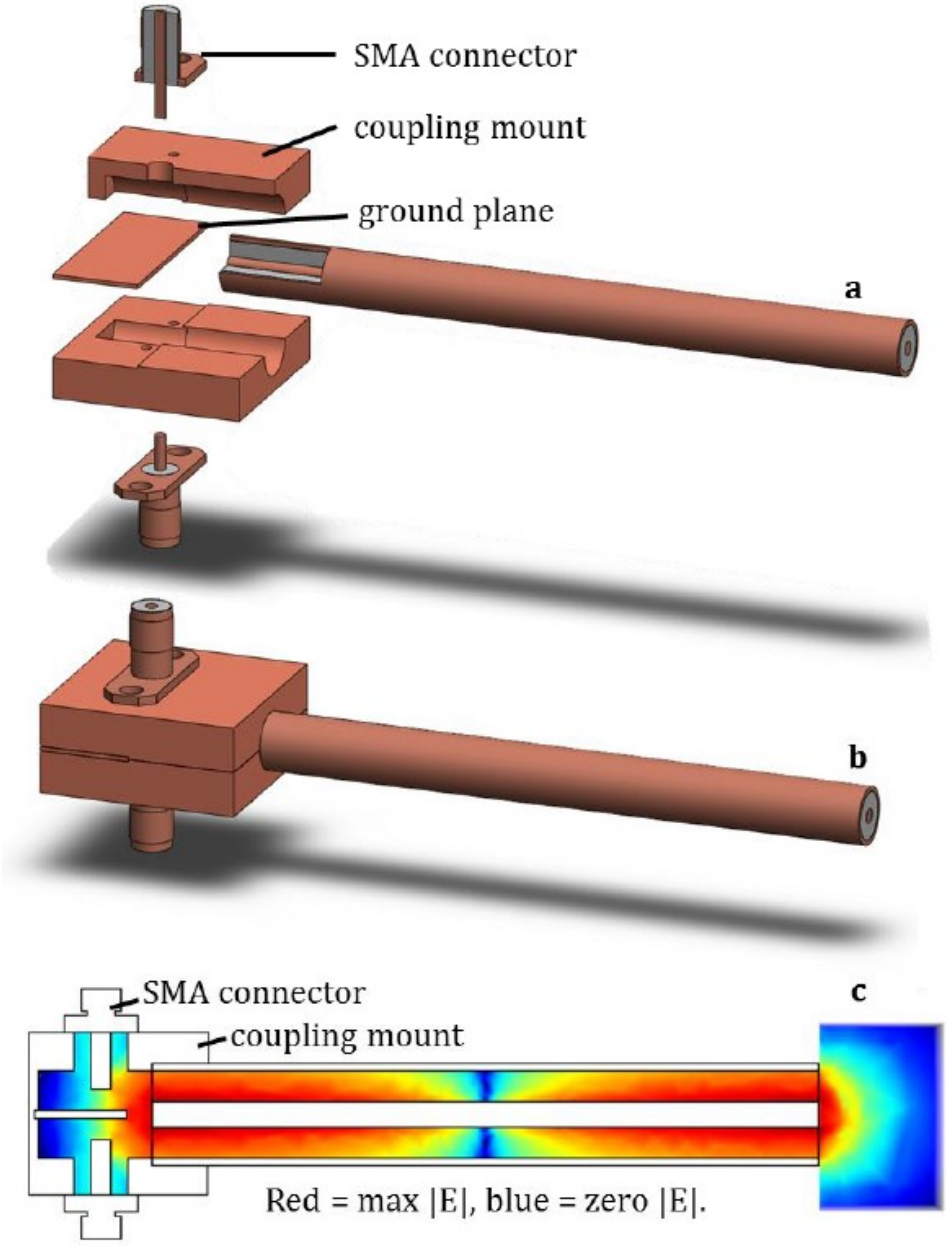

Figure 4.6. (a) Exploded view of the noninvasive coupling structure for transmission measurements on the coaxial resonant probe, (b) assembled view of the same, (c) cross sectional view of the entire sensor arrangement with a logarithmic color map illustrating the electric field inside the coupling mount, the resonator, and the liquid sample (taken from [44])

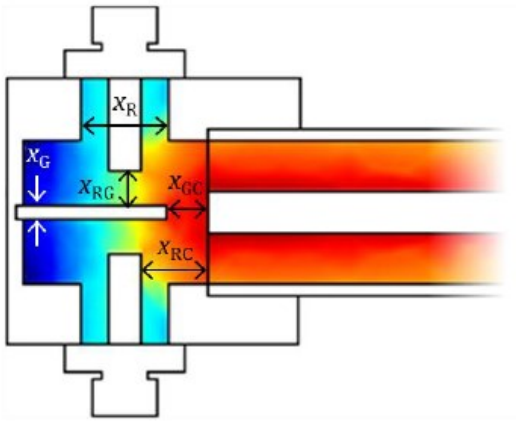

Figure 4.7 Coupling structure dimensions which dominate coupling strength (taken from [44])

The most important dimensions which dictate the coupling of fields from the resonator, as reported by the authors of [44,92,105] and demonstrated in Figure 4.7 are the following:

X_{RC}: distance between SMA receptacle and resonator

X_{GC}: distance between ground plane and resonator

X_{RG}: distance between SMA receptacle and ground plane

X_G: thickness of ground plane

X_R: radius of hole housing the SMA receptacle

Of these dimensions, X_R is set by the dimension of the protruding inner conductor of the SMA, such that the hole in the coupling structure housing the SMA receptacle forms a 50 Ω transmission line, ensuring an impedance match with the 50 Ω SMA connector itself. This means that for a standard SMA connector with an inner diameter of 1.28 mm, X_R has to be 3 mm. The authors use COMSOL simulations to find the optimum values for the other dimensions, which turn out to be $X_{RC} = 2.86$ mm, $X_{GC} = 0.25$ mm, $X_{RG} = 1.25$ mm, and $X_G = 0.5$ mm.

To test how this design performs for the problem herein, the coupling structure with the above dimensions is modeled in ANSYS HFSS and simulated for two different samples – air,

and deionized (DI) water. The simulations sweep a frequency range of 0.3 GHz to 3.3 GHz. It is expected for resonances to be seen at 1 GHz, 2 GHz and 3 GHz in air, and the resonance peaks to shift down as permittivity is increased considerably in the case of DI water. Figure 4.8 shows the sensor model designed on HFSS, and Figures 4.9-4.10 show the results of these simulations. The details of the sensor modeling and simulation on HFSS is presented in Chapter 5.

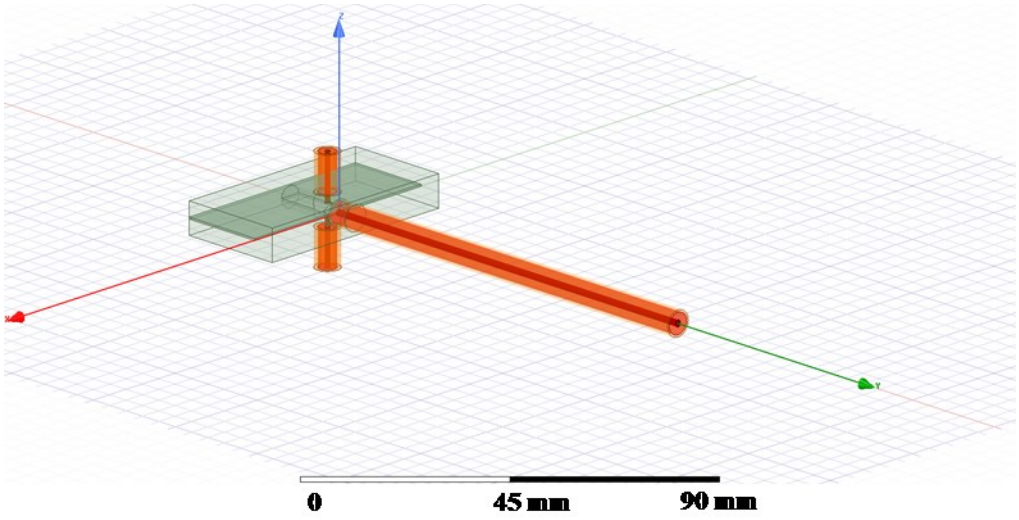

Figure 4.8 Dimetric view of resonator with coupling structure and SMA receptacles in HFSS

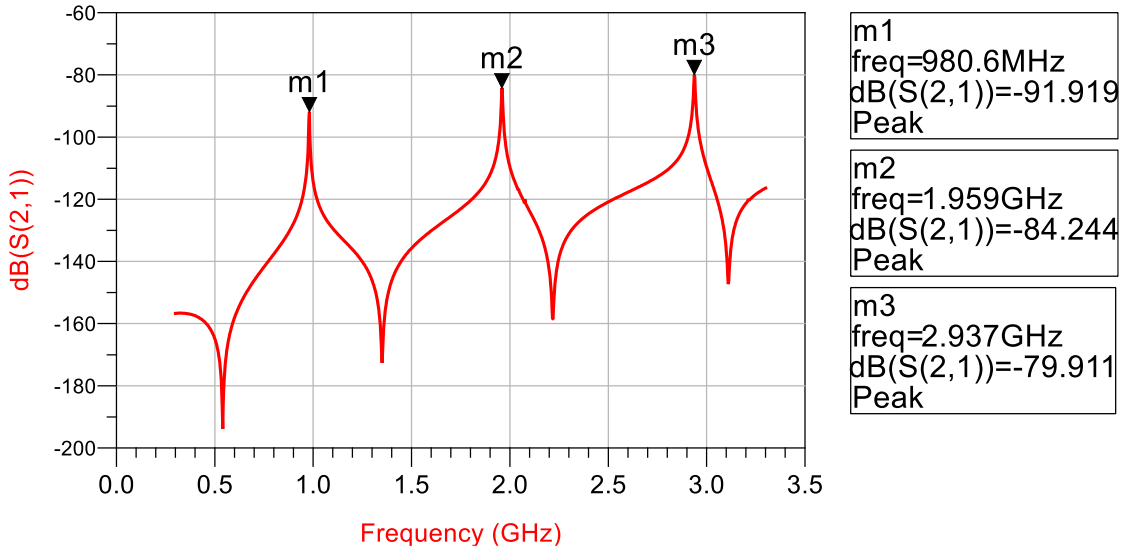

Figure 4.9 Resonance characteristics of resonant sensor in air

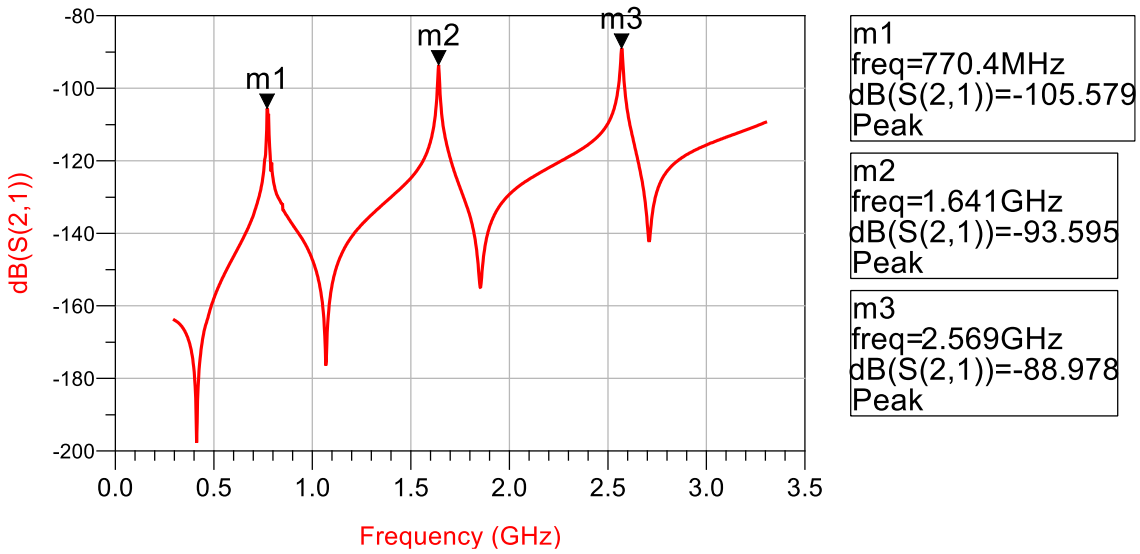

Figure 4.10 Resonance characteristics of resonant sensor in deionized water

It can be observed from Figure 4.9 that in the case of air, the resonator resonates at frequencies close to 1 GHz and its integer multiples. There is a shift from the ideal values due to the effect of coupling. Also, as expected, the resonance peaks shift down in frequency on changing the sample to deionized water. The magnitude of S_{21} however, is really low and one can expect it to go down further while testing with ionic solutions, which introduce a fair amount of loss. This calls for the need to optimize the dimensions of the coupling structure to get better coupling, and hence more easily measurable resonances. This is done through a series of parametric analyses which are detailed in the next section.

4.5 Choice of Coupling Structure Dimensions

To find the optimal coupling structure dimensions for the current research, a series of parametric sweeps are done on HFSS with deionized water sample. X_G is kept at 0.5 mm because the requirement of the ground plane is just to prevent crosstalk between the two SMA receptacles, and a smaller thickness would be practically challenging to machine out. The other dimensions which dominate coupling strength are swept and the results are shown in Figure 4.11.

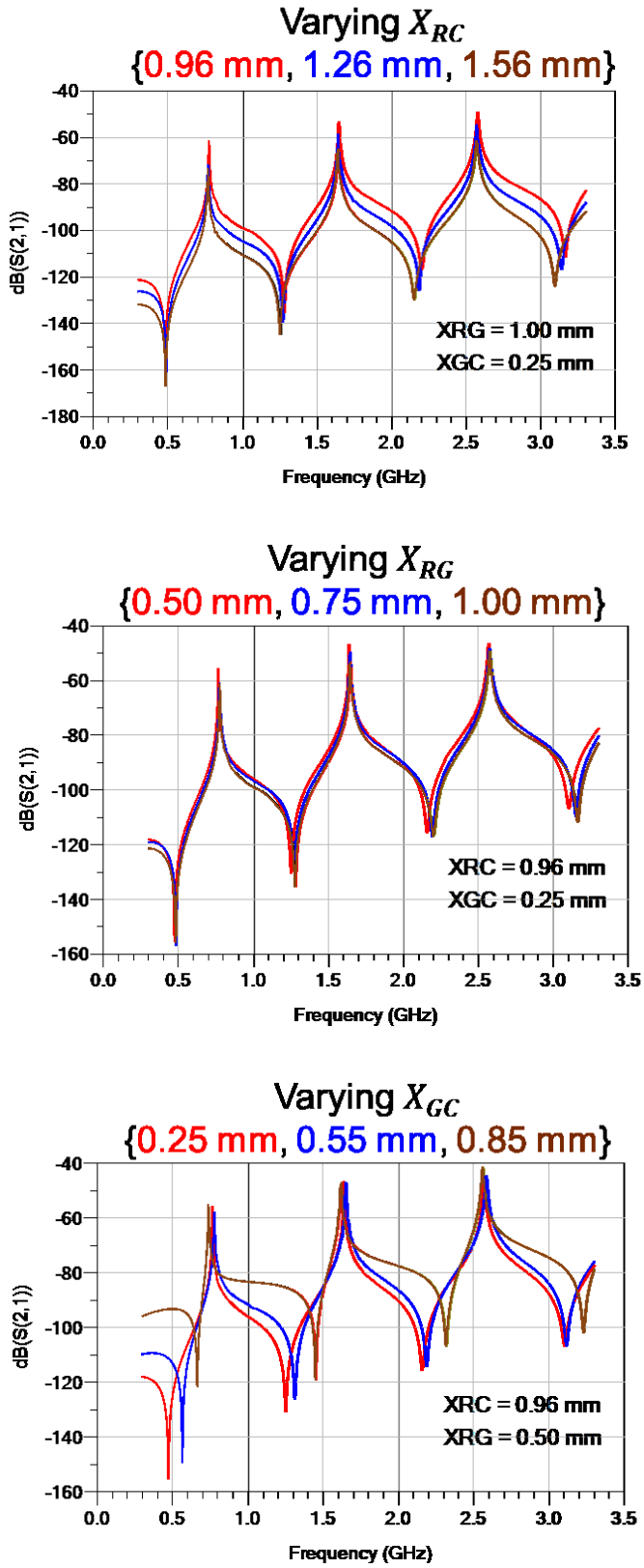

Figure 4.11 Parametric analyses of resonant sensor sweeping X_{RC}, X_{RG}, and X_{GC} respectively

From Figure 4.11, it can be seen that for X_{RC} and X_{GC}, decreasing their size leads to more coupling, and hence a higher peak power. The minimum values of X_{RC} and X_{GC} are chosen such that the machining cost of the sensor does not increase drastically. In the plot showing the sweep of X_{GC}, it can be seen that the resonance peak is the highest for $X_{GC} = 0.85\ mm$. For this value, however, the resonance as is not symmetric, and this might lead to uncertainties in measuring the resonance. Hence, $X_{GC} = 0.25$ mm is chosen for the design, which shows a drop in S_{21} by only 0.6 dB.

The final chosen dimensions of the critical parameters have been tabulated in Table 4.3. For these values, the resonant sensor shows a fundamental resonant frequency of $765.8\ MHz$, when the sample is deionized (DI) water. It can be observed that for the fundamental mode of resonance, the current dimensions of the coupling structure help provide an S_{21} response greater in magnitude by 50 dB than with the dimensions mentioned in [44,92,105]. The next chapter explores how the resonant frequency of the resonant sensor designed over the last two chapters changes as it simulated using samples of different ionic solutions with varying concentrations.

Table 4.3: Final optimized resonator coupling structure dimensions which dominate coupling strength

$\mathbf{X_{RC}}$	$\mathbf{X_{GC}}$	$\mathbf{X_{RG}}$	$\mathbf{X_{G}}$
0.96 mm	0.25 mm	0.50 mm	0.50 mm

CHAPTER 5. MODELING AND SIMULATIONS

This chapter discusses the resonant sensor model created on ANSYS HFSS 17.0, the simulation setup used, and the subsequent results obtained by simulating the model for different solution sample data. It is divided, hence, in two sections – Section 5.1 detailing out the simulation model and the solution setup, whereas Section 5.2 deals with simulation results using sample data.

5.1 Resonant Sensor Modeling on ANSYS HFSS

The resonant sensor is modeled in four parts, which are – (1) coaxial transmission line resonator, (2) coupling structure consisting of two coupling mounts and a ground plane, (3) two 50 Ω SMA connectors, and (4) sample solution at the open end of the resonator. These have been discussed as follows.

Coaxial Transmission Line

As mentioned in chapter 4, the objective of making the sensor low-cost suggests the use of a readily available coaxial transmission line. RG 401 is a standard 50 Ω coaxial transmission line with copper conductors (conductivity $\sigma_{copper} = 5.8 \times 10^7$ S/m), and a PTFE dielectric (relative permittivity $\varepsilon_{m,PTFE}{}' = 2.1$). The model for the resonator is created using the radial dimensions from the datasheet available on [122], and the materials have been taken from the predefined materials library of HFSS. A length of 10.35 cm is chosen for the resonator, which corresponds to a fundamental resonant frequency of 1 GHz in free space.

Coupling Structure

The coupling structure is modeled using copper conductors. It has two identical top and bottom coupling mounts, with a thin layer of ground plane sandwiched in between to prevent

crosstalk. The dimensions which dominate coupling strength are presented in Table 4.2. The external dimensions are illustrated in Figure. 5.1. The length L and the width W are chosen such that they could be easily machined using readily available tools, as the two dimensions correspond to 1" and 2" respectively. The critical dimensions X_{RC} and X_{GC} also have an impact on L. The height H is determined by the dimensions of the SMA connector, the optimum value of X_{RG} and X_G.

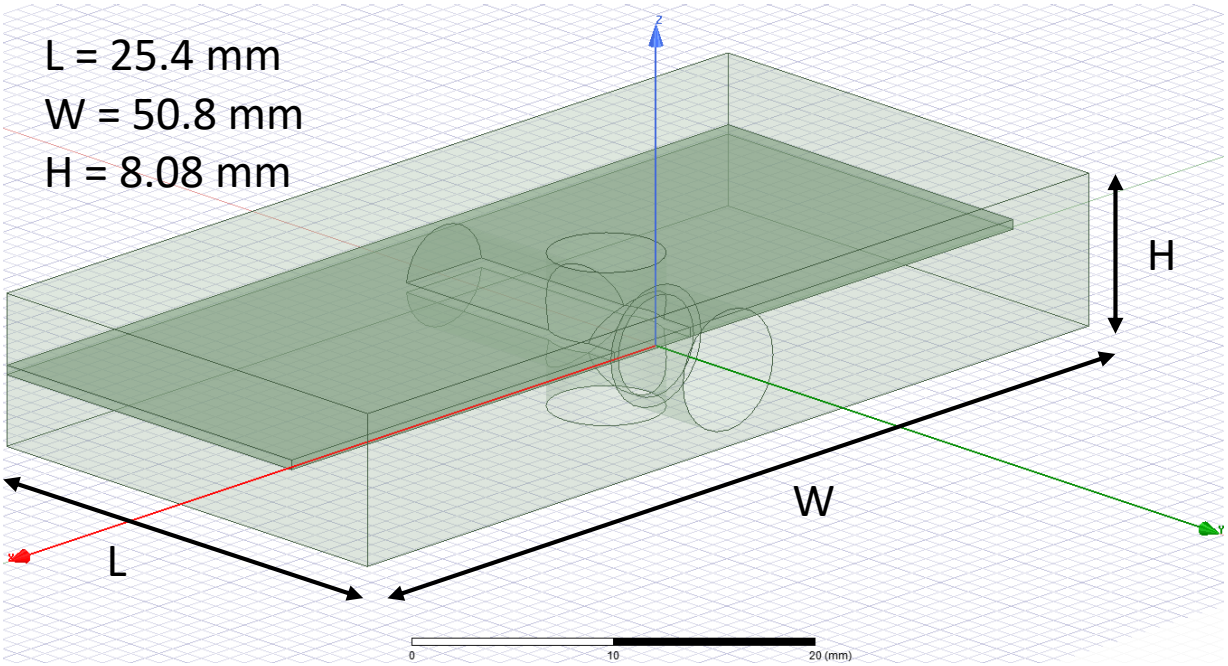

Figure 5.1 External dimensions of coupling structure containing the ground plane

SMA Connectors

The two SMA receptacles are modeled following the datasheet of a standard 50 Ω SMA connector [123]. The SMA connector has copper conductors, with a protruding inner conductor, and a PTFE dielectric. The coupling structure along with the SMA receptacles are shown in Figure 5.2. The circular hole at the right face of the coupling structure is provided for the coaxial

resonator to fit in. With the coaxial resonator partially sitting inside the hole of the coupling structure, the total length of the system adds up to 12.38 cm (less than 5”).

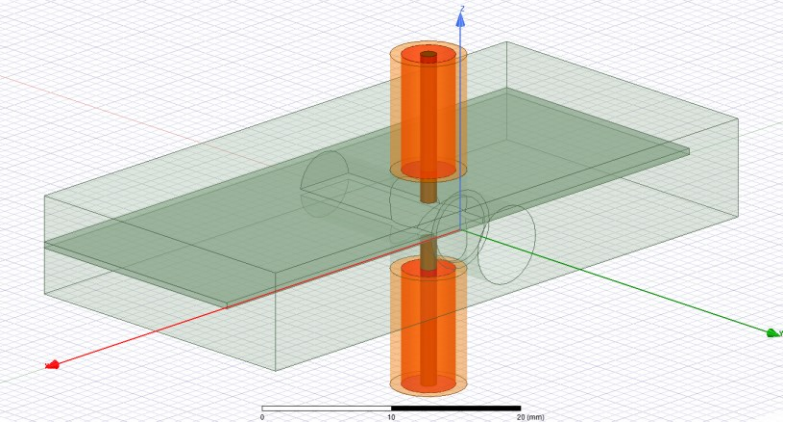

Figure 5.2 Coupling structure with SMA receptacles

Sample Solutions

The sample is modeled as a box around the coaxial resonator, whose dielectric constant and loss tangent are changed during each simulation to represent a different sample concentration or ion. The data used has been obtained from the research discussed in Chapter 2. The model is drawn to simulate the resonator being dipped to a length of 3.35 cm inside the solution under test, as shown in Figure 5.3.

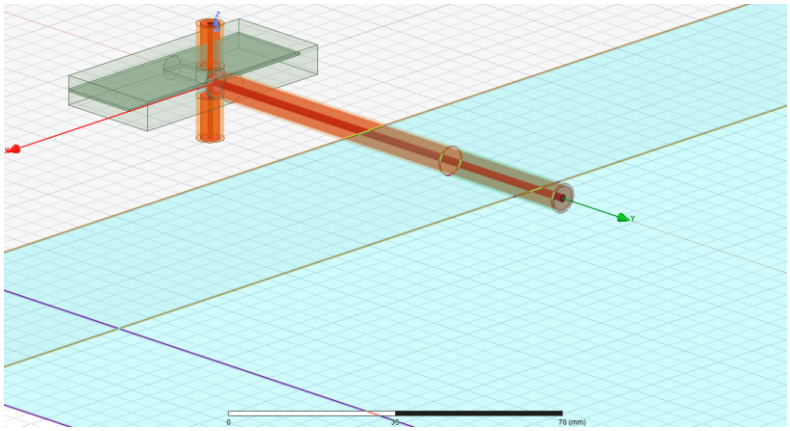

Figure 5.3 Resonant sensor dipped in sample (light blue box)

For the purpose of the simulation, appropriate boundary conditions are required at all the external faces of the model to define the solution space for the simulator. The boundary condition chosen is driven by how the sensor is expected to behave in a real-world scenario. It can be envisaged that all the fields would be contained inside the resonant sensor, except for at the sample interface from where some energy could radiate into the lossy electrolyte sample. A fitting boundary condition for this situation is to put the entire resonant sensor inside a radiation box and enforce a radiation boundary condition on the box. This imposes that all the radiated fields are absorbed at the faces of the box. A rule of thumb is to separate the radiating structure from the faces of the radiation box by at least $\lambda/4$, so that negligible energy is left to be absorbed at the boundary, leading to robust solutions [124]. For this research, the radiation box is made to be partly of air, and the rest of the varying solution sample to replicate a practical situation.

The simulations are run using automatic broadband adaptive meshing which provides high accuracy of solutions, in lieu of high computational time [125]. An interpolating frequency sweep of 12001 points between 300 MHz and 3.3 GHz is selected (step size 0.25 MHz), with the solver solving the model at least 60 points. The solution setup parameter of maximum delta S is set to the default of 0.02. Maximum delta S represents the maximum change that occurs in two consecutive passes in the magnitude of any of the calculated S-parameters. The maximum number of passes is set to 20.

The simulations are executed on an Intel® Core™ i7-2600 CPU @ 3.40GHz processor, using 8 GB RAM, and Microsoft Windows 10 Enterprise 2016 64-bit operating system. The results of these simulations are discussed in the next section.

5.2 Simulation Results

In this section, the results obtained by simulating the designed resonant sensor for different ionic solution samples are presented. The simulations are executed for test samples consisting of deionized water, and fifteen different concentrations of sodium nitrate, sodium sulfate, and sodium chloride, respectively, and the transmission S-parameter S_{21} is measured across the two SMA connectors. The concentration ranges for the different types of ions used are provide in Table 2.1. Figure 5.4 shows the S_{21} response of the resonant sensor when it is interfaced with a sample consisting of deionized water. Figure 5.5 to 5.10 demonstrate the same for two concentrations of each of the three types of ionic solutions considered in this work. It can be observed from these figures that in the swept frequency range of 300 MHz to 3.3 GHz, the resonant sensor exhibits three modes of resonance, and for each type of ionic solution, the resonant frequency decreases as the ionic concentration increases for all three resonant modes. Tables 5.1, 5.3 and 5.5 present the dielectric properties of the different concentrations of the three types of electrolyte samples used in this work, whereas, the detailed results of all the simulations for the three different types of solution samples are listed in Tables 5.2, 5.4 and 5.6.

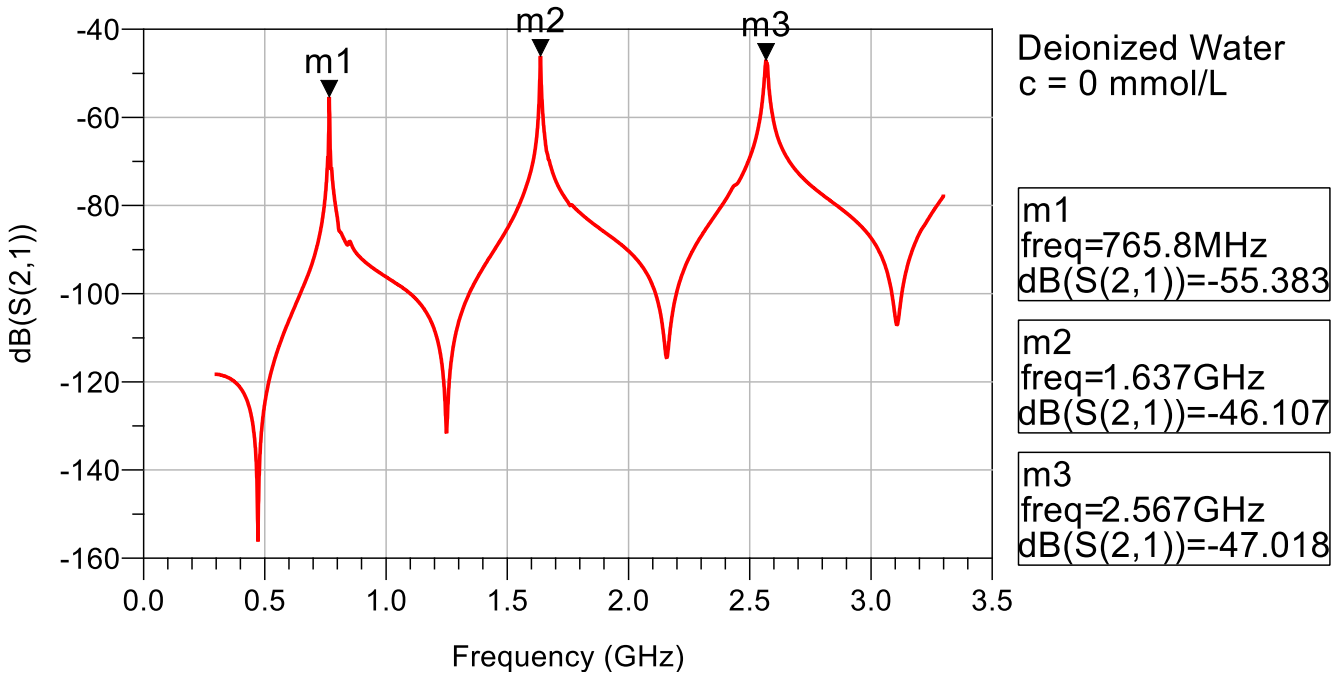

Figure 5.4 Response of resonant sensor for deionized water sample

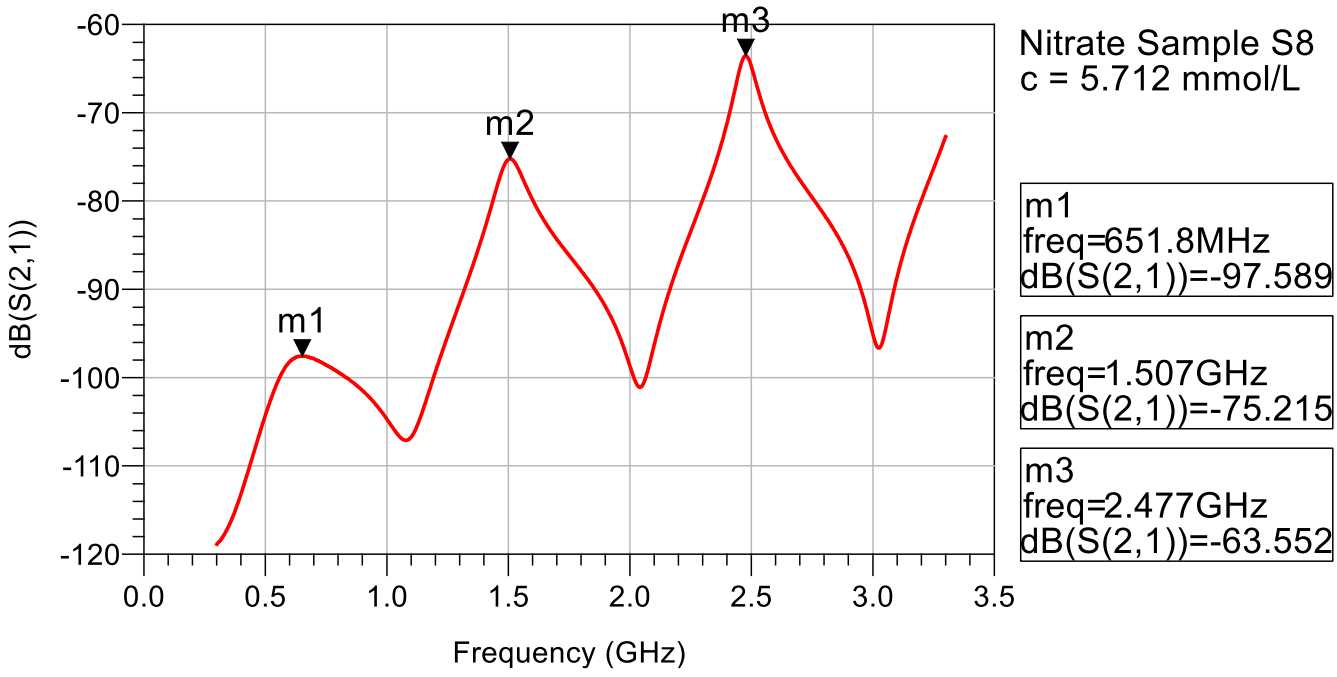

Figure 5.5 Response of resonant sensor for sodium nitrate solution with 5.712 mmol/L concentration (sample S8)

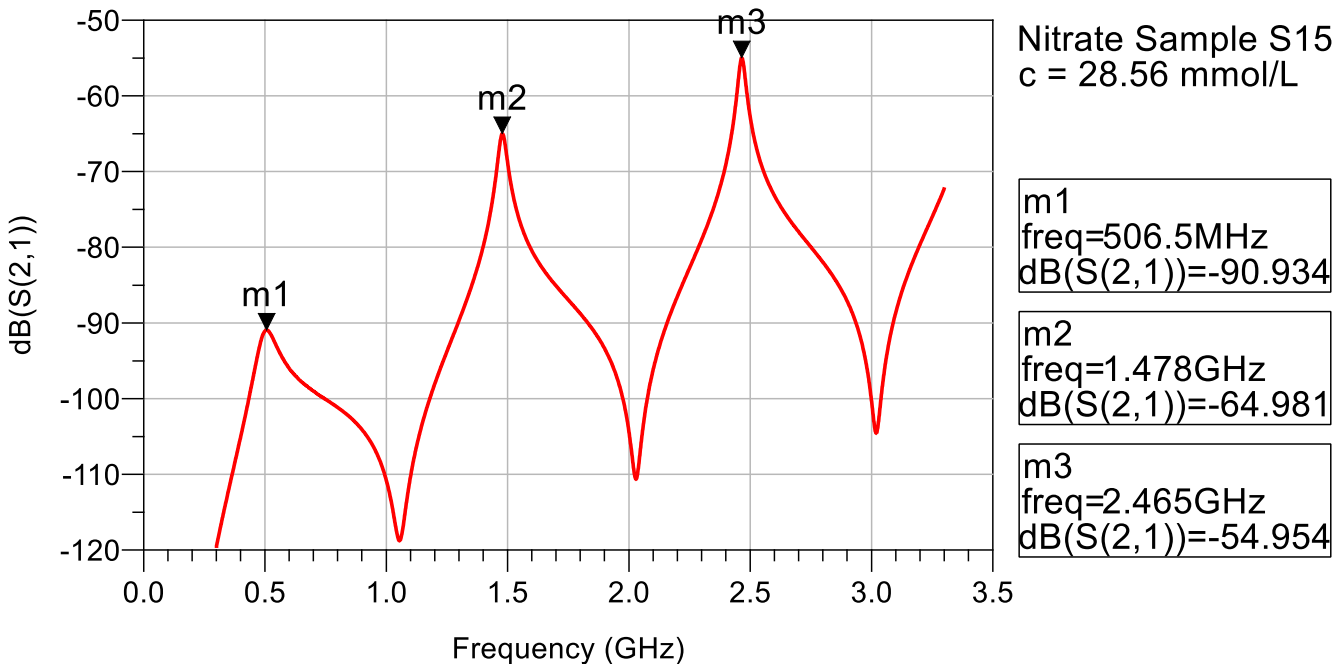

Figure 5.6 Response of resonant sensor for sodium nitrate solution with 28.56 mmol/L concentration (sample S15)

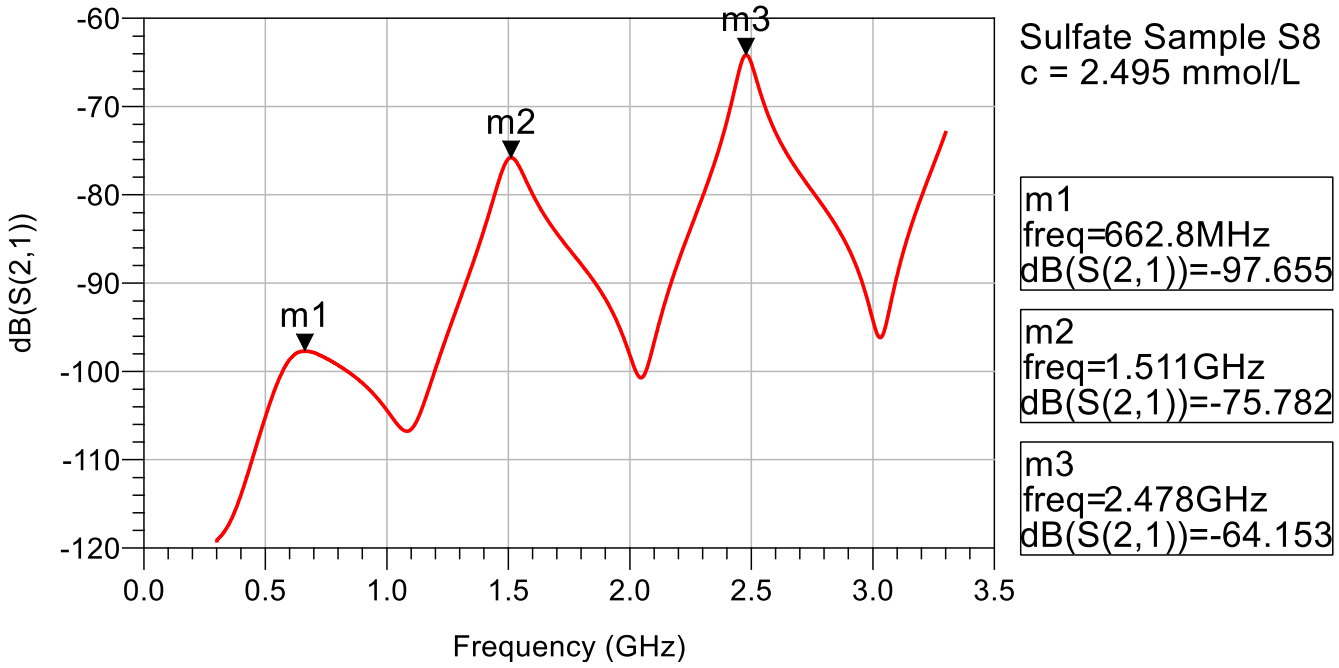

Figure 5.7 Response of resonant sensor for sodium sulfate solution with 2.495 mmol/L concentration (sample S8)

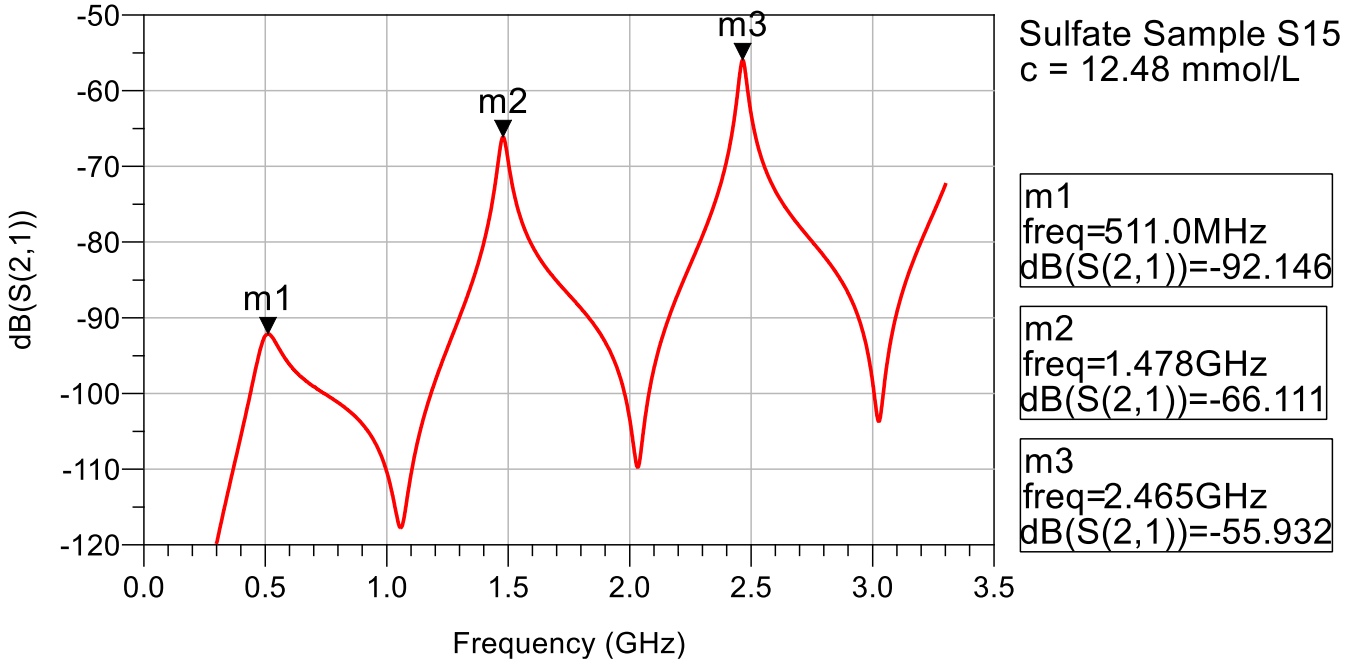

Figure 5.8 Response of resonant sensor for sodium sulfate solution with 12.48 mmol/L concentration (sample S15)

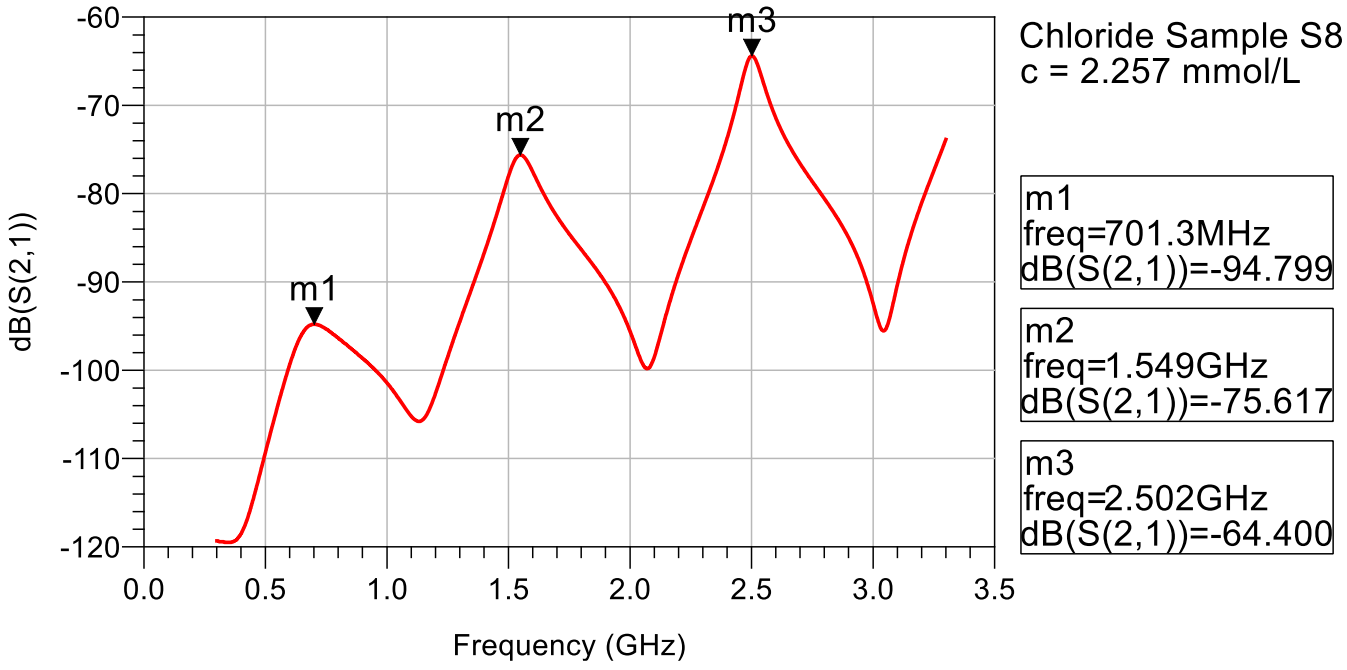

Figure 5.9 Response of resonant sensor for sodium chloride solution with 2.257 mmol/L concentration (sample S8)

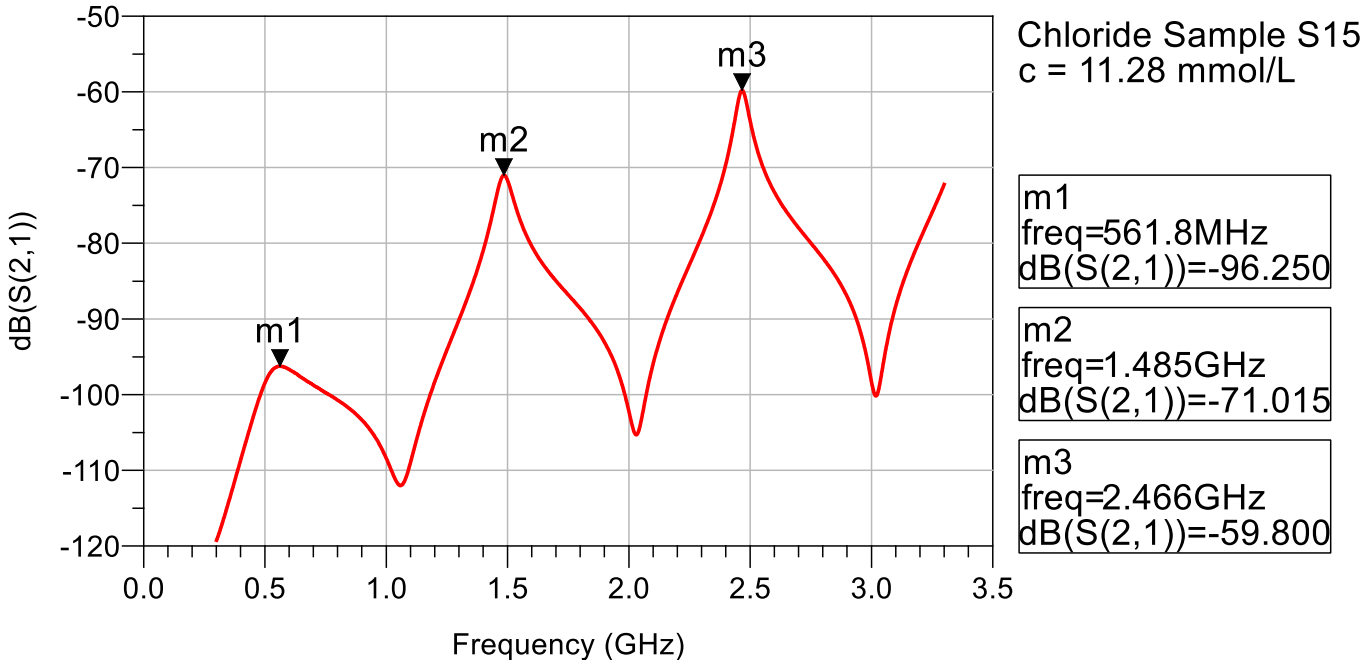

Figure 5.10 Response of resonant sensor for sodium chloride solution with 11.28 mmol/L concentration (sample S15)

Table 5.1 Dielectric properties of different concentrations of sodium nitrate solution samples at frequencies close to the first three resonant frequencies for deionized water [39]

Frequency		**770 MHz**			**1.64 GHz**			**2.57 GHz**		
Sample No.	***c* (mmol/L)**	ε_r'	ε_r''	**tan δ**	ε_r'	ε_r''	**tan δ**	ε_r'	ε_r''	**tan δ**
S0	0	78.24	2.923	0.03736	77.83	6.189	0.07952	77.08	9.598	0.1245
S1	0.7139	78.23	3.162	0.04042	77.82	6.300	0.08096	77.07	9.668	0.1255
S2	1.428	78.22	3.364	0.04301	77.81	6.394	0.08218	77.06	9.728	0.1262
S3	2.142	78.21	3.559	0.04550	77.81	6.488	0.08339	77.06	9.790	0.1270
S4	2.856	78.19	3.803	0.04864	77.78	6.606	0.08493	77.03	9.869	0.1281
S5	3.570	78.18	3.979	0.05090	77.77	6.687	0.08599	77.02	9.920	0.1288
S6	4.284	78.16	4.175	0.05342	77.75	6.776	0.08715	77.00	9.972	0.1295
S7	4.998	78.15	4.374	0.05596	77.75	6.871	0.08838	77.00	10.036	0.1303
S8	5.712	78.14	4.555	0.05829	77.74	6.956	0.08949	76.99	10.091	0.1311
S9	6.425	78.12	4.736	0.06062	77.72	7.042	0.09060	76.97	10.146	0.1318
S10	7.139	78.13	4.926	0.06304	77.73	7.135	0.09180	76.98	10.211	0.1326
S11	10.709	78.04	5.923	0.07590	77.64	7.598	0.09785	76.90	10.499	0.1365
S12	14.279	77.88	7.796	0.1001	77.48	8.455	0.1091	76.74	11.021	0.1436
S13	21.418	77.80	8.712	0.1120	77.40	8.875	0.1147	76.67	11.278	0.1471
S14	24.988	77.74	9.643	0.1240	77.34	9.307	0.1203	76.61	11.547	0.1507
S15	28.558	77.68	10.549	0.1358	77.28	9.723	0.1258	76.55	11.802	0.1542

Table 5.2 Simulation results for sodium nitrate solution samples

Sample No.	c (mmol/L)	f_0 (GHz)	Δf_0 (GHz)	Q_0	f_1 (GHz)	Δf_1 (GHz)	Q_1	f_2 (GHz)	Δf_2 (GHz)	Q_2
S0	0	0.7658	0	382.9	1.637	0	282.2	2.567	0	183.4
S1	0.7139	0.7418	-0.0240	7.546	1.606	-0.0304	19.59	2.543	-0.0245	38.52
S2	1.428	0.7335	-0.0323	4.265	1.585	-0.0522	13.01	2.525	-0.0425	27.96
S3	2.142	0.7270	-0.0388	3.004	1.566	-0.0709	11.16	2.511	-0.0563	25.06
S4	2.856	0.7198	-0.0460	2.502	1.548	-0.0885	10.20	2.500	-0.0675	24.46
S5	3.570	0.7047	-0.0611	2.332	1.535	-0.1019	10.65	2.492	-0.0755	25.35
S6	4.284	0.6840	-0.0818	2.219	1.522	-0.1150	11.36	2.485	-0.0825	27.61
S7	4.998	0.6665	-0.0993	2.136	1.513	-0.1237	12.18	2.480	-0.0872	24.26
S8	5.712	0.6518	-0.1140	2.101	1.507	-0.1297	12.79	2.477	-0.0902	31.79
S9	6.425	0.6375	-0.1283	2.068	1.502	-0.1347	13.68	2.474	-0.0927	32.69
S10	7.139	0.6235	-0.1423	2.121	1.498	-0.1387	14.69	2.472	-0.0948	34.48
S11	10.709	0.5683	-0.1975	2.310	1.486	-0.1504	20.17	2.467	-0.0998	47.17
S12	14.279	0.5353	-0.2305	2.946	1.481	-0.1554	27.33	2.466	-0.1015	58.56
S13	21.418	0.5182	-0.2476	4.048	1.479	-0.1574	33.62	2.465	-0.1022	64.69
S14	24.988	0.5175	-0.2483	4.037	1.479	-0.1574	33.62	2.465	-0.1022	72.49
S15	28.558	0.5065	-0.2593	5.743	1.478	-0.1584	43.23	2.465	-0.1017	82.18

Table 5.3 Dielectric properties of different concentrations of sodium sulfate solution samples at frequencies close to the first three resonant frequencies for deionized water [39]

Frequency		770 MHz			1.64 GHz			2.57 GHz		
Sample No.	c (mmol/L)	ε_r'	ε_r''	$\tan\delta$	ε_r'	ε_r''	$\tan\delta$	ε_r'	ε_r''	$\tan\delta$
S0	0	78.24	2.923	0.03736	77.83	6.189	0.07952	77.08	9.598	0.1245
S1	0.3119	78.24	3.133	0.04004	77.83	6.292	0.08085	77.07	9.669	0.1255
S2	0.6237	78.23	3.343	0.04273	77.82	6.391	0.08212	77.07	9.732	0.1263
S3	0.9356	78.21	3.523	0.04505	77.8	6.471	0.08318	77.04	9.778	0.1269
S4	1.247	78.21	3.706	0.04738	77.8	6.559	0.08431	77.05	9.837	0.1277
S5	1.559	78.21	3.878	0.04958	77.8	6.641	0.08537	77.04	9.891	0.1284
S6	1.871	78.18	4.048	0.05178	77.76	6.713	0.08633	77.01	9.927	0.1289
S7	2.183	78.17	4.236	0.05419	77.76	6.802	0.08748	77	9.985	0.1297
S8	2.495	78.16	4.405	0.05636	77.75	6.878	0.08847	76.99	10.03	0.1303
S9	2.807	78.14	4.581	0.05863	77.73	6.96	0.08954	76.98	10.08	0.1309
S10	4.678	78.07	5.6	0.07173	77.66	7.437	0.09576	76.91	10.38	0.135
S11	6.237	78.03	6.425	0.08233	77.62	7.822	0.1008	76.87	10.63	0.1382
S12	7.797	77.96	7.233	0.09278	77.55	8.196	0.1057	76.8	10.86	0.1414
S13	9.356	77.9	8.017	0.1029	77.49	8.564	0.1105	76.74	11.09	0.1446
S14	10.92	77.85	8.801	0.1131	77.44	8.931	0.1153	76.69	11.33	0.1477
S15	12.48	77.8	9.746	0.1253	77.39	9.366	0.121	76.64	11.59	0.1513

Table 5.4 Simulation results for sodium sulfate solution samples

Sample No.	c (mmol/L)	f_0 (GHz)	Δf_0 (GHz)	Q_0	f_1 (GHz)	Δf_1 (GHz)	Q_1	f_2 (GHz)	Δf_2 (GHz)	Q_2
S0	0	0.7658	0	382.9	1.637	0	282.2	2.567	0	183.4
S1	0.3119	0.7418	-0.0240	8.626	1.608	-0.0287	21.79	2.544	-0.0228	42.40
S2	0.6237	0.7340	-0.0318	4.310	1.587	-0.0499	13.47	2.527	-0.0405	28.13
S3	0.9356	0.7288	-0.0370	3.141	1.569	-0.0674	11.37	2.513	-0.0537	25.13
S4	1.247	0.7208	-0.0450	2.650	1.554	-0.0829	10.62	2.503	-0.0643	24.54
S5	1.559	0.7093	-0.0565	2.413	1.540	-0.0967	10.56	2.494	-0.0727	24.94
S6	1.871	0.6945	-0.0713	2.226	1.528	-0.1087	10.90	2.488	-0.0795	26.41
S7	2.183	0.6777	-0.0881	2.172	1.518	-0.1187	11.68	2.482	-0.0850	27.58
S8	2.495	0.6627	-0.1031	1.863	1.511	-0.1257	12.21	2.478	-0.0887	28.82
S9	2.807	0.6482	-0.1176	2.001	1.505	-0.1314	5.588	2.476	-0.0915	31.06
S10	4.678	0.5840	-0.1818	2.147	1.488	-0.1487	7.282	2.468	-0.0990	42.41
S11	6.237	0.5540	-0.2118	2.493	1.484	-0.1530	8.629	2.466	-0.1007	49.52
S12	7.797	0.5360	-0.2298	2.983	1.481	-0.1554	9.889	2.420	-0.1470	55.25
S13	9.356	0.5250	-0.2408	3.547	1.480	-0.1567	10.96	2.465	-0.1017	62.10
S14	10.92	0.5172	-0.2486	4.111	1.479	-0.1577	11.84	2.465	-0.1020	68.47
S15	12.48	0.5110	-0.2548	4.904	1.479	-0.1582	13.38	2.465	-0.0812	77.03

Table 5.5 Dielectric properties of different concentrations of sodium chloride solution samples at frequencies close to the first three resonant frequencies for deionized water [39]

Frequency		770 MHz			1.64 GHz			2.57 GHz		
Sample No.	c (mmol/L)	ε_r'	ε_r''	$\tan\delta$	ε_r'	ε_r''	$\tan\delta$	ε_r'	ε_r''	$\tan\delta$
S0	0	78.24	2.923	0.03736	77.83	6.189	0.07952	77.08	9.598	0.1245
S1	0.2821	78.27	3.010	0.03846	77.86	6.237	0.08011	77.11	9.637	0.1250
S2	0.5641	78.29	3.116	0.03980	77.88	6.299	0.08087	77.13	9.690	0.1256
S3	0.8462	78.31	3.202	0.04089	77.90	6.348	0.08148	77.15	9.734	0.1262
S4	1.128	78.34	3.276	0.04182	77.93	6.392	0.08202	77.18	9.773	0.1266
S5	1.410	78.32	3.365	0.04296	77.91	6.439	0.08265	77.16	9.810	0.1271
S6	1.692	78.31	3.461	0.04420	77.90	6.483	0.08322	77.15	9.837	0.1275
S7	1.974	78.28	3.529	0.04508	77.88	6.512	0.08362	77.13	9.852	0.1277
S8	2.257	78.27	3.631	0.04639	77.86	6.558	0.08423	77.11	9.880	0.1281
S9	2.539	78.26	3.766	0.04718	77.85	6.623	0.08462	77.11	9.924	0.1284
S10	4.231	78.24	4.175	0.05335	77.84	6.817	0.08758	77.10	10.05	0.1304
S11	5.641	78.23	4.596	0.05875	77.83	7.019	0.09019	77.09	10.18	0.1321
S12	7.052	78.20	5.010	0.06407	77.80	7.222	0.09282	77.06	10.32	0.1340
S13	8.462	78.19	5.345	0.06836	77.79	7.383	0.09490	77.05	10.43	0.1354
S14	9.872	78.17	5.746	0.07350	77.77	7.570	0.09733	77.04	10.55	0.1370
S15	11.28	78.12	6.141	0.07861	77.72	7.751	0.09973	76.98	10.66	0.1385

Table 5.6 Simulation results for sodium chloride solution samples

Sample No.	c (mmol/L)	f_0 (GHz)	Δf_0 (GHz)	Q_0	f_1 (GHz)	Δf_1 (GHz)	Q_1	f_2 (GHz)	Δf_2 (GHz)	Q_2
S0	0	0.7658	0	382.9	1.637	0	282.2	2.567	0	183
S1	0.2821	0.7578	-0.0080	20.05	1.629	-0.0077	43.10	2.561	-0.0058	71.14
S2	0.5641	0.7415	-0.0243	9.980	1.609	-0.0274	24.38	2.546	-0.0215	46.96
S3	0.8462	0.7418	-0.0240	6.869	1.605	-0.032	11.30	2.541	-0.0258	25.93
S4	1.128	0.7308	-0.0350	5.442	1.591	-0.0457	15.91	2.541	-0.0258	30.91
S5	1.410	0.7338	-0.0320	4.314	1.591	-0.0457	13.45	2.541	-0.0258	19.21
S6	1.692	0.7315	-0.0343	3.549	1.578	-0.0592	12.11	2.519	-0.0477	26.24
S7	1.974	0.7292	-0.0366	3.198	1.571	-0.0659	11.40	2.514	-0.0527	25.66
S8	2.257	0.7013	-0.0645	2.874	1.549	-0.0879	7.75	2.502	-0.0655	28.36
S9	2.539	0.7238	-0.0420	2.585	1.553	-0.0834	10.35	2.503	-0.0645	23.99
S10	4.231	0.6867	-0.0791	2.217	1.523	-0.1134	11.14	2.486	-0.0815	27.02
S11	5.641	0.6505	-0.1153	2.086	1.507	-0.1302	12.99	2.476	-0.0908	31.66
S12	7.052	0.6198	-0.1460	2.066	1.497	-0.1397	14.97	2.472	-0.0952	36.24
S13	8.462	0.596	-0.1698	2.127	1.492	-0.1447	16.99	2.470	-0.097	41.17
S14	9.872	0.5827	-0.1831	2.158	1.489	-0.1477	18.57	2.469	-0.0982	43.85
S15	11.28	0.5617	-0.2041	2.380	1.485	-0.1517	21.21	2.467	-0.1005	47.43

From the Tables 5.1, 5.3, and 5.5, it can be observed that for each type of sample solution, as ionic concentration (c) is increased, the real part of relative permittivity (ε_r') decreases, whereas the imaginary part of relative permittivity (ε_r'') and loss tangent ($\tan\delta = \varepsilon_r'' / \varepsilon_r'$) increase. The values of ε_r', ε_r'', and $\tan\delta$ have been presented at three different frequencies for all concentrations of the different electrolyte samples. These three frequencies represent the closest frequencies available in the experimental dataset which correspond to the resonant frequencies of the first three modes for deionized water (Figure 5.4).

Figures 5.4 to 5.10, as well as, Tables 5.2, 5.4, and 5.7 demonstrate that the increases in concentration also lead to a decrease in resonant frequency for all three kinds of ionic species for all three resonant modes observed. Hence, this fact can be used to measure a shift in resonant frequency for a sample containing a particular kind of ion from the corresponding resonant frequency for deionized water, and subsequently calculate the ionic concentration of the sample

under test from it. The approximate values of the quality factors (Q) for the first three resonant modes are also reported in Tables 5.2, 5.4, and 5.7 for the three respective ionic species. These have been calculated from the spectrum of S_{21} using the standard formula for r-th mode of resonance [51]:

$$Q_r = \frac{f_r}{\Delta f_{3db_r}} = \frac{f_r}{f_{3dB+_r} - f_{3dB-_r}} \tag{5.1}$$

In Equation (5.1), Δf_{3dB_r} represents the 3 dB bandwidth or the full width half maximum (FWHM) of the r-th mode of resonance. It is calculated by taking the difference of the two frequencies (f_{3dB+_r} and f_{3dB-_r}) where the magnitude of S_{21} falls by 3 dB from the peak value at f_r. Due to the finite number of frequency points used for simulation, the calculated value of Δf_{3dB_r} is approximate, leading to approximate values of Q_r. Therefore, no conclusions have been drawn from the calculated values of the quality-factor apart from noticing that for each of the three types of sample solutions, the quality factor is in the same order of magnitude for a particular resonant mode, and the values decrease significantly from the deionized water sample as the ions introduce significant amount of loss into the resonant system. The variation of Q with the change in ionic concentration can be a topic of interest for future research on the open-ended coaxial resonant sensor.

To gain further insight into the operation of the sensor, it is of interest to understand how the two different parts of the permittivity affect the resonant characteristics. Since the dielectric properties of a sample are input to the simulator in the form of the real part of relative permittivity (ε_r') and loss tangent ($\tan\delta$), two artificial samples are created by swapping the ε_r' of nitrate sample S8 (c = 5.712 mmol/L) with the ε_r' of nitrate sample S15 (c = 28.56 mmol/L)

keeping $\tan\delta$ constant, and the $\tan\delta$ of nitrate sample S8 with the $\tan\delta$ of nitrate sample S15 keeping ε_r' constant. The simulation results are tabulated in Table 5.7.

Table 5.7 Resonant frequencies in GHz of different modes for nitrate sample S8 with a concentration of 5.712 mmol/L, artificially created sample using real permittivity of S8 and loss tangent of S15, sample S15 with a concentration of 28.56 mmol/L, and artificially created sample using real permittivity of S15 and loss tangent of S8

ε_r'	$\tan\delta$	f_0 (GHz)	f_1 (GHz)	f_2 (GHz)
S8	S8	0.6518	1.507	2.477
S8	S15	0.5102	1.479	2.465
S15	S15	0.5065	1.478	2.465
S15	S8	0.6458	1.606	2.477

From the experimental data it can be seen that as the ionic concentration of a solution increases, the real permittivity decreases, whereas the loss tangent increases [39]. Table 5.7 suggests that when only the real permittivity of a sample is changed, keeping loss tangent constant, the change in resonant frequency is much smaller than when only the loss tangent is changed, and real permittivity is kept constant. Thus, it can be said that for the sample concentrations used in this research, $\tan\delta$ dominates the change in resonant frequency.

Having obtained the resonant frequencies for the first three modes of resonance for all the sample solutions under test in this chapter, this information is employed to relate the change in resonant frequency to the change in ionic concentration, which can be further inverted to compute the ionic concentration of an arbitrary sample solution with known ion type from its measured resonance characteristics, as described in Chapter 6.

CHAPTER 6. RESULTS AND DISCUSSION

The primary objective of this chapter is to analyze the data obtained from the simulations on HFSS and propose a systematic approach to predict the ionic concentration of an electrolyte solution of known ion type from the measured values of its first three modes of resonant frequency. To achieve this, first it is observed how the resonant frequency data for all the three types of solutions used varies with ionic concentration. This is done by plotting the negative of the shift in resonant frequency for a particular sample from that of deionized water for all three modes of resonance observed against ionic concentration ($-\Delta f_0$, $-\Delta f_1$, $-\Delta f_2$ vs c). The negative values of the resonant frequency shifts are taken so that the resulting function is nonnegative. The plots obtained are illustrated in Figures 6.1 to 6.3. All these data have been taken from Tables 5.2, 5.4, and 5.6.

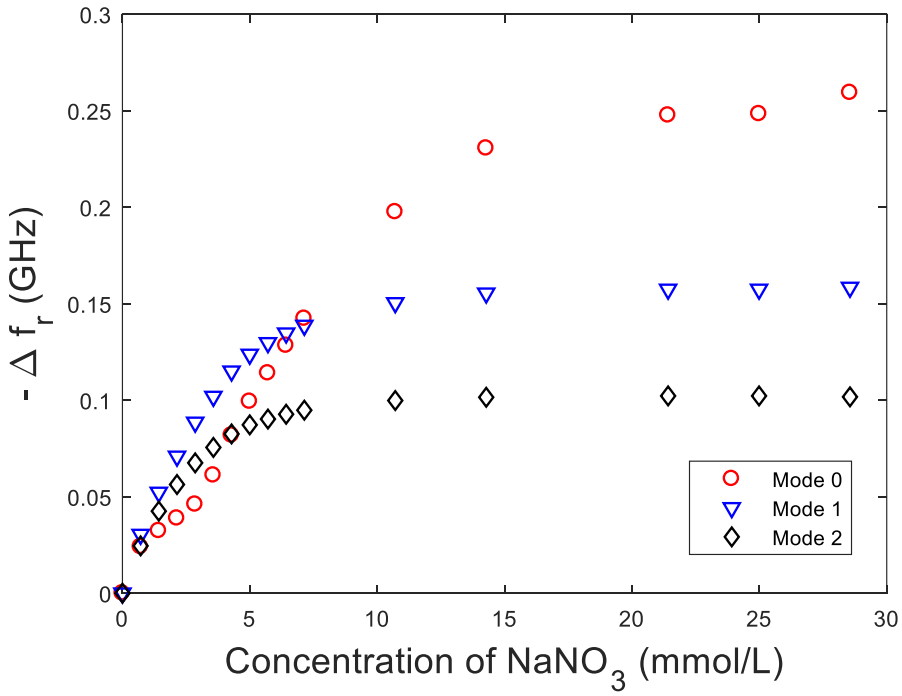

Figure 6.1 Negative of shift in resonant frequency from deionized water plotted against ionic concentration of sodium nitrate sample for the first three modes of resonance

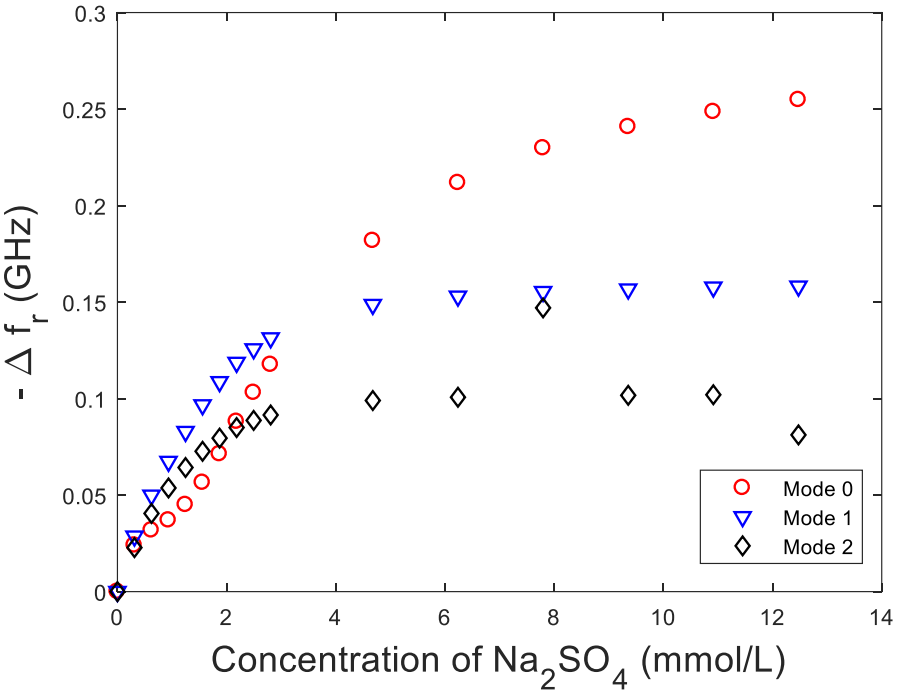

Figure 6.2 Negative of shift in resonant frequency from deionized water plotted against ionic concentration of sodium sulfate sample for the first three modes of resonance

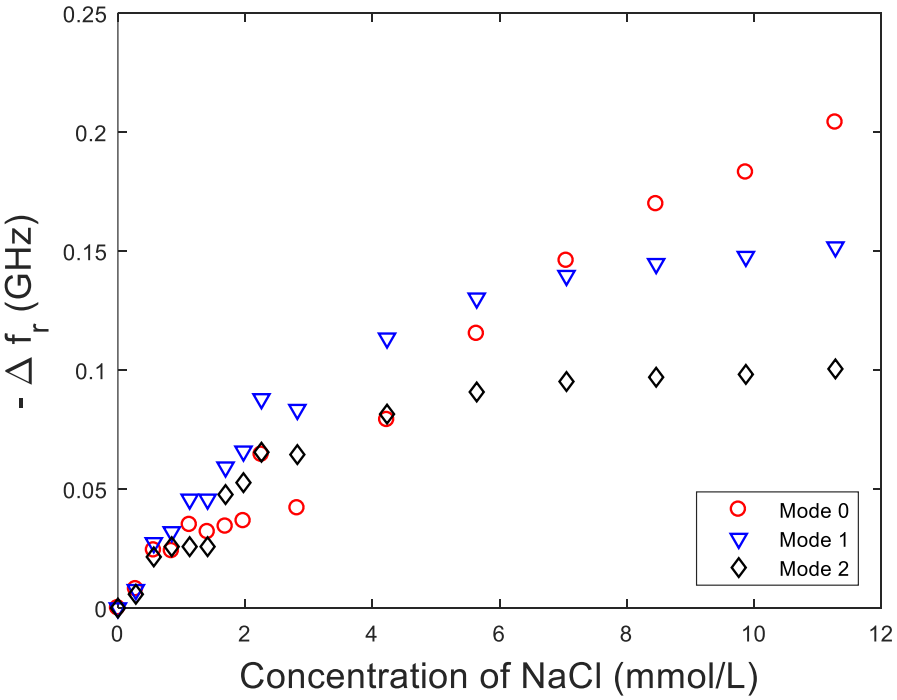

Figure 6.3 Negative of shift in resonant frequency from deionized water plotted against ionic concentration of sodium chloride sample for the first three modes of resonance

From Figures 6.1-6.3, it can be observed that for all three ionic species, for each mode of resonance r, $-\Delta f_r$ increases nonlinearly with concentration. For all three resonant modes, the sensor is sensitive to the lower set of ionic concentrations, whereas the response saturates for higher concentrations. The response for low concentration chloride samples is not as clean as for the other two types of electrolytes. This can be attributed to the fact that, unlike for nitrate and sulfate samples, the real relative permittivity (ε_r') for the lower concentrations of chloride solution increases with concentration. This behavior has been proposed to be a manifestation of the Debye-Falkenhagen Effect in [39].

It can also be observed that for all three ionic species, the shift in resonant frequency seems to follow the same family of functions for modes 1 and 2, and for the higher concentrations for mode 0. The responses for modes 1 and 2 are fitted with an exponential model using a nonlinear, least-squares analysis. The fitting function used is given in Equation (6.1) where r is the mode number, and $\gamma_{r,1}$ and $\gamma_{r,2}$ are the fitting parameters.

$$-\Delta f_r = \gamma_{r,1}(1-e^{-\gamma_{r,2}c}) \qquad for\ r \in \{1,2\} \qquad (6.1)$$

As evident with the naked eye, trying to fit the mode 0 data with the same model yields good agreement for the higher concentrations, but overestimates the shift in resonant frequency for the lower ionic concentrations. For this purpose, an additional function with three fitting parameters is used to produce a good fit for the mode 0 data, as shown in Equation 6.2, where $\gamma_{0,1}$, $\gamma_{0,2}$, $\gamma_{0,3}$, $\gamma_{0,4}$, and $\gamma_{0,5}$ are the fitting parameters used.

$$-\Delta f_0 = \gamma_{0,1}(1-e^{-\gamma_{0,2}c}) - (\gamma_{0,3}ce^{-c^{\gamma_{0,4}}})^{\gamma_{0,5}} \qquad (6.2)$$

The fitted curves have been plotted along with the data points obtained through simulation for all the modes and sample types under test in Figures 6.4 to 6.12. The fitting

parameters used for fitting the mode 0 data are presented in Table 6.1, whereas those for modes 1 and 2 are presented in Table 6.2. The corresponding mean squared error (MSE) for each fit is reported, where mean squared error is given by:

$$MSE = \frac{1}{n-p}\sum_{i=1}^{n}(Y_i - Y_i)^2 \tag{0.1}$$

In Equation (6.3), n represents the number of samples, which is 16 (S0 to S15) in this case, and p stands for the number of fitting parameters. Y_i denotes the measured values of $(-\Delta f_r)$ for the i-th sample, where $r \in \{0, 1, 2\}$, and $\widehat{Y}_i$ stands for the corresponding fitted value.

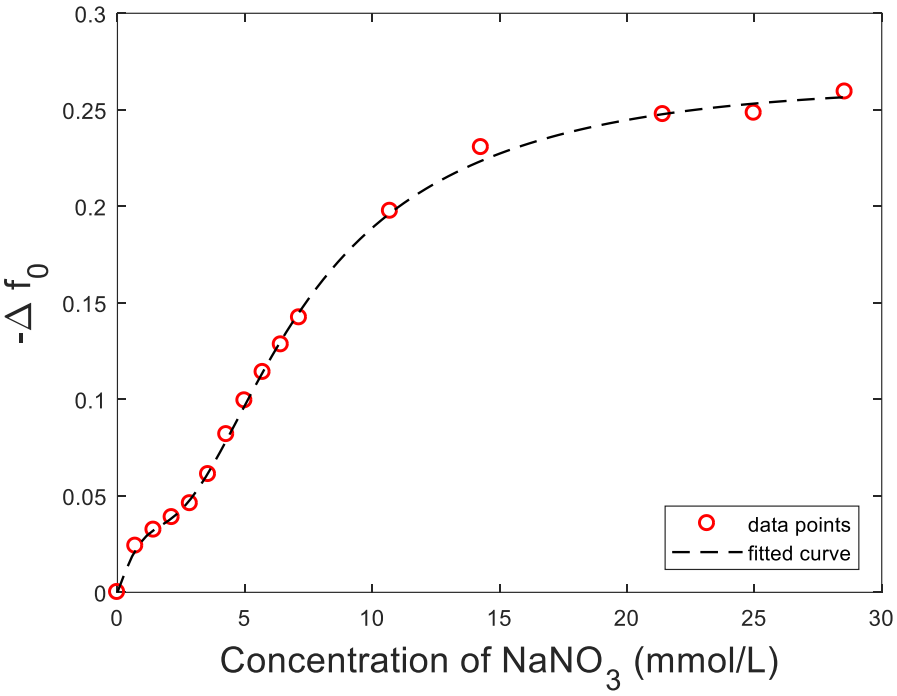

Figure 6.4 Fitted curve for relating shift in Mode 0 resonant frequency with concentration for sodium nitrate sample (fitting parameters presented in Table 6.1)

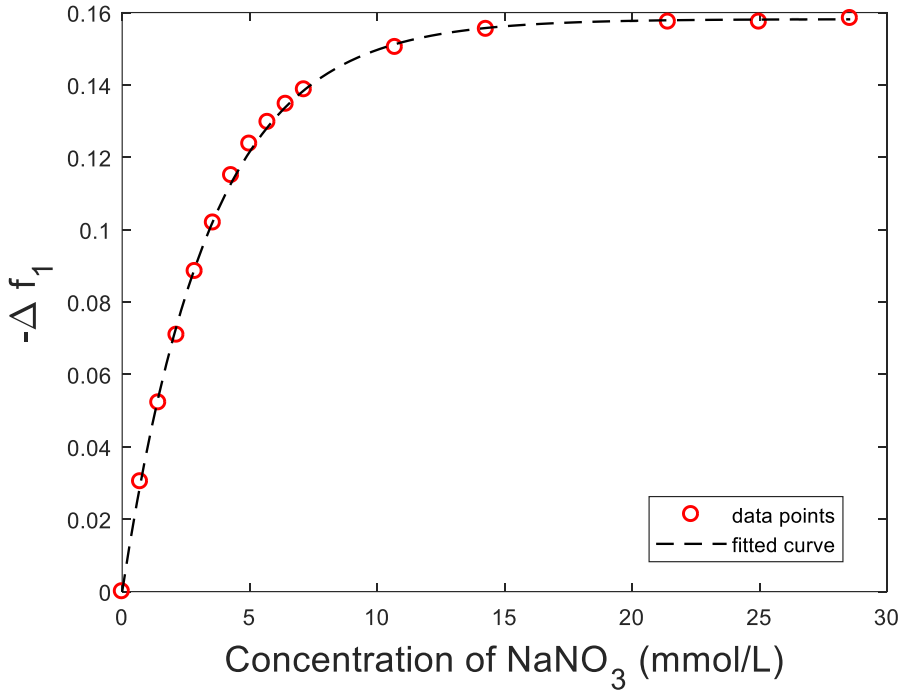

Figure 6.5 Fitted curve for relating shift in Mode 1 resonant frequency with concentration for sodium nitrate sample (fitting parameters presented in Table 6.1)

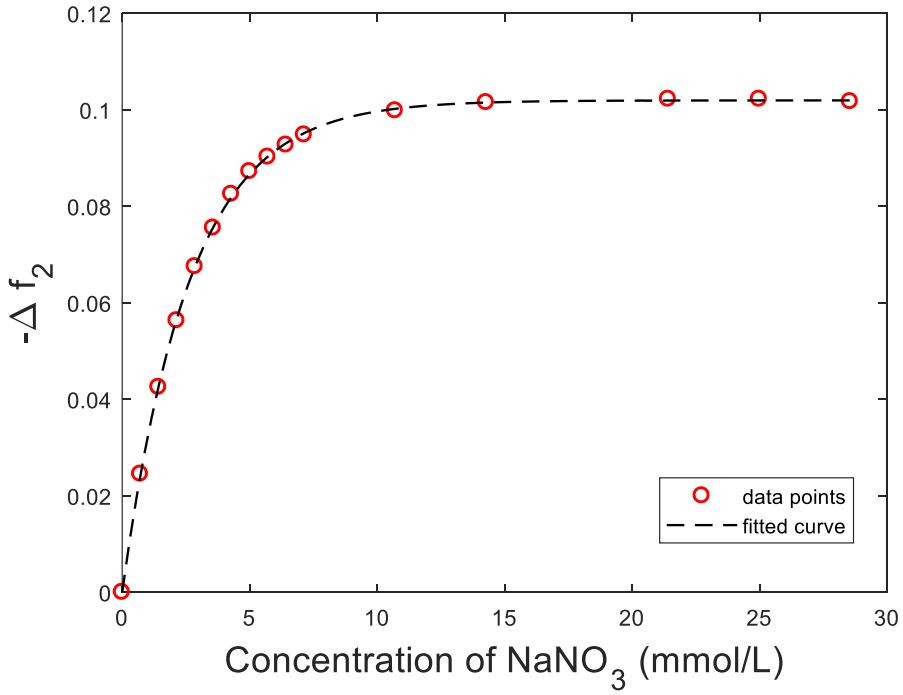

Figure 6.6 Fitted curve for relating shift in Mode 2 resonant frequency with concentration for sodium nitrate sample (fitting parameters presented in Table 6.1)

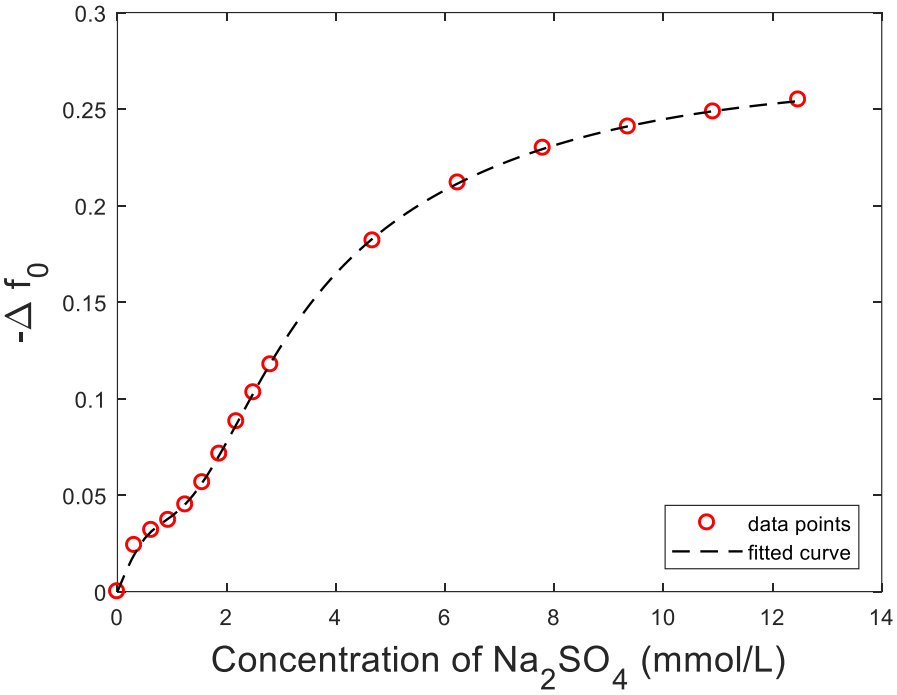

Figure 6.7 Fitted curve for relating shift in Mode 0 resonant frequency with concentration for sodium sulfate sample (fitting parameters presented in Table 6.1)

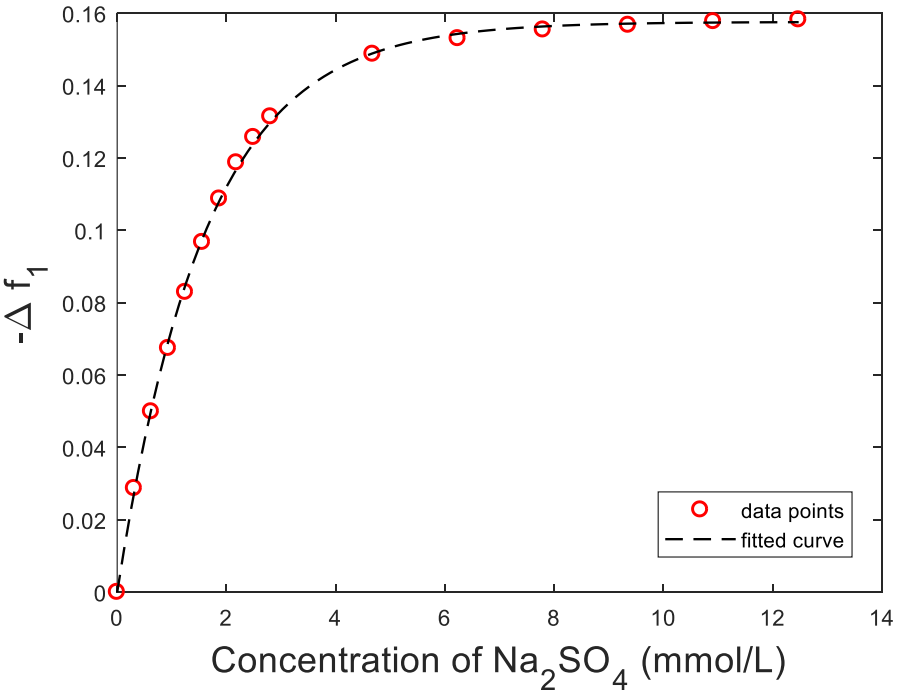

Figure 6.8 Fitted curve for relating shift in Mode1 resonant frequency with concentration for sodium sulfate sample (fitting parameters presented in Table 6.1))

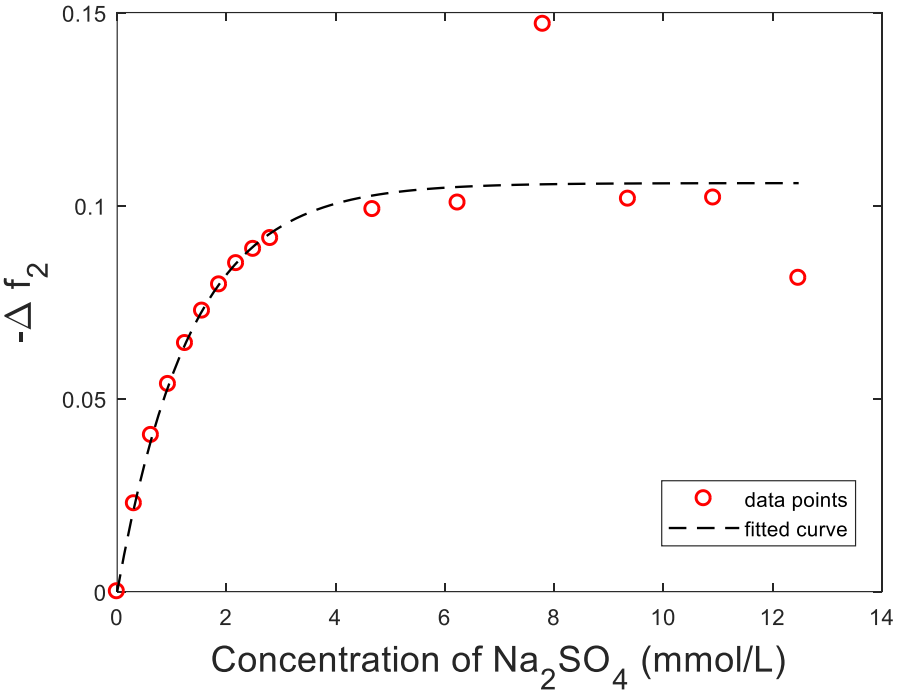

Figure 6.9 Fitted curve for relating shift in Mode 2 resonant frequency with concentration for sodium sulfate sample (fitting parameters presented in Table 6.1)

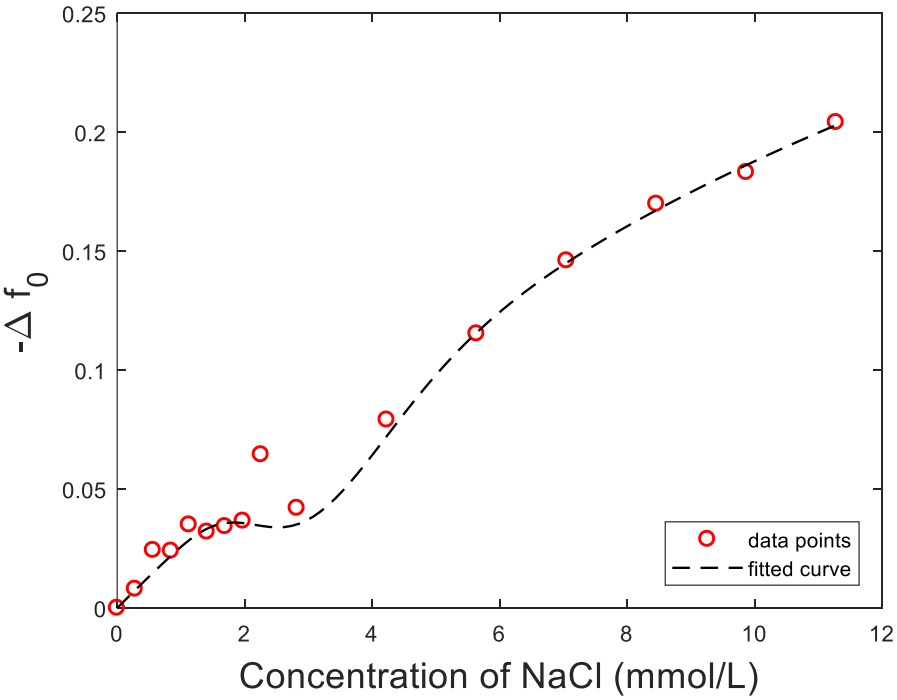

Figure 6.10 Fitted curve for relating shift in Mode 0 resonant frequency with concentration for sodium chloride sample (fitting parameters presented in Table 6.1)

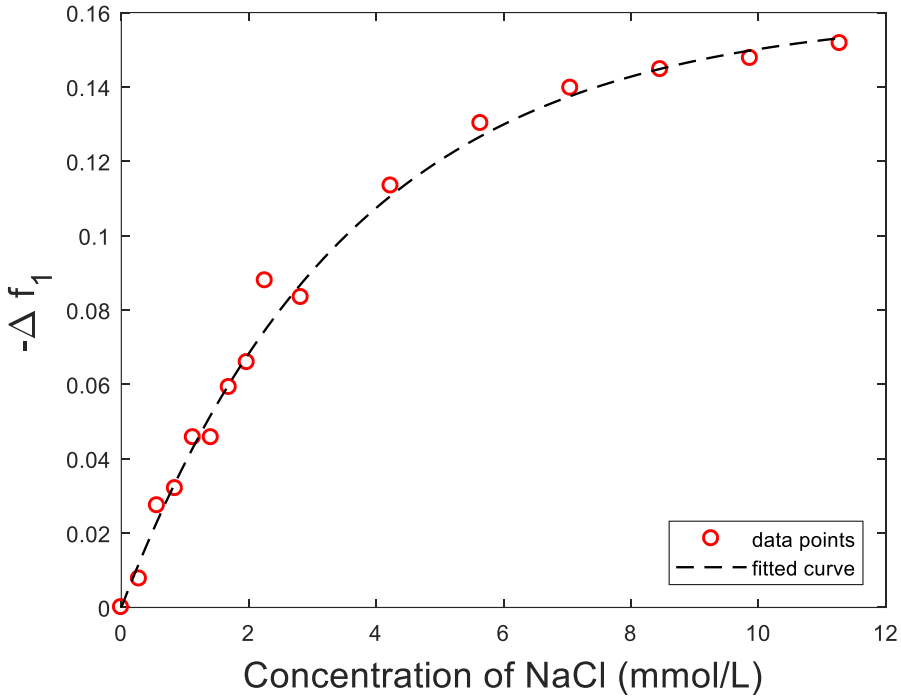

Figure 6.11 Fitted curve for relating shift in Mode 1 resonant frequency with concentration for sodium chloride sample (fitting parameters presented in Table 6.1)

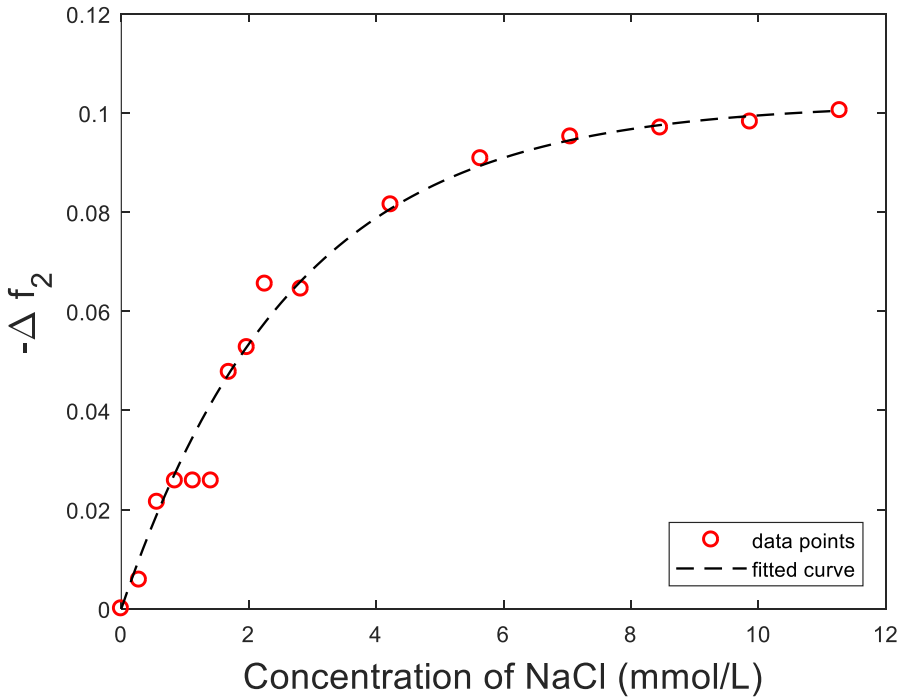

Figure 6.12 Fitted curve for relating shift in Mode 2 resonant frequency with concentration for sodium chloride sample (fitting parameters presented in Table 6.1)

Table 6.1 Values of fitting parameters used and corresponding mean squared errors of fitting (MSE) for Mode 0 for sodium nitrate, sodium sulfate, and sodium chloride solutions

Sample Type	$\gamma_{0,1}$ [L/mmol]	$\gamma_{0,2}$ [L/mmol]	$\gamma_{0,3}$	$\gamma_{0,4}$	$\gamma_{0,5}$	MSE
Sodium Nitrate	0.2618	0.1368	1.069	0.5181	5.456	1.080×10^{-5}
Sodium Sulfate	0.2646	0.2558	1.254	0.7012	4.985	2.393×10^{-6}
Sodium Chloride	0.3485	0.0774	1.648	0.5355	16.53	1.044×10^{-4}

Table 6.2 Values of fitting parameters used and corresponding mean squared errors of fitting (MSE) for Modes 1 and 2 for sodium nitrate, sodium sulfate, and sodium chloride solutions

Sample Type	Mode 1 ($r = 1$)			Mode 2 ($r = 2$)		
	$\gamma_{1,1}$ [L/mmol]	$\gamma_{1,2}$ [L/mmol]	MSE	$\gamma_{2,1}$ [L/mmol]	$\gamma_{2,2}$ [L/mmol]	MSE
Sodium Nitrate	0.1582	0.2926	1.798×10^{-6}	0.1019	0.3797	1.155×10^{-7}
Sodium Sulfate	0.1576	0.6198	1.561×10^{-6}	0.1058	0.7479	1.709×10^{-4}
Sodium Chloride	0.1601	0.2781	1.651×10^{-5}	0.1020	0.3702	9.722×10^{-6}

Using the fitting equations (6.1) and (6.2), and parameters from Tables 6.1 and 6.2, it is possible to estimate the shift in resonant frequency of the sensor for a given concentration of an electrolyte. By the Safe Drinking Water Act, there is a 10 mg/L (or 10 parts per million) standard set for the maximum contaminate level (MCL) of nitrate-nitrogen in drinking water [15]. This corresponds to 0.7139 mmol/L concentration of nitrate ions. The calculated resonant frequency shifts on addition of this concentration to deionized water for the first three resonant modes of the designed resonant sensor are 22.02 MHz, 29.82 MHz, and 24.20 MHz respectively. For the minimum concentration of sulfate measured, i.e. 0.3119 mmol/L, the shifts in resonant frequency from that of deionized water for modes 0,1, and 2 are 19.49 MHz, 27.70 MHz, and 22.01 MHz

respectively. For the minimum concentration of chloride measured, i.e. 0.2821 mmol/L, the corresponding frequency shifts are 7.527 MHz, 12.08 MHz, and 10.12 MHz respectively.

The sensitivity of the resonant sensor for a given mode of resonance r is defined as $|\frac{\partial \Delta f_r}{\partial c}|$ which is equal to $|\frac{\partial f_r}{\partial c}|$. To investigate sensitivity, this parameter is plotted as a function of concentration for all three ion types in Figures 6.13 to 6.18. Figures 6.13, 6.15, and 6.17 present sensor sensitivity for the entire range of concentrations simulated, whereas Figures 6.14, 6.16, and 6.18 focus on a smaller range of concentrations which are agriculturally more relevant. Since the response of the sensor varies nonlinearly with concentration, its sensitivity is not constant but it is too a function of concentration. In Table 6.3 the range in which sensor sensitivity varies as concentration of ion is increased from 0 to 10 mg/L for all three ion types and resonant modes are presented. It is worth mentioning here that the experimental data used for this research has measurements only at 0 and 10 mg/L (corresponding to 0.7139 mmol/L, 0.3119 mmol/L, and 0.2821 mmol/L for nitrate, sulfate, and chloride respectively). Further experimentation is necessary to better understand the behavior of the system for such low concentration ranges.

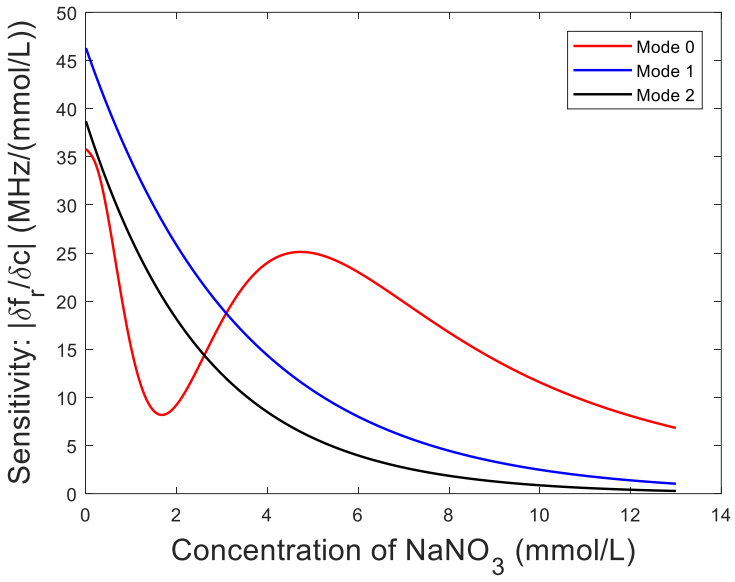

Figure 6.13 Sensor sensitivity to the change in concentration of nitrate ions for the first three resonant modes over entire range of concentrations

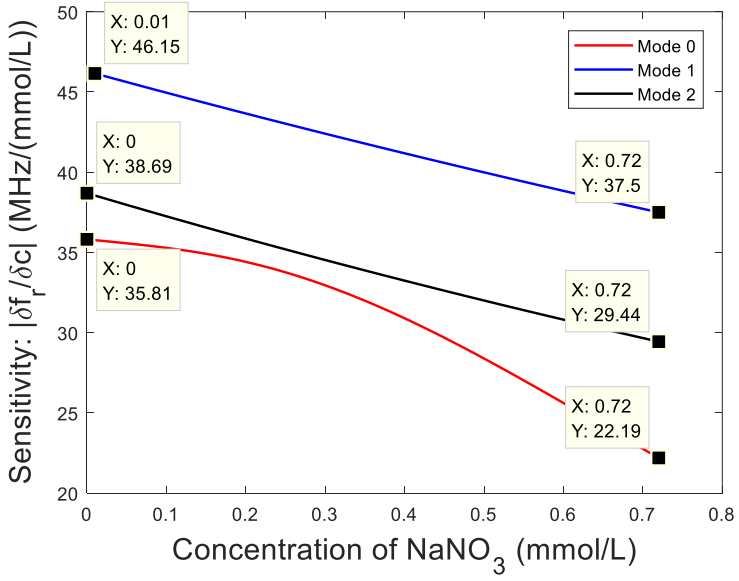

Figure 6.14 Sensor sensitivity to the change in concentration of nitrate ions for the first three resonant modes over a small range of concentrations

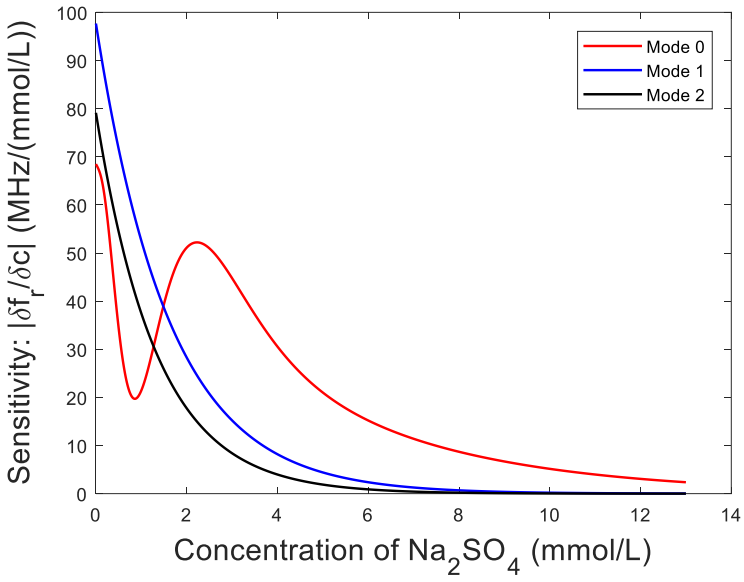

Figure 6.15 Sensor sensitivity to the change in concentration of sulfate ions for the first three resonant modes over entire range of concentrations

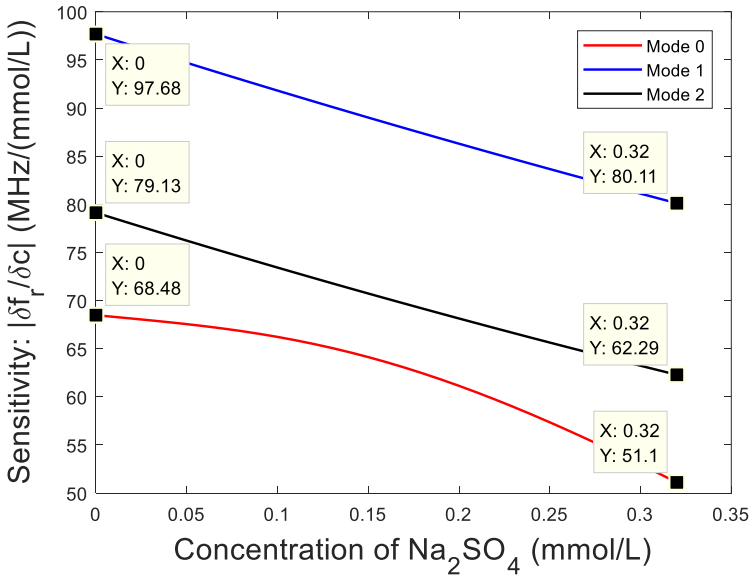

Figure 6.16 Sensor sensitivity to the change in concentration of sulfate ions for the first three resonant modes over a small range of concentrations

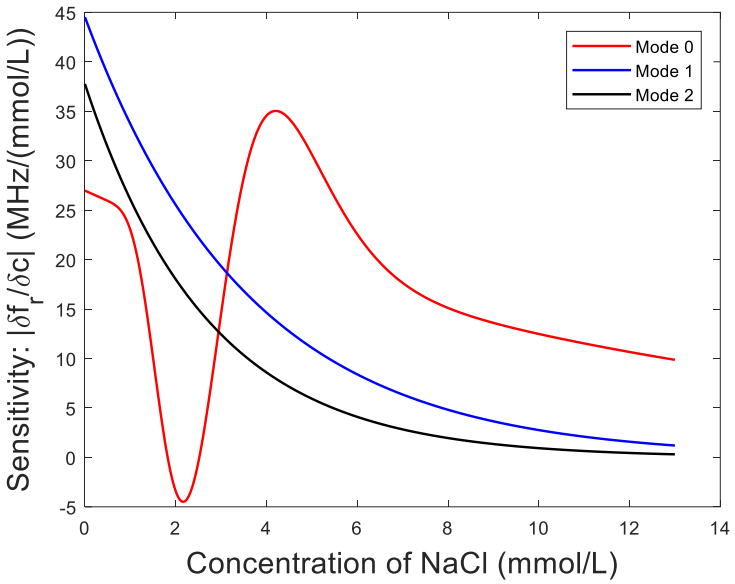

Figure 6.17 Sensor sensitivity to the change in concentration of chloride ions for the first three resonant modes over entire range of concentrations

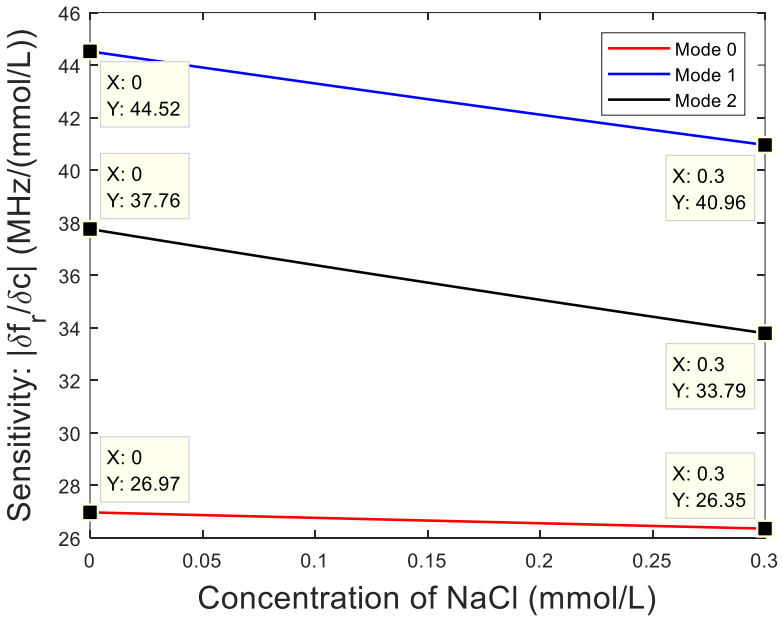

Figure 6.18 Sensor sensitivity to the change in concentration of chloride ions for the first three resonant modes over a small range of concentrations

Table 6.3 Sensitivity of resonant sensor to changes in concentration which are agriculturally relevant for nitrate, sulfate, and chloride ions

Ion Type	Modes	Sensitivity Range (MHz/(mmol/L))
Nitrate	0	35.81 - 22.19
	1	46.29 - 37.50
	2	38.69 - 29.44
Sulfate	0	68.48 - 51.10
	1	97.68 - 80.11
	2	79.13 -62.29
Chloride	0	26.97 - 26.35
	1	44.52 - 40.96
	2	37.76 - 33.79

The difference in behavior of the resonant sensor in its fundamental mode for the lower concentrations of sample solutions from the other resonant modes is further explored. For this purpose, the different contributions to complex permittivity from Equation (2.1) are plotted against ionic concentration for sodium nitrate solutions at three different frequencies – 770 MHz, 1.64 GHz, and 2.57 GHz, which correspond to the first three resonant modes for deionized water sample. Figures 6.19 to 6.23 present these plots.

The imaginary part of permittivity, ε_r is a summation of two components: the dipolar loss ε_d'', and the conductivity contribution $\frac{\sigma}{2\pi\varepsilon_0 f}$. From Figures 6.20 to 6.22, it can be observed that for the samples with higher concentrations of nitrate, the imaginary part of permittivity at 770 MHz is mostly due to the conductivity contribution term, unlike at the two other frequencies for which the data is plotted, where the dipolar loss component provides a more significant contribution. As one moves from higher to lower concentrations, the dipolar loss remains

unchanged at all three frequencies, whereas the conductivity contribution term falls more rapidly for the 770 MHz trace, compared to the other two frequencies. This leads to a lower value of total imaginary permittivity, and loss tangent. These lower values of loss tangent might provide an explanation for lower values of resonant frequency shifts for the fundamental mode of resonance for the lower ionic concentrations than what would be predicted by an exponential fitting function, as is the case for the two higher modes of resonance. More information about the resonant system is required to arrive at a stronger conclusion about the difference in behavior of the fundamental resonant mode, compared with the first and second modes, for the samples of lower concentration.

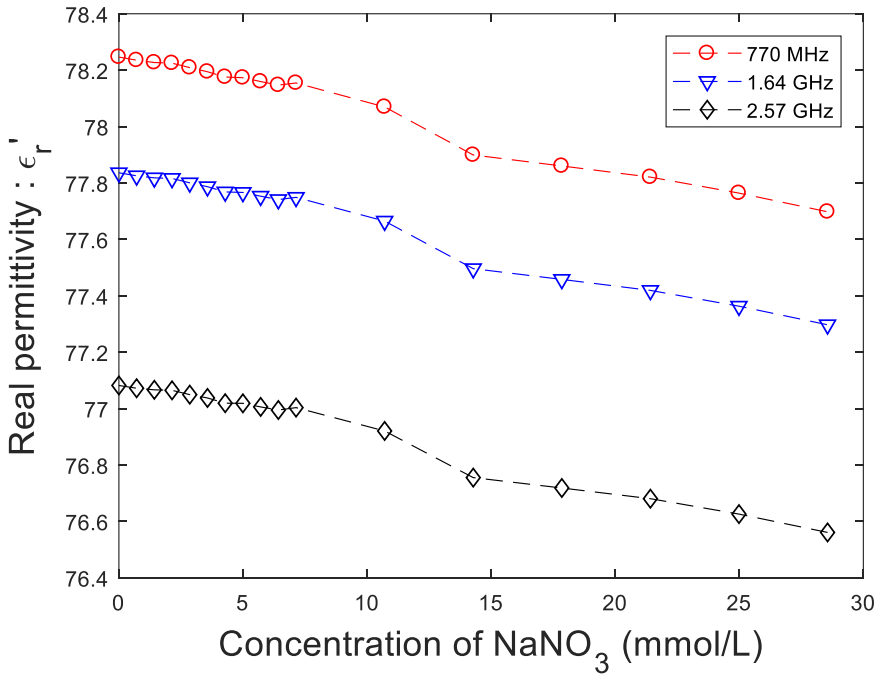

Figure 6.19 Real permittivity of different concentrations of sodium nitrate solution samples at frequencies close to the first three resonant frequencies for deionized water

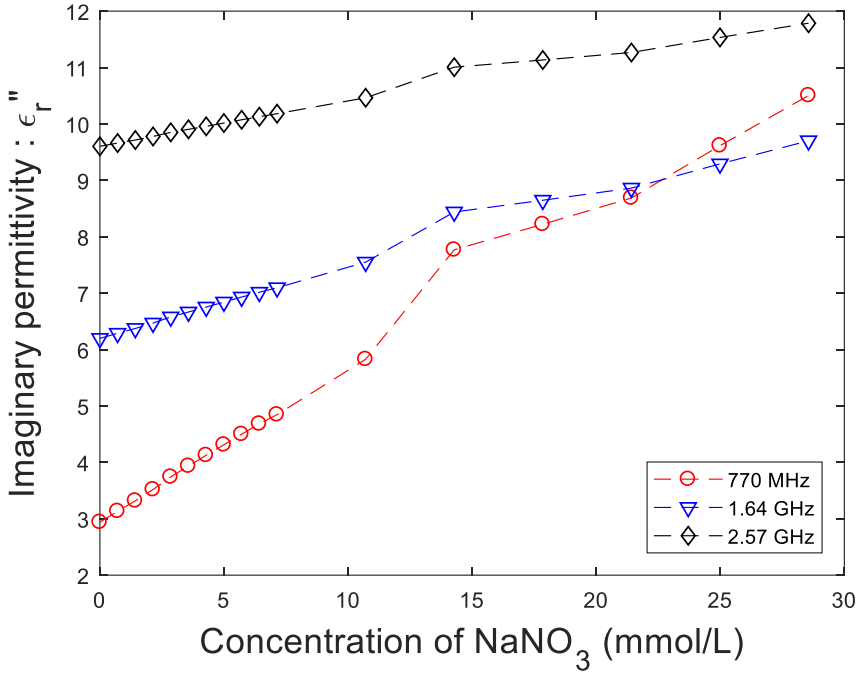

Figure 6.20 Imaginary permittivity of different concentrations of sodium nitrate solution samples at frequencies close to the first three resonant frequencies for deionized water

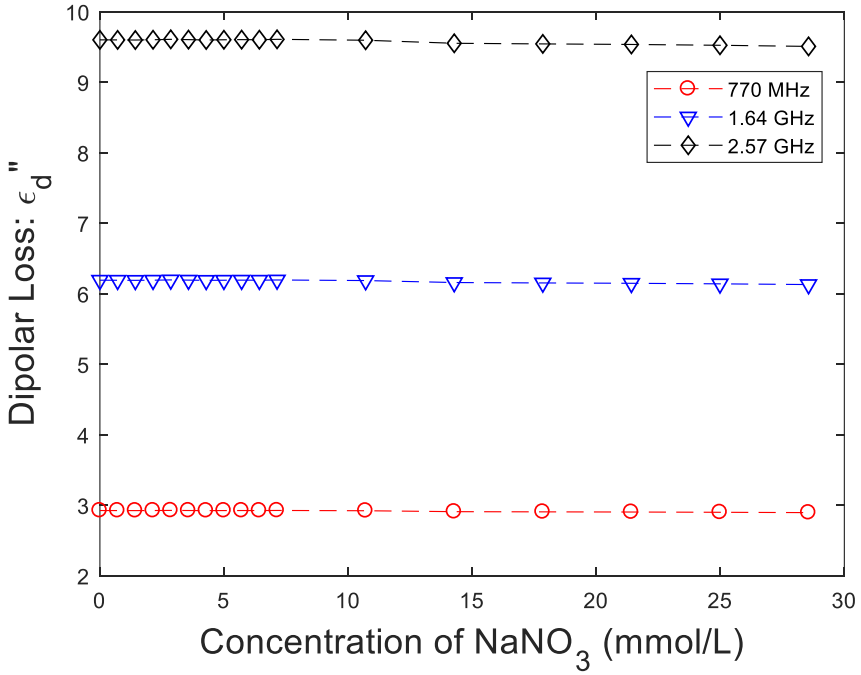

Figure 6.21 Dipolar loss of different concentrations of sodium nitrate solution samples at frequencies close to the first three resonant frequencies for deionized water

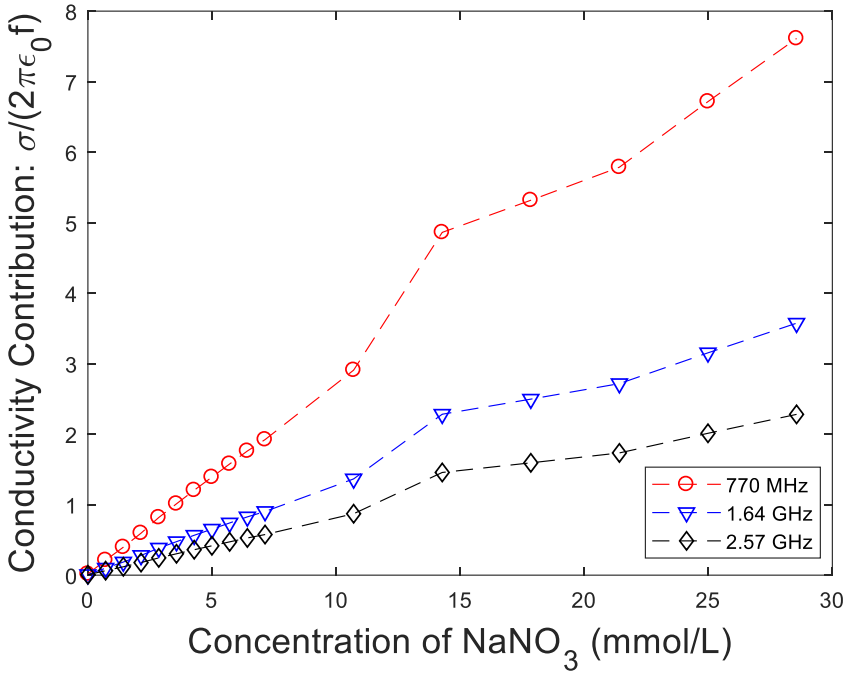

Figure 6.22 Conductivity contribution to imaginary permittivity of different concentrations of sodium nitrate solution samples at frequencies close to the first three resonant frequencies for deionized water

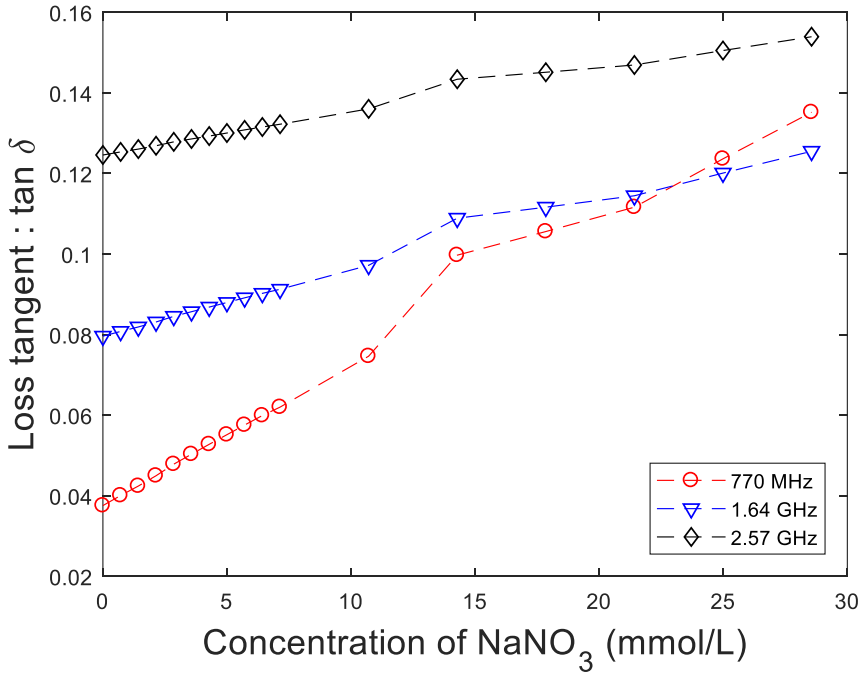

Figure 6.23 Loss tangent of different concentrations of sodium nitrate solution samples at frequencies close to the first three resonant frequencies for deionized water

CHAPTER 7. GENERAL CONCLUSIONS

The preceding chapters have discussed the design of a resonant sensor which should be sensitive to changes in ionic concentrations which are agriculturally relevant. This chapter talks about the feasibility of practically implementing the resonant sensor for measuring ionic concentration of electrolytes. Some comparisons are also drawn with the two existing real-time methods discussed in Chapter 1, viz. the Ion Selective Electrode (ISE) Technology, and Ultraviolet (UV) Absorption Technology. This is followed by a brief discussion on the direction in which research on the coaxial resonant dielectric sensor could potentially progress. Finally, the work presented in this thesis is summarized and concluding statements are made.

7.1 Feasibility of Coaxial Resonant Sensor

The coaxial resonant sensor developed herein has been designed for the purpose of measuring changes in ionic concentration of aqueous solution in the order of mmol/L. In this section, the potential of this design to be implemented as a low cost, highly sensitive, field deployable, real time sensor is explored. These criteria are discussed one-by-one, probable challenges with prospective solutions are discussed, and comparisons are made with existing ionic monitoring systems.

Cost

The designed resonant sensor is potentially low cost due to two reasons.

1. Manufacturing costs are low: The sensor is made of an inexpensive, readily-available RG401 coaxial cable, a coupling structure made of copper, and two SMA receptacles.

These make the manufacturing costs low when compared to a UV absorption sensor. Bulk manufacturing would further lower the costs of production.

2. An expensive Vector Network Analyzer (VNA) is not required: The fact that a resonant sensor solely relies on the measurement of its resonant characteristics, and not on complete S-parameters implies that, unlike for broadband dielectric sensors, a resonant sensor can be used in conjunction with a much simpler and less expensive measuring device than a VNA. A phase locked loop (PLL) can be implemented to generate a frequency stable signal whose frequency corresponds to the ionic concentration of the sample under test that is of critical interest. Several techniques to measure the frequency of such a signal accurately are discussed in [126-127]. The use of one such method would render the resonant sensor developed herein a much more economically viable system than traditional broadband methods as well as the UV absorption sensor. Also, the lower the frequency of operation, the lower would be the cost of the external RF hardware.

Sensitivity

It has been established in Chapter 6 that the designed sensor has the highest sensitivity to a change in ionic concentration at the lower concentrations, which fall in the agriculturally relevant range. For all the three ions, it has been observed that the frequency shift is maximum for Mode 1. It is, however, generally cheaper and easier in terms of hardware requirement, to measure a normalized frequency shift $\left|\frac{\Delta f_r}{f_r}\right|$ which is larger in magnitude. In other words, it is generally more economical to detect a shift in frequency of a given order of magnitude, from a smaller reference frequency than a larger one. The normalized frequency shift can be calculated to be the largest for the fundamental resonant mode for the concentrations of interest.

One challenge to getting the sensitivity results achieved through simulations, in a laboratory experiment could be the high loss in the sensor system, leading to very low values of the magnitude of S_{21} of the two port network. This could be potentially overcome by providing a large input power to the system (in the order of a few Watts), or using a suitable Low Noise Amplifier (LNA) to increase the overall S_{21}, and making it easier to separate the signal from the noise background.

The measured resonances as well as the sensitivity of the resonant sensor are expected to suffer from different types of uncertainties during testing. These uncertainties might arise due to inaccurate machining of sensor dimensions, as well as imperfections in material properties of the sensor and the sensor elements. This calls for the need of rigorous uncertainty analysis of the sensor system.

Field Deployment

The resonant sensor has been designed to fit into standard tile drains of a diameter of 5" and above. The part of the sensor with interacts with the solution can be encapsulated in a thin chemically-inert polymer coating, for example PTFE tape, to prevent the copper conductor from corroding. This will result in the sensor having high durability when compared to an Ion Selective Electrode (ISE) sensor.

The use of a resonant sensor, furthermore, dispenses with the strong need of calibration as common with conventional broadband methods. The coaxial resonant sensor could be used to measure the resonant frequencies of a reference liquid (deionized water), and then installed to monitor the ionic concentration of an arbitrary sample.

In a tile drain containing agricultural efflux, there would be multiple types of compounds dissolved in water. The sensor designed herein, however, can only detect concentration of a

single-ion system. More research needs to be done to understand how complex permittivity changes with frequency in the presence of multiple ions, and that has to be leveraged to modify the sensor to detect ionic concentration in a multi-ion system.

Two other important factors which require further research to make the sensor field deployable are the knowledge of temperature dependence of sensor sensitivity and the performance of the sensor when the sample is flowing. Uneven flow in different parts of the sample may lead to turbulences, locally increasing the temperature of certain regions and thus leading to erroneous results. This can be avoided by either using a suitable microfluidic device [92] or by placing the sensor in a tank adjoining the tile drainage system, as shown in Figure 7.1, where the flow can be expected to be significantly less.

Figure 7.1 Tank adjoining tile drainage system where the resonant sensor could be potentially deployed

Real Time Operation

The interaction of the dipoles in water and the ions with an applied external field is almost instantaneous at the operating frequencies of the sensor, which are far from any relaxation frequency. Even an operation involving the relaxation frequency would be real time for all

practical purposes as the relaxation times are much smaller than what can be perceived by a human operator. The speed of operation is likely to be limited by the speed at which the data can be collected and read.

7.2 Future Work

Driven by the preceding section, the future work on the coaxial resonant sensor to measure ionic concentration would firstly involve building the resonant sensor and testing it in laboratory conditions using a Vector Network Analyzer (VNA). This could be followed by using a comparatively low cost frequency measurement system to measure the frequency shift and dispense with the expensive VNA. The sensitivity of the sensor to manufacturing uncertainties, both for dimensions as well as material properties, and uncertainties in measurements need to be investigated. The temperature dependence of sensor sensitivity also needs to be studied. Dimensional optimizations may be carried out to increase sensitivity of sensor to ionic concentration. This might imply operating at different frequencies. Higher resonant modes may also be explored. An in-depth exploration of the variation of quality factor of the coaxial resonant sensor with changing ionic concentration can further provide more insights into the system.

There also needs to be work done to better understand the ionic system under test. Specifically, more knowledge of the sample under test would help explain better the difference in behavior of the measured fundamental resonant mode for lower ionic concentrations from the other two resonant modes. Further investigation into the dielectric properties of multi-ionic

systems could throw some light onto how to modify the coaxial resonant sensor to detect ions in a practical situation.

7.3 Summary

In this thesis, an open ended resonant coaxial probe has been proposed, with a coupling structure, to take transmission measurements on an electrolyte under test. The dimensions of the resonator and the coupling structure have been optimized, through numerical simulations, to boost sensitivity of the resonant frequency of the system with respect to changes in ionic concentration of the sample, and to have a higher output power to facilitate easier measurements of the resonant characteristics. The sensor arrangement was simulated in HFSS to find the resonant characteristics of the first three resonant modes for samples of varying concentrations of sodium nitrate, sodium, sulfate and sodium chloride. For each ion type and resonant mode, a relationship between the change in concentration and the shift in resonant frequency was developed. It was found that the designed sensor has high sensitivity at low ionic concentrations, which are agriculturally relevant.

REFERENCES

[1] “Understanding the Economics of Tile Drainage | Ag Decision Maker.” [Online]. Available: https://www.extension.iastate.edu/agdm/wholefarm/html/c2-90.html. [Accessed: 22-Oct-2017].

[2] “Planning an agricultural subsurface drainage system: Agricultural Drainage: University of Minnesota Extension.” [Online]. Available: http://www.extension.umn.edu/agriculture/water/planning/planning-a-subsurface-drainage-system/#drain-depth. [Accessed: 22-Oct-2017].

[3] “Operating and Maintaining a Tile Drainage System.” [Online]. Available: http://www.omafra.gov.on.ca/english/engineer/facts/10-091.htm. [Accessed: 22-Oct-2017].

[4] “Drain Spacing Calculations,” iGrow | SDSU Extension. [Online]. Available: http://igrow.org/agronomy/corn/drain-spacing-calculations/. [Accessed: 22-Oct-2017].

[5] “Returns to Farm Drainage | Ohio Ag Manager.” [Online]. Available: http://u.osu.edu/ohioagmanager/2013/01/04/returns-to-farm-drainage/. [Accessed: 22-Oct-2017].

[6] “Iowa farms with good drainage systems did well in drought,” The Gazette. [Online]. Available: http://www.thegazette.com/2013/01/09/iowa-farms-with-good-drainage-systems-did-well-in-drought. [Accessed: 22-Oct-2017].

[7] G. A. Pavelis, Farm Drainage in the United States: History, Status, and Prospects. U.S. Department of Agriculture, Economic Research Service, 1987.

[8] E. Maxwell, E. W. Peterson, and C. M. O'Reilly, "Enhanced Nitrate Reduction within a Constructed Wetland System: Nitrate Removal within Groundwater Flow," Wetlands, vol. 37, no. 3, pp. 413–422, Jun. 2017.

[9] B. A. Zimmerman, "Exploration of ion species in agricultural subsurface drainage waters," M.S., Iowa State University, United States -- Iowa, 2016.

[10] "How Minerals Affect the Water Supplies." [Online]. Available: http://www.ndhealth.gov/wq/gw/pubs/mineral.htm. [Accessed: 22-Oct-2017].

[11] "1. EUTROPHICATION." [Online]. Available: http://people.oregonstate.edu/~muirp/eutrophi.htm. [Accessed: 22-Oct-2017].

[12] D. A. Kovacic, R. M. Twait, M. P. Wallace, and J. M. Bowling, "Use of created wetlands to improve water quality in the Midwest—Lake Bloomington case study," Ecol. Eng., vol. 28, no. 3, pp. 258–270, Dec. 2006.

[13] R. E. Turner, N. N. Rabalais, and D. Justić, "Predicting summer hypoxia in the northern Gulf of Mexico: Redux," Mar. Pollut. Bull., vol. 64, no. 2, pp. 319–324, Feb. 2012.

[14] K. E. Schilling and R. D. Libra, "The Relationship of Nitrate Concentrations in Streams to Row Crop Land Use in Iowa," J. Environ. Qual., vol. 29, no. 6, pp. 1846–1851, 12/01 2000.

[15] W. Stowe, "Swimming Upstream: Des Moines Water Works Asks for Agricultural Accountability in A State that Claims to ĹFeed the Worldĺ," Rootstalk. A Prairie Journal of Culture, Science and the Arts, no. 2.1, pp. 32-37.2016.

[16] G. R. Hallberg, and B. C. Kross, “Iowa statewide rural well water survey summary of results,” Department of Natural Resources Geological Survey Bureau and University of Iowa Center for Health Effects of Environmental Contamination 52242, Iowa City, IA, Iowa, 1990.

[17] A. J. De Roos, M. H. Ward, C. F. Lynch, and K. P. Cantor, “Nitrate in Public Water Supplies and the Risk of Colon and Rectum Cancers,” Epidemiology, vol. 14, no. 6, pp. 640–649, Nov. 2003.

[18] M. H. Ward, “Too Much of a Good Thing? Nitrate from Nitrogen Fertilizers and Cancer,” Rev. Environ. Health, vol. 24, no. 4, pp. 357–363, 2011.

[19] J. D. Brender et al., “Prenatal Nitrate Intake from Drinking Water and Selected Birth Defects in Offspring of Participants in the National Birth Defects Prevention Study,” Environ. Health Perspect., vol. 121, no. 9, pp. 1083–1089, Sep. 2013.

[20] “NITRATE IN DRINKING WATER: A Public Health Concern For All Iowans.” [Online]. Available: http://www.iaenvironment.org/webres/File/News%20%26%20Resources/Publications/Nitrate_in_Drinking_Water_Report_ES_Web.pdf. [Accessed: 22-Oct-2017].

[21] “3. Hazards in drinking-water supply and waste management.” [Online]. Available http://www.who.int/water_sanitation_health/hygiene/plumbing3.pdf. [Accessed: 22-Oct-2017].

[22] G. Venkatesan and G. Swaminathan, “Review of chloride and sulphate attenuation in ground water nearby solid-waste landfill sites,” J. Environ. Eng. Landsc. Manag., vol. 17, no. 1, pp. 1–7, Mar. 2009.

[23] "Sulfate in Well Water - EH: Minnesota Department of Health." [Online]. Available: http://www.health.state.mn.us/divs/eh/wells/waterquality/sulfate.html. [Accessed: 22-Oct-2017].

[24] "Sulfate as a Contaminant in Freshwater Ecosystems: Sources, Impacts and Mitigation." [Online]. Available: http://conference.ifas.ufl.edu/ncer2011/Presentations/Wednesday/Waterview%20C-D/am/0850_Orem.pdf. [Accessed: 22-Oct-2017].

[25] O. Korostynska, A. Mason, and A. I. Al-Shamma'a, "Monitoring Pollutants in Wastewater: Traditional Lab Based versus Modern Real-Time Approaches," in Smart Sensors for Real-Time Water Quality Monitoring, Springer, Berlin, Heidelberg, 2013, pp. 1–24.

[26] M. J. Moorcroft, J. Davis, and R. G. Compton, "Detection and determination of nitrate and nitrite: a review," Talanta, vol. 54, no. 5, pp. 785–803, Jun. 2001.

[27] H. B. Glasgow, J. M. Burkholder, R. E. Reed, A. J. Lewitus, and J. E. Kleinman, "Real-time remote monitoring of water quality: a review of current applications, and advancements in sensor, telemetry, and computing technologies," J. Exp. Mar. Biol. Ecol., vol. 300, no. 1, pp. 409–448, Mar. 2004.

[28] R. P. Buck, "Ion selective electrodes," Anal. Chem., vol. 50, no. 5, pp. 17–29, Apr. 1978.

[29] P. J. Milham, A. S. Awad, R. E. Paull, and J. H. Bull, "Analysis of plants, soils and waters for nitrate by using an ion-selective electrode," Analyst, vol. 95, no. 1133, pp. 751–757, 1970.

[30] W. E. Morf, “The Principles of Ion-Selective Electrodes and of Membrane Transport,” Elsevier, 2012.

[31] E. M. Gross, R. S. Kelly, and D. M. Cannon, “Analytical Electrochemistry: Potentiometry,” Journal of Analytical Sciences, 2008.

[32] C. Hu, F. E. Muller-Karger, and R. G. Zepp, “Absorbance, absorption coefficient, and apparent quantum yield: A comment on common ambiguity in the use of these optical concepts,” Limnol. Oceanogr., vol. 47, no. 4, pp. 1261–1267, Jul. 2002.

[33] B. A. Pellerin, B. A. Bergamaschi, B. D. Downing, J. F. Saraceno, J. D. Garrett, and L. D. Olsen, “Optical techniques for the determination of nitrate in environmental waters: Guidelines for instrument selection, operation, deployment, maintenance, quality assurance, and data reporting,” U.S. Geological Survey, Reston, VA, USGS Numbered Series 1-D5, 2013.

[34] A. Volkov and A. Prokhorov, “Broadband Dielectric Spectroscopy of Solids,” Radiophys. Quantum Electron., vol. 46, no. 8/9, pp. 657–665, Aug. 2003.

[35] W. D. Callister , “Electrical Conduction in Ionic Ceramics and in Polymers”, Materials Science and Engineering: An Introduction,7th Edn., Wiley & Sons, Inc., 2007, pp. 700-711.

[36] N. Nandi, K. Bhattacharyya, and B. Bagchi, “Dielectric Relaxation and Solvation Dynamics of Water in Complex Chemical and Biological Systems,” Chem. Rev., vol. 100, no. 6, pp. 2013–2046, Jun. 2000.

[37] R. Viana, P. Lunkenheimer, J. Hemberger, R. Böhmer, and A. Loidl, “Dielectric spectroscopy in SrTiO3,” Phys. Rev. B, vol. 50, no. 1, pp. 601–604, Jul. 1994.

[38] F. Bordi, C. Cametti, and R. H. Colby, “Dielectric spectroscopy and conductivity of polyelectrolyte solutions,” J. Phys. Condens. Matter, vol. 16, no. 49, p. R1423, 2004.

[39] A. Gorji, “Dielectric spectroscopy of agriculturally relevant electrolyte systems in water sources,” PhD, Iowa State University, 2018. (*in preparation*)

[40] J. F. Rouleau, J. Goyette, T. K. Bose, and M. F. Frechette, “Performance of a microwave sensor for the precise measurement of water vapor in gases,” IEEE Trans. Dielectr. Electr. Insul., vol. 7, no. 6, pp. 825–831, Dec. 2000.

[41] U. Kaatze and Y. Feldman, “Broadband dielectric spectrometry of liquids and biosystems,” Meas. Sci. Technol., vol. 17, no. 2, p. R17, 2006.

[42] M.-M. Huang, Y. Jiang, P. Sasisanker, G. W. Driver, and H. Weingärtner, “Static Relative Dielectric Permittivities of Ionic Liquids at 25 °C,” J. Chem. Eng. Data, vol. 56, no. 4, pp. 1494–1499, Apr. 2011.

[43] A. Naylon, “Microwave resonant sensors,” PhD, Cardiff University, 2011.

[44] D. J. Rowe, “Microfluidic microwave resonant sensors,” PhD, Cardiff University, 2012.

[45] A. Gorji, A. L. Kaleita, and N. Bowler, "Towards low-cost sensors for real-time monitoring of contaminant ions in water sources," in Microwave Symposium (IMS), IEEE MTT-S International, Honolulu, HI, USA, 2017, pp. 1-4.

[46] A. Gorji and N. Bowler, "Static permittivity of environmentally-relevant low-concentration aqueous solutions of NaCl, NaNO3, and Na2SO4," The Journal of Chemical Physics, (*in preparation*)

[47] H. P. Schwan, “Electrode Polarization Impedance and Measurements in Biological Materials*,” Ann. N. Y. Acad. Sci., vol. 148, no. 1, pp. 191–209, Feb. 1968.

[48] P. Debye, “Polar molecules,” Chemical Catalog Company, Incorporated, 1929.

[49] "A Guide to the characterization of dielectric materials at RF and microwave Frequencies" , The Institute of Measurement and Control (IMC) and The National Physical Laboratory (NPL) , London, ISBN 0 904457 38 9, 2003.

[50] S. I. Watanabe, H. Taki, T. Nojima, and O. Fujiwara, “Characteristics of the SAR distributions in a head exposed to electromagnetic fields radiated by a hand-held portable radio,” IEEE Trans. Microw. Theory Tech., vol. 44, no. 10, pp. 1874–1883, Oct. 1996.

[51] R. J. Weber, “Introduction to Microwave Circuits,” Wiley-IEEE Press, 2001.

[52] M. Steel, R. J. Sheppard and E. H. Grant, "A precision method for measuring the complex permittivity of solid tissue in the frequency domain between 2 and 18 GHz.", J Phys. E:Sci Instrum., Vol. 17, pp. 30-34, 1984.

[53] L. Zanforlin, "Permittivity measurements of lossy liquids at millimeterwave frequencies", Trans. IEEE Microw. Theory Tech., Vol. 31, No. 5, pp. 417-419, 1983.\

[54] S. Roberts and A. von Hippel, "A new method for measuring dielectric constant and loss in the range of centimetre waves", J. Appl. Phys., Vol. 17, pp. 610-616, 1946.

[55] J. Baker-Jarvis, M. D. Janezic and R. B. Stafford , "Shielded open circuited sample holders for dielectric and magnetic measurements on fluids and powders", NIST Report, NISTIR 5001, 1993.

[56] R. Van Loon and R. Finsy, "Measurement of complex permittivity of liquids at frequencies from 5 to 40 GHz", Rev. Sci. Instrum., Vol. 44, No. 9, pp. 1204-1208, 1973.

[57] J. Baker-Jarvis, "Transmission/ Reflection and Short-Circuit Line Permittivity Measurements", NIST Technical Note 1341, 1990.

[58] S. Jenkins, T. E. Hodgetts, R. N. Clarke and A. W. Preece , "Dielectric measurements on reference liquids using automatic network analysers and calculable geometries", Meas. Sci. Tech., Vol. 1, pp. 691-702, 1990.

[59] J. M. Neu, G. Roussy and J. L. Rivail , "Influence de la présence d'un ménisque dans la détermination des propriétés diélectriques par la méthode de von Hippel en ligne coaxiale", Rev. Phys. Appl., Vol. 3, pp. 400-404, 1968.

[60] R. J. Sheppard and E. H. Grant, "Design and construction of a coaxial cell for measuring the complex permittivity of a liquid", J. Phys. E: Sci. Instrum., Vol. 5, pp. 1208-1212, 1972.

[61] J. Hunger, I. Cerjak, H. Schoenmaker, M. Bonn, and H. J. Bakker, "Precision waveguide system for measurement of complex permittivity of liquids at frequencies from 60 to 90 GHz," *Rev. Sci. Instrum.*, vol. 82, no. 10, p. 104703, Oct. 2011.

[62] D. K. Misra, "A Quasi-Static Analysis of Open-Ended Coaxial Lines (Short Paper)," IEEE Trans. Microw. Theory Tech., vol. 35, no. 10, pp. 925–928, Oct. 1987.

[63] D. M. Pozar, "Microwave Engineering," 3rd ed. New York: Wiley, 2009.

[64] C. Gabriel, T. Y. A. Chan, and E. H. Grant, "Admittance models for open ended coaxial probes and their place in dielectric spectroscopy," Phys. Med. Biol., vol. 39, no. 12, p. 2183, 1994.

[65] A. P. Gregory and R. N. Clarke, "Dielectric metrology with coaxial sensors," Meas. Sci. Technol., vol. 18, no. 5, p. 1372, 2007.

[66] M. Okoniewski, J. Anderson, E. Okoniewska, K. Caputa, and S. S. Stuchly, "Further analysis of open-ended dielectric sensors," IEEE Trans. Microw. Theory Tech., vol. 43, no. 8, pp. 1986–1989, Aug. 1995.

[67] R. Olmi, M. Bini, R. Nesti, G. Pelosi, and C. Riminesi, "Improvement of the Permittivity Measurement by a 3d Full-wave Analysis of a Finite Flanged Coaxial Probe," J. Electromagn. Waves Appl., vol. 18, no. 2, pp. 217–232, Jan. 2004.

[68] A. P. Gregory and R. N. Clarke, "A review of RF and microwave techniques for dielectric measurements on polar liquids," IEEE Trans. Dielectr. Electr. Insul., vol. 13, no. 4, pp. 727–743, Aug. 2006.

[69] A. Kraszewski, M. A. Stuchly, and S. S. Stuchly, "ANA Calibration Method for Measurements of Dielectric Properties," IEEE Trans. Instrum. Meas., vol. 32, no. 2, pp. 385–387, Jun. 1983.

[70] G. P. Otto and W. C. Chew, "Improved calibration of a large open-ended coaxial probe for dielectric measurements," IEEE Trans. Instrum. Meas., vol. 40, no. 4, pp. 742–746, Aug. 1991.

[71] J. P. Grant, R. N. Clarke, G. T. Symm, and N. M. Spyrou, "In vivo dielectric properties of human skin from 50 MHz to 2.0 GHz," Phys. Med. Biol., vol. 33, no. 5, p. 607, 1988.

[72] T. Friisø and T. Tjomsland, "Monitoring of density changes in low-permittivity liquids by microwave-permittivity measurements with an open-ended probe," Meas. Sci. Technol., vol. 8, no. 11, p. 1295, 1997.

[73] D. Popovic et al., "Precision open-ended coaxial probes for in vivo and ex vivo dielectric spectroscopy of biological tissues at microwave frequencies," IEEE Trans. Microw. Theory Tech., vol. 53, no. 5, pp. 1713–1722, May 2005.

[74] K. Folgero, T. Friiso, J. Hilland, and T. Tjomsland, "A broad-band and high-sensitivity dielectric spectroscopy measurement system for quality determination of low-permittivity fluids," Meas. Sci. Technol., vol. 6, no. 7, p. 995, 1995.

[75] S. Fan and D. Misra, "A study on the metal-flanged open-ended coaxial line terminating in a conductor-backed dielectric layer," in 7th IEEE Conference on Instrumentation and Measurement Technology, 1990, pp. 43–46.

[76] A. P. Gregory and R. N. Clarke, "Traceable measurements on dielectric reference liquids over the temperature range 10 - 50 /spl deg/C using coaxial-line methods," in Conference Digest Conference on Precision Electromagnetic Measurements, 2002, pp. 102–103.

[77] J. K. Piotrowski and J. Chramiec, "Broad-Band Dielectric Probe with a Coaxial Line - Circular Waveguide Junction," in 2000 30th European Microwave Conference, 2000, pp. 1–4.

[78] M. Hirano, M. Takahashi, and M. Abe, "A measurement of complex permittivity of lossy dielectrics by using flanged rectangular waveguide," Electron. Commun. Jpn. Part II Electron., vol. 84, no. 4, pp. 59–67, Apr. 2001.

[79] Sphicopoulos, V. Teodoridis, and F. Gardiol, "Simple Nondestructive Method for the Measurement of Material Permittivity," J. Microw. Power, vol. 20, no. 3, pp. 165–172, Jan. 1985.

[80] K. Bois, A. Benally, and R. Zoughi, “Two-Port Network Analyzer Dielectric Constant Measurement of Granular or Liquid Materials for the Study of Cement Based Materials,” in Nondestructive Characterization of Materials VIII, Springer, Boston, MA, 1998, pp. 291–296.

[81] K. Shibata, K. Tani, O. Hashimoto, and K. Wada, “Measurement of Complex Permittivity for Liquid Phantom by Transmission Line Method Using Coaxial Line,” IEICE Trans. Electron., vol. E87–C, no. 5, pp. 689–693, May 2004.

[82] S. Szwarnowski, “A transmission line cell for measuring the permittivity of liquids over the frequency range 90 MHz to 2 GHz,” J. Phys. [E], vol. 15, no. 10, p. 1068, 1982.

[83] S. Jenkins, T. E. Hodgetts, R. N. Clarke, and A. W. Preece, “Dielectric measurements on reference liquids using automatic network analysers and calculable geometries,” Meas. Sci. Technol., vol. 1, no. 8, p. 691, 1990.

[84] U. Kaatze, R. Pottel, and A. Wallusch, “A new automated waveguide system for the precise measurement of complex permittivity of low-to-high-loss liquids at microwave frequencies,” Meas. Sci. Technol., vol. 6, no. 8, p. 1201, 1995.

[85] N. Ueda, Y. Kuriyama, A. Nishikata, N. Fukunaga, S. Watanabe, and Y. Yamanaka, “Liquid material’s complex permittivity measurement using seamless dielectric tube and rectangular waveguide,” in 2004 Asia-Pacific Radio Science Conference, 2004. Proceedings., 2004, p. 537-.

[86] Stuchly, S. S., and C. E. Bassey. "Microwave coplanar sensors for dielectric measurements." Measurement Science and Technology 9.8 (1998): 1324.

[87] S. S. Stuchly and C. E. Bassey, “Microwave coplanar sensors for dielectric measurements,” Meas. Sci. Technol., vol. 9, no. 8, p. 1324, 1998.

[88] M. R. Tofighi and A. Daryoush, “Comparison of two post-calibration correction methods for complex permittivity measurement of biological tissues up to 50 GHz,” IEEE Trans. Instrum. Meas., vol. 51, no. 6, pp. 1170–1176, Dec. 2002.

[89] J. Hefti, A. Pan, and A. Kumar, “Sensitive detection method of dielectric dispersions in aqueous-based, surface-bound macromolecular structures using microwave spectroscopy,” Appl. Phys. Lett., vol. 75, no. 12, pp. 1802–1804, Sep. 1999.

[90] F. Kremer and A. Schönhals, “The Scaling of the Dynamics of Glasses and Supercooled Liquids,” in Broadband Dielectric Spectroscopy, Springer, Berlin, Heidelberg, 2003, pp. 99–129.

[91] R. A. Waldron, “Perturbation theory of resonant cavities,” Proc. IEE - Part C Monogr., vol. 107, no. 12, pp. 272–274, Sep. 1960.

[92] D. J. Rowe, A. Porch, D. A. Barrow, and C. J. Allender, “Microfluidic device for compositional analysis of solvent systems at microwave frequencies,” Sens. Actuators B Chem., vol. 169, no. Supplement C, pp. 213–221, Jul. 2012.

[93] K. H. Hong and J. A. Roberts, “Microwave properties of liquids and solids using a resonant microwave cavity as a probe,” J. Appl. Phys., vol. 45, no. 6, pp. 2452–2456, Jun. 1974.

[94] K. B. Yu, S. G. Ogourtsov, V. G. Belenky, A. B. Maslenikov, and A. S. Omar, “Accurate microwave resonant method for complex permittivity measurements of liquids [biological],” IEEE Trans. Microw. Theory Tech., vol. 48, no. 11, pp. 2159–2164, Nov. 2000.

[95] M. Regier and H. Schubert, “Dielectric Properties at Microwave Frequencies Studied in Partially Filled Cylindrical TE011 Cavities,” J. Microw. Power Electromagn. Energy, vol. 35, no. 1, pp. 25–33, Jan. 2000.

[96] G. Tsankova, M. Richter, A. Madigan, P. L. Stanwix, E. F. May, and R. Span, “Characterisation of a microwave re-entrant cavity resonator for phase-equilibrium

measurements and new dew-point data for a (0.25 argon + 0.75 carbon dioxide) mixture," J. Chem. Thermodyn., vol. 101, pp. 395–404, Oct. 2016.

[97] R. N. Clarke, et al, 'A guide to the characterisation of dielectric materials at RF and microwave frequencies," Institute of Measurement and Control/National Physical Laboratory, 2003.

[98] G. Gennarelli, S. Romeo, M. R. Scarfì, and F. Soldovieri, "A Microwave Resonant Sensor for Concentration Measurements of Liquid Solutions," IEEE Sens. J., vol. 13, no. 5, pp. 1857–1864, May 2013.

[99] J. Krupka, K. Derzakowski, M. D. Janezic, and J. Baker-Jarvis, "TE018 Dielectric-Resonator Technique for Precise Measurements of the Complex Permittivity of Lossy Liquids at Frequencies Below 1 GHz*," in 2004 Conference on Precision Electromagnetic Measurements, 2004, pp. 469–470.

[100] A. I. Gubin, A. A. Barannik, N. T. Cherpak, S. Vitusevich, A. Offenhaeusser, and N. Klein, "Whispering-gallery mode resonator technique for characterization of small volumes of biochemical liquids in microfluidic channel," in 2011 41st European Microwave Conference, 2011, pp. 615–618.

[101] J. Krupka and J. Mazierska, "Contactless Measurements of Resistivity of Semiconductor Wafers Employing Single-Post and Split-Post Dielectric-Resonator Techniques," IEEE Trans. Instrum. Meas., vol. 56, no. 5, pp. 1839–1844, Oct. 2007.

[102] U. Raveendranath, S. Bijukumar, and K. T. Mathew, "Broadband coaxial cavity resonator for complex permittivity measurements of liquids," IEEE Trans. Instrum. Meas., vol. 49, no. 6, pp. 1305–1312, Dec. 2000.

[103] H. Aebischer and C. Matzler, A Microwave Sensor for the Measurement of the Liquid Water Content on the Surface of the Snow Cover. 1983.

[104] D. J. Rowe, A. Porch, D. A. Barrow, and C. J. Allender, "Integrated microwave resonant device for dielectric analysis of microfluidic systems," J. Phys. Conf. Ser., vol. 310, no. 1, p. 012004, 2011.

[105] D. J. Rowe, A. Porch, D. A. Barrow, and C. J. Allender, "Novel Coupling Structure for the Resonant Coaxial Probe," IEEE Trans. Microw. Theory Tech., vol. 60, no. 6, pp. 1699–1708, Jun. 2012.

[106] N. A. Hoog-Antonyuk, W. Olthuis, M. J. J. Mayer, D. Yntema, H. Miedema, and A. van den Berg, "On-line fingerprinting of fluids using coaxial stub resonator technology," Sens. Actuators B Chem., vol. 163, no. 1, pp. 90–96, Mar. 2012.

[107] A. A. Abduljabar, D. J. Rowe, A. Porch, and D. A. Barrow, "Novel Microwave Microfluidic Sensor Using a Microstrip Split-Ring Resonator," IEEE Trans. Microw. Theory Tech., vol. 62, no. 3, pp. 679–688, Mar. 2014.

[108] A. Porch, et al, "Sapphire dielectric resonators for microfluidic compositional analysis," Proc. MicroTAS. 2010.

[109] K. Ohwi, "Liquid dielectric measurement by using YIG resonator," in 1998 International Conference on Microwave and Millimeter Wave Technology Proceedings, 1998. ICMMT '98, 1998, pp. 193–196.

[110] E. Topsakal, T. Karacolak, and E. C. Moreland, "Glucose-dependent dielectric properties of blood plasma," in 2011 XXXth URSI General Assembly and Scientific Symposium, 2011, pp. 1–4.

[111] U. Kaatze and K. Giese, “Dielectric relaxation spectroscopy of liquids: frequency domain and time domain experimental methods,” J. Phys. [E], vol. 13, no. 2, p. 133, 1980.

[112] A. P. Gregory and R. N. Clarke, “Traceable measurements of the static permittivity of dielectric reference liquids over the temperature range 5–50 °C,” Meas. Sci. Technol., vol. 16, no. 7, p. 1506, 2005.

[113] E. H. Grant, 1931-, R. J. Sheppard, and G. P. South, Dielectric behaviour of biological molecules in solution. Clarendon Press, 1978.

[114] F. I. Mopsik, “Precision time-domain dielectric spectrometer,” Rev. Sci. Instrum., vol. 55, no. 1, pp. 79–87, Jan. 1984.

[115] R. H. Cole, J. G. Berberian, S. Mashimo, G. Chryssikos, A. Burns, and E. Tombari, “Time domain reflection methods for dielectric measurements to 10 GHz,” J. Appl. Phys., vol. 66, no. 2, pp. 793–802, Jul. 1989.

[116] G. Voss and H. Happ, “Time domain spectroscopy (TDS) of dielectric properties up to 15 GHz with voltage pulses. Application to solids and liquids,” J. Phys. [E], vol. 17, no. 11, p. 981, 1984.

[117] “Main Page/PHYS 4210/Coaxial Cable - Physics Wiki.” [Online]. Available: http://physwiki.apps01.yorku.ca/index.php?title=Main_Page/PHYS_4210/Coaxial_Cable. [Accessed: 23-Oct-2017].

[118] K. W. Jarrett and L. Goleniewski, “Traditional Transmission Media for Networking and Telecommunications,” 2007.

[119] H. A. Bethe and J. Schwinger, “Perturbation theory for cavities,” Massachusetts Institute of Technology, Radiation Laboratory, 1943.

[120] U. S. Waterproofing, “What is Drain Tile 101 | How Drain Tile Works.” [Online]. Available: http://www.uswaterproofing.com/learning-center/what-is-drain-tile-101-how-drain-tile-works. [Accessed: 23-Oct-2017].

[121] “RG401 Coax Cable with Copper.” [Online]. Available: https://www.pasternack.com/semirigid-0.250-rg401-50-ohm-coax-cable-copper-rg401-u-p.aspx. [Accessed: 23-Oct-2017].

[122] “RG401 Coax Cable with Copper.” [Online]. Available: https://www.pasternack.com/semirigid-0.250-rg401-50-ohm-coax-cable-copper-rg401-u-p.aspx. [Accessed: 23-Oct-2017].

[123] “1052422-1 TE Connectivity AMP Connectors | Connectors, Interconnects | DigiKey.” [Online]. Available: https://www.digikey.com/products/en?mpart=1052422-1&v=17. [Accessed: 22-Oct-2017].

[124] “ANSYS HFSS Open Regions.” [Online]. Available: http://www.ansys.com/-/media/ansys/corporate/resourcelibrary/techbrief/ab-hfss-open-regions.pdf. [Accessed: 23-Oct-2017].

[125] “ANSYS HFSS – Broadband Adaptive Meshing.” [Online]. Available: http://www.ansys.com/-/media/Ansys/corporate/resourcelibrary/application-brief/ab-ansys-hfss-adaptive-broadband-meshing.pdf. [Accessed: 23-Oct-2017].

[126] “Frequency Measurements: How-To Guide - National Instruments.” [Online]. Available: http://www.ni.com/tutorial/7111/en/. [Accessed: 31-Oct-2017].

[127] “6 Frequency Measurement and Manipulation.” [Online]. Available: http://cas.ee.ic.ac.uk/people/dario/files/E302/6frequencyandtime.pdf/. [Accessed: 31-Oct-2017].